Etudes submicroniques de la plasticité du monocristal de Mg.

Gyu Seok Kim

▶ To cite this version:

HAL Id: tel-00721838
https://theses.hal.science/tel-00721838

Submitted on 30 Jul 2012

UNIVERSITÉ DE GRENOBLE

THÈSE

Pour obtenir le grade de

DOCTEUR DE L'UNIVERSITÉ DE GRENOBLE

Spécialité : *2MGE : Matériaux, Mécanique, Génie civil, Electrochimie*

Arrêté ministériel : 15 avril 2011

Présentée par

Gyu Seok KIM

Thèse dirigée par **Marc Fivel** et
codirigée par **Erica Lilleodden** et **Emilie FERRIE**

préparée au sein du **laboratoire Science et Ingénierie des Matériaux et des Procédés (SIMaP)**
dans **le cadre de l'Ecole Doctorale I-MEP2**

Small Volume Investigation of Slip and Twinning in Magnesium Single Crystals

Thèse soutenue publiquement le **15 Avril 2011**,
devant le jury composé de :

M. Edgar RAUCH
DR, CNRS, Président
M. Marc LEGROS
CR, CNRS, Rapporteur
M. Heung Nam HAN
Associated professor, Seoul National University, Rapporteur
M. Daniel Weygand
Dr, KIT, Examinateur
M. Marc Fivel
DR, CNRS, Directeur de thèse
Mme. Erica Lilleodden
Dr, HZG, Co-Directeur de thèse
Mme, Emilie FERRIE
MCF, Grenoble INP, Co-Directeur de thèse

Abstract

A combined experimental and computational investigation of the deformation behavior of pure magnesium single crystal at the micron length scale has been carried out. Employing the recently exploited method of microcompression testing, uniaxial microcompression experiments have been performed on magnesium single crystals with [0001], [2-1-12], [10-11], [11-20] and [10-10] compression axes. The advantage of the microcompression method over conventional mechanical testing techniques is the ability to localize a single crystalline volume which is characterizable after deformation. The stress-strain relations resulting from microcompression experiments are presented and discussed in terms of orientation dependent slip activity, twinning mechanisms and an anisotropic size effect. Such a mechanistic picture of the deformation behavior is revealed through SEM, EBSD and TEM characterization of the deformation structures, and further supported by 3D discrete dislocation dynamics simulations.

The [0001], [2-1-12], and [10-11] compression axes results show dislocation plasticity. Specifically, the deformation due to [0001] compression is governed by pyramidal slip and displays significant hardening and massive unstable shear at stresses above 500MPa. In the case of the two orientations with compression along an axis 45 degrees to the basal plane, unsurpringly it is found that basal slip dominates the deformation. In contrast, compression along the [11-20] and [10-10] directions show deformation twinning in addition to dislocation plasticity. In the case of compression along [11-20], the twinning leads to easy basal slip, while the twin resultant during compression along [10-10] does not lead to easy basal slip. In all cases, a size effect in the stress-strain behavior is observed; the flow stress increases with decreasing column diameter. Furthermore, the extent of the size effect is shown to depend strongly on the number of active slip systems; compression along the [0001] axis is associated with 12 slips systems and displays a saturation of the size effect at a diameter of 10µm, while the other orientations still show a significant size effect at this diameter.

The experimental evidence of an orientation-dependent deformation behavior in flow stress has been investigated by 3D discrete dislocation dynamics simulations. Here, the code TRIDIS was modified for hcp structure and c/a ratio of Mg. By matching the simulation results to experimental results, some proper constitutive material parameters such as initial dislocation density, dislocation source length, the critical resolved shear stress were suggested. For the case of [0001] and [2-1-12] orientation, dislocation feature in the pillar during the deformation was exhibited and strain burst was discussed.

keywords : Magnesium, slip, twin, dislocation, orientation, SEM, EBSD, FIB, TEM, microcompression test, dislocation dynamics, size effect.

Acknowledgements

Foremost, I express my sincere gratitude to my advisors Dr. Marc Fivel, Dr. Erica Lilleodden and Dr. Emile Ferrie for their support of my research. Their scientific guidance and consideration were not limited to my Ph.D work but also touched other aspects of my life.

I also thank Dr. Edgar Rauch, Dr. Marc Legros, Professor Heung Nam Han, and Dr. Daniel Weygand for their fruitful discussions and comments on my thesis.

In addition, I thank Professor Kyu Hwan Oh, who inspired me to pursue scientific research with devotion and passion.

I thank Professor Nobert Huber for giving me the opportunity to work in Helmholtz-Zentrum Geestachat, former GKSS research center.

I especially thank Dr. Sangbong Yi, who provided tremendous support to me during my studies at GKSS. I cannot picture my life in Germany without him.

My sincere thanks also go to Dr. Huang Yuanding, Dr. Florian Pyczak, and Mr. Uwe Lorenz for their assistance with Transmission Electron Microscopy (TEM).

I am grateful to my colleagues and laboratory assistants in France and Germany. It was great to work with you all.

SIMaP : Alex, Jean-Phlip, Charles, Remi, Sebastian, Luis, Hyung-Jun, Pierre, Jennifer, Antoine, Simon, Julien, Juliette, Patrick, Claude Ghiotti, Claire Thomasson, Valerie Quatela, Franck Pelloux and Charles Josserond

HZG : Daniel, Julia, Henry and Paula and Stephanie Koch

I thank my former laboratory members for giving me lots of support from Korea: Dr. Hee-Suk Chung, Dr. Jiwoo Kim, Do-Hyun, Sul-cham, Eun-Kyu, Jong Soo, Jung-Han, Tae-Jun, Eusun, Dr. Chansun Shin, Dr. Tae-Young Kim and Dr. Hyo-Jong Lee.

I am heartily thankful to my parents, parents-in-law, and sister-in-law for their unconditional love and encouragement.

Lastly, I owe my deepest gratitude to Ihn Ok and Rayoon. Ihn Ok, my wife, I could not have accomplished this work without you. Rayoon, my petit angel, I am learning something from you everyday; love, trial, failure, endurance, overcoming and success. I thank you, Lord, for blessing my life with Ihn Ok and Rayoon, and for providing us with the opportunity to be a family.

Table of contents

<div align="right">

CHAPTER 1.

</div>

Introduction

1.1 Motivation for research on magnesium single crystal

Due to the ever increasing need for energy efficiency, the search for lightweight structural materials is an important and active area of research. Magnesium, the lightest of all structural metallic materials, shows great promise, although the inherent plastic anisotropy of this hexagonal close-packed (hcp) metal necessitates a greater basic understanding of its mechanical behavior than is currently known. There is considerable need to develop mechanism-based material models for the deformation of magnesium, due to its strong anisotropy and its importance in the development of lightweight structural materials. Unfortunately, constitutive inputs for such models are critically lacking; fundamental studies of the critical stresses and strains and associated slip and twinning systems are needed.

While many studies have been carried out on Mg single crystal ([Kelly and Hosford 68], [Yoshinaga and Horiuchi 63], [Obara *et al*. 73]), the difficulty of obtaining truly single crystalline bulk materials due to the ease of twinning during sample preparation complicates an unambiguous study of the deformation mechanisms. Identification of individual slip mechanisms have been carried out with *in-situ* TEM investigations ([Couret and Caillard 85] although the stress field is expectedly not uniform, and is made more difficult due to the free surfaces. Therefore, in order to identify slip and twinning activity in magnesium, a simpler, known stress state testing technique is needed, while maintaining a deformation volume small enough for comprehensive post-mortem characterization. Employing the recently exploited method of microcompression testing and 3 dimensional discrete dislocation dynamics (3D DDD), we have investigated the deformation behavior of Mg single crystals.

1.2 Micromechanical characterization.

The recent development of microcompression testing ([Uchic *et al*. 04], [Uchic and Dimiduk 05]) has opened up the possibility of localizing micron-scale volumes of material for uniaxial compression. This method has strong advantages over traditional mechanical testing methods for studying mechanisms of deformation, as the entire deformation volume can be

investigated post-mortem. In this way, the salient features associated with the measured stress-strain characteristics can be identified, circumventing a needle-in-a-haystack approach. The microcompression method has been widely used to investigate the plasticity in fcc single crystals ([Volkert and Lilleodden 06], [Uchic and Dimiduk 05], [Greer *et al*. 06]), showing a significant size effect; yield strength increases significantly with decreasing column diameter. Some studies on bcc materials ([Bei *et al*. 09]) have been carried out, and most recently two studies on Mg (0001) single crystals ([Lilleodden 10], [Byer *et al*. 10]) have been carried out as the first microcompression studies of Mg. These studies showed that pyramidal π2 slip rather than twinning is the relevant mechanism of deformation for [0001] compression in Mg. Lilleodden showed also that the size effect in strength is also present in hcp materials. While such a size effect makes the extraction of material parameters such as critical resolved shear stress difficult, the opportunity to study size effects in Mg, a plastically anisotropic material is advantageous to understanding the widely observed size effect itself. It is therefore of further interest to study other orientations of single crystal Mg, where deformation twinning and the activation of other slip systems is possible.

In this spirit a combined experimental and computational investigation of the deformation behavior of pure Mg single crystal at the micron length scale has been carried out. The stress-strain relations resulting from microcompression experiments will be presented and discussed in terms of orientation dependent slip activity and twinning mechanisms. Such a mechanistic picture of the deformation behavior is revealed through SEM, EBSD and TEM characterization of the deformation structures, and is supported by 3D discrete dislocation dynamics simulations.

1.3. Scope of thesis.

The aim of this research is to investigate the slip and twinning activities of magnesium single crystal at small scale and to study the deformation mechanism of several orientations using a combined experimental and computational approach. The thesis is organized as follows:

- The current understanding of Mg is presented in Chapter 2. The crystallographic information, well established mechanical properties, and a review of the current understanding of the slip and twining behavior is given.

- Part I discusses the experimental micromechanical characterization of magnesium. This part is divided into 3 chapters. Chapter 3 covers the experimental methods employed: sample preparation, focused ion beam (FIB) milling, electron backscattered diffraction (EBSD), transmission electron microscopy (TEM) and nanoindentation. This is followed by two chapters on the experimental results from microcompression experiments on 5 different orientated single crystals. Chapter 4 focuses on the understanding of orientation effects on the slip and twinning mechanisms, while

Chapter 5 focuses on the size effects observed in the stress-strain behavior.

- Part II deals with the 3 dimensional discrete dislocation dynamics (3D DDD) simulations using the program TRIDIS. While TRIDIS cannot take into account the twin activities, it provides strong advantages for studying dislocation activities. For this research, the TRIDIS code has been modified for hcp and employed to match the simulation results to experimentally observed results.

- Part III gives concluding remarks and perspectives for future work

Background on the mechanical behavior of magnesium

2.1 Magnesium: material characters

Investigation of plastic behavior of magnesium has been studied intensively during 1950s and 60s with a few mm size of single crystal. At the early stage of the research, slip and twin activities have been investigated by slip and twin trace analysis from the optical images. As the technical instrument was developed, new effort was invested to identify the deformation mechanism with TEM. The purpose of this chapter is to review the theoretical background of magnesium which has been investigated during last few decades.

Chapter 2 introduces the brief summary of crystallographic information and material properties of magnesium to improve the fundamental understanding. In addition, previous studies regarding the slip and twin systems which play an important role in the deformation behavior are reviewed. In addition, the calculation of Schmid factor which is relatively complicated due to hcp structure is derived. And finally the trend of recent studies on Mg is summarized.

2.1.1 Crystallography of hcp structure

The structure of Mg is hexagonal close-packed (hcp). The primitive hexagonal unit cell has 3 axes ($\mathbf{a_1}=\mathbf{a_2}\neq\mathbf{c}$) with corresponding angles ($\alpha=\beta=90^\circ$, $\gamma=120^\circ$). In one primitive hexagonal unit cell, 2 atoms are placed forming a double lattice structure. Thus, the stacking sequence of hcp structure along $\mathbf{c}$ direction is ABABAB…, in the ideal case (See atom layers of cyan and black in Figure 2.1).

In terms of crystallography, the basic difference between hcp and face center cubic (fcc) is the asymmetry of the array of atom. The unit cell is defined by cubic in case of fcc,

whereas cubic system is not proper to apply to hcp. In order to define the indices of directions and planes in hcp structure, usually Millier-Bravais notation with 4 axes has been used. The 4-axis system is based on the vectors $\mathbf{a_1}$, $\mathbf{a_2}$, $\mathbf{a_3}$ and $\mathbf{c}$ as shown in Figure 2.1; $\mathbf{a_3}$ is redundant since $\mathbf{a_3}$= - ($\mathbf{a_1}$+$\mathbf{a_2}$). With respect to this four vector basis, an arbitrary crystal vector $\mathbf{r}$ may be written by

$$\mathbf{r} = u\,\mathbf{a_1} + v\,\mathbf{a_2} + t\,\mathbf{a_3} + w\,\mathbf{c} \qquad (2.1)$$

with $u + v + t = 0$.
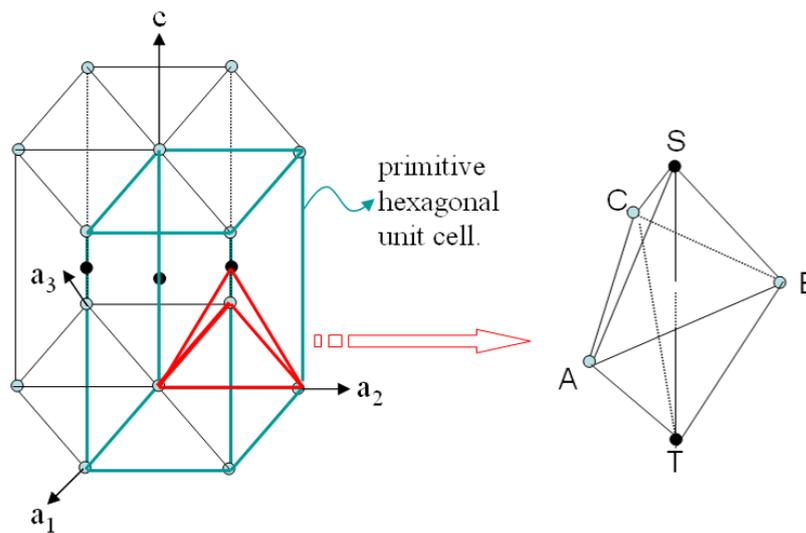
Figure 2.1: Hexagonal close-packed structure. The hexagonal primitive unit cell contains 2 atoms and Thomson-tetrahedron which is used in fcc can be applied to explain the slip system

2.1.2 Material properties

The mechanical properties of Mg are studied during last few decades. Some important mechanical properties are listed in Table 2.1. One of the important material parameters which determine the deformation behavior is c/a ratio. The shortest distance from the atom center to $\mathbf{a}$ and $\mathbf{c}$ axis is usually presented as a and c, respectively. The ideal axial ratio c/a equals $\sqrt{8/3}$=1.633. However, no pure metal has this ideal c/a ratio. Depending on the c/a ratio, some metals such as Zr, Cd show the twinning dominant deformation when compressive load is applied along $\mathbf{c}$ axis, while tensile load is needed for twinning in Mg and Be. Twin activities of hcp material strongly depend on the c/a ratio as will be discussed in Chapter 2.3.

Another interesting material parameter is the elastic modulus. Magnesium is known to have only weak elastic anisotropy whereas the plastic behavior is strongly dependent on the

crystal axis ([Kelly and Groves 70], [Gharghouri *et al.* 99]).

property	value	reference
atomic distance, a	0.321nm	[Yoo 81]
c/a ratio	1.624	[Yoo 81]
density	1.74g/cm³	[handbook]
Elastic modulus	45GPa	[handbook]
poisson's ratio	0.34	[handbook]
Drag coefficient(basal)	0.5×10^{-6} Pa·s	[Groh 09]
stacking fault energy (basal)	36mJ/m²	[Smith 07]
	44mJ/m²	[Chetty et al. 97]
	32mJ/m²	[Uesugi et al. 03]
	<50mJ/m²	[Couret et al 85]

Table 2.1: Some important physical parameters of magnesium

2.2 Slip and twinning in Mg

2.2.1 Slip

Although hcp metals can have many slip systems and twinning systems, Mg is known to be deformed mainly by four slip systems and one twinning system. Figure 2.2 shows the five deformation modes in Mg. Figure 2.2(a), (b), (c) and (d) are basal, prismatic, pyramidal π1 and pyramidal π2 slip systems, whereas (e) is tensile twin system.
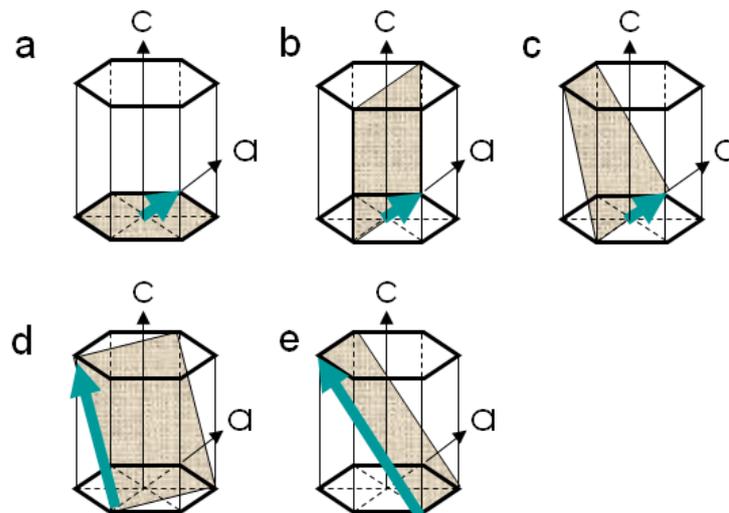
Figure 2.2: Deformation system of magnesium. (a), (b), (c) and (d) are basal, prismatic, pyramidal π1 and pyramidal π2 slip systems, respectively, whereas (e) is tensile twin system.

Type of dislocation	direction	Crystallographic Indices	Relative energy of dislocations	Number of independent Mode
AB	**a**	$\{0001\}[11\bar{2}0]$		2
		$\{10\bar{1}0\}[11\bar{2}0]$	$|a|^2$	2
		$\{10\bar{1}1\}[11\bar{2}0]$		4
ST+AB	**c+a**	$\{0001\}[11\bar{2}0]$	$2.63|a|^2$	
ST	**c**	$\{hki0\}[0001]$	$3.67|a|^2$	5
Twinning		$\{10\bar{1}2\}[10\bar{1}1]$		0.5

Table 2.2: Some important information of four slip systems and twinning system.

Burgers vectors for the structure may also be explained in a similar manner of the Thompson's tetrahedron for face-centered-cubic metals using the bi-pyramidal as shown in Figure 2.1. Some important information of four slip systems is listed in Table 2.2. The basal, prismatic, pyramidal π1 slip systems have <a> Burgers vector, whereas the pyramidal π2 slip system has <c+a> Burgers vector, therefore, the energy of the Burgers vector of pyramidal π2 slip system is greater than that of other slip systems, therefore energetically less stable. In addition, Mg has <c> dislocation, however this is sessile dislocation, thus it cannot contribute to the deformation and is not considered as the important slip system ([Partridge 67]).

According to Taylor criterion, at least five independent slip systems are required to achieve homogeneous, generalized ductility ([Taylor 38]). Robert and Wonsiewicz pointed out that magnesium crystals only possess two independent easy slip systems; both involving the Burgers vector of basal <a> ([Robert CS 64], [Wonsiewicz and Backofen 67]). Non-basal slip mechanism in the prismatic system has been observed by Ward Flynn and Quimby ([Quimby *et al*. 62], [Ward Flynn P *et al*. 61]). Note that basal slip system and prismatic slip system has 2 independent slip modes, respectively. The strain accommodation due to the twin might give another deformation mode. However, because of the polar mechanism of twin as will be discussed in Chapter 2.2.2, twin is thought to give only 0.5 deformation mode. Thus, there are 4.5 independent deformation system; 2 of basal, 2 of prismatic, 0.5 of twinning. Taylor criterion has not been satisfied. Therefore, non-basal slip system has been investigated extensively. As a result, pyramidal slip system with Burgers vector of <a> have been observed ([Reed-Hill and Robertson 57], [Reed-Hill *et al*. 57]).

In contrast, the existence of <c+a> dislocation was on dispute for a long time. Many researchers performed c-axis compression test to investigate slip or twin activities which accommodate the deformation along c-axis by making the Schmid factor of other systems being zero. Though the c-axis compression test, twin has been observed by trace analysis
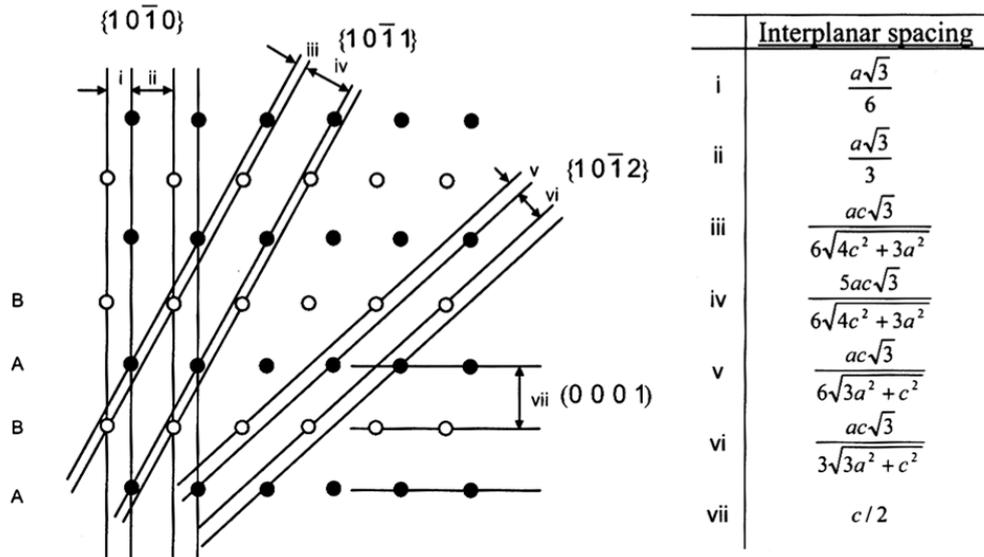
([Bakarian and Mathewson 43], [Yoshinaga and Horiuchi 63]). However, employing TEM analysis, <c+a> dislocation, so called pyramidal π2 slip system, has been observed ([Obara *et al*. 73], [Stohr and Poirier 72]). Such a <c+a> slip system introduces 5 independent equivalent slip systems, thus, Taylor law could be satisfied successfully.

Figure 2.3 shows temperature dependence of critical resolved shear stress (CRSS) of basal slip system and prismatic slip system in Mg. Because the basal slip system has the lowest CRSS, basal slip system is more easily activated than prismatic slip system or other slip system.
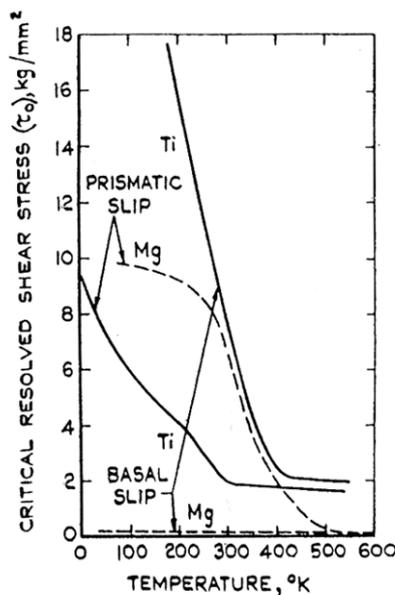
Figure 2.3: Temperature dependence of critical resolved shear stress of basal slip system and prismatic slip system in Mg. ([Partridge 67])

Figure 2.4 shows the projection of atoms in (1-210) plane which shows the interplanar spacing and traces and corrugation of atom array. Closed circles are the atoms in A layer and open circles are the atoms in B layer. The interplanar spacing of non-basal plane is different depending on the selection of atom layer. One interesting thing is the interplanar spacing between the slip planes. The interspacing of basal plane is simply calculated as c/2. In contrast prismatic planes or pyramidal planes are not uniformly spaced (See (i) and (ii) in Figure 2.4). Slip usually occurs most widely spaced planes because a wide, planer core tends to produce low value of energy barrier. If the c/a ratio is smaller than $\sqrt{3}$, the interplanar spacing of prismatic plane is greater than that of basal plane. Because c/a ration of Mg is 1.624, prismatic slip system should be easier to be activated than basal slip with the point of view of interplanar spacing. However, prismatic slip system is more difficult to be activated indeed, and this is because of the stacking fault.

{10$\bar{1}$0} {10$\bar{1}$1} {10$\bar{1}$2} (0 0 0 1)

	Interplanar spacing
i	$\dfrac{a\sqrt{3}}{6}$
ii	$\dfrac{a\sqrt{3}}{3}$
iii	$\dfrac{ac\sqrt{3}}{6\sqrt{4c^2+3a^2}}$
iv	$\dfrac{5ac\sqrt{3}}{6\sqrt{4c^2+3a^2}}$
v	$\dfrac{ac\sqrt{3}}{6\sqrt{3a^2+c^2}}$
vi	$\dfrac{ac\sqrt{3}}{3\sqrt{3a^2+c^2}}$
vii	$c/2$

Figure 2.4: Projection of atoms in (1-210) plane which shows the interplanar spacing and traces. Closed circles are the atoms in A layer and open circles are the atoms in B layer. ([Partridge 67])

The basal <a> dislocation and non-basal <a> can be dissociated following equation 2.2 and equation 2.3, respectively. However, only the stacking fault in basal plane is energetically favored due to the corrugated atom array of non-basal planes ([Rosenbaum 64]). The equation 2.2 indicates the dissociation of <a> dislocation into Shockley partial dislocation.

$$\frac{1}{3}[11\bar{2}0] \rightarrow \frac{1}{3}[10\bar{1}0] + \frac{1}{3}[01\bar{1}0] \qquad (2.2)$$

$$\frac{1}{3}[11\bar{2}0] \rightarrow \frac{1}{6}[11\bar{2}1] + \frac{1}{6}[11\bar{2}1] \qquad (2.3)$$

In case of <c+a> dislocation, because of the high energy, dissociation is more strongly occurred to reduce the energy. Rosenbaum suggested a dissociation mechanism of <c+a> dislocation as equation 2.4. Although such dissociation was reasonable in terms of energy reduction, it was not observed by experimentally ([Rosenbaum 64]). The use of TEM enables more clear dislocation observation. Morozumi *et al.* suggested the dissociation of <c+a> dislocation based on their TEM observation as equation 2.5 ([Morozumi *et al.* 76])

$$\frac{1}{3}[11\bar{2}3] \rightarrow \frac{1}{6}[11\bar{2}3] + \frac{1}{6}[11\bar{2}3] \qquad (2.4)$$

$$\frac{1}{3}[11\bar{2}3] \rightarrow [0001] + \frac{1}{3}[10\bar{1}0] + \frac{1}{3}[01\bar{1}0] \qquad (2.5)$$

Individual dislocation behavior has been also studied ([Couret and Caillard 85], [Couret 85]). They performed *in-situ* TEM as shown in Figure 2.5 and suggested kink-pair mechanism based on their observation of prismatic dislocation. At the heart of the explanation, the dislocations are assumed to glide by jumps between adjacent valleys, via the thermally activated nucleation of a pair of kinks with opposite signs, as shown in Figure 2.6.
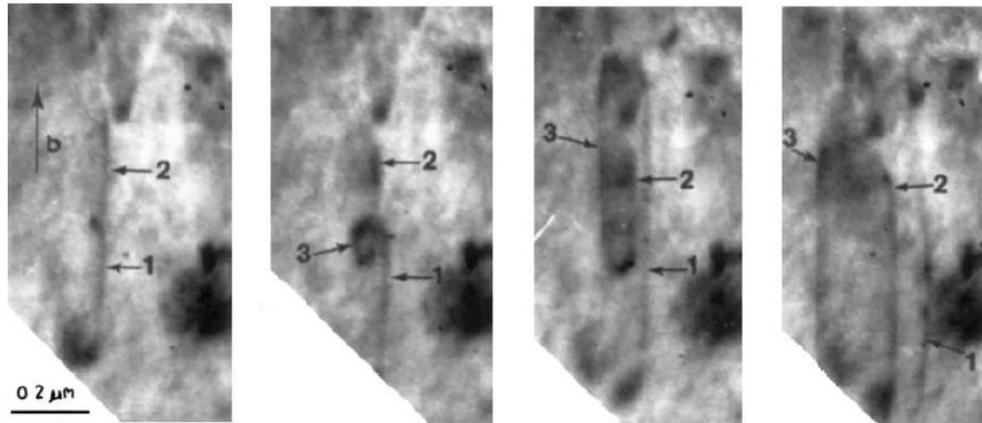
Figure 2.5: Prismatic slip in magnesium at 300 K The movement of screw dislocations is controlled by the kink-pair mechanism. A dislocation loop formed at a pinning point expands by the rapid movement of its edge parts ([Couret *et al.* 85]).
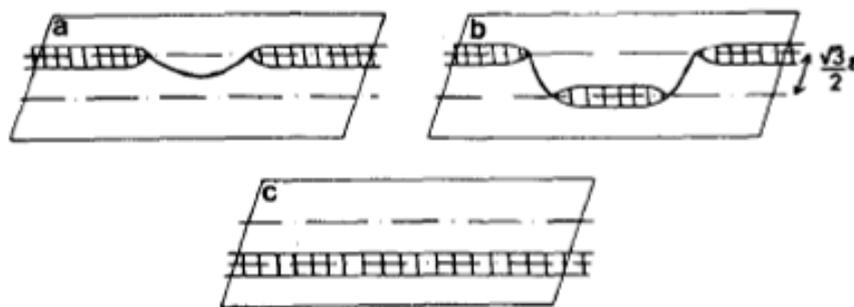
Figure 2.6: Kink-pair mechanism. ([Couret *et al.* 85]).

2.2.2 Twinning

Twinning proceeds by the atoms translation for the accommodation of deformation, thus, it is a polar mechanism which cannot be reversible, while slip is reversible process. Due to such a one-directional character, twin is thought to have a contribution only 0.5 independent deformation mode as discussed in chapter 2.2.1. Nevertheless, the understanding of twin is of importance because twinning is a major deformation mode with basal slip at room temperature.

In contrast to the dislocation slip which critical resolved shear stress is required for

activation, the twin requires the nucleation stress for activation. The twin nucleation stress is much higher than the twin propagation stress. Therefore, twin can easily occurs at the stress concentrated zone such as grain boundary.

Twin leads to the reorientation of the crystal. In case of tensile twin of Mg, the misorientation of mother and daughter is about 87.3 degrees. However, that does not mean that there was huge translation in atom array. Only a small atomic translation can change the crystallographic orientation. Actually, although the contribution of twin itself to plastic strain is not so tremendous in case of polycrystalline, twin can play an important role because the twin modifies the crystallographic orientation of mother to the dislocation slip favored orientation. In case of monocrystalline magnesium, due to the absence of grain boundary, almost all volume is twinned, once twin occurred. Therefore, the influence of twin is much larger in single crystal.

The incidence of twinning is affected by the purity of the metal. And the twinning behavior can be changed depending on the sample size. For example, Bian and Shin observed secondary twin (twinning in the twinned region) after the uniaxial compression test of Mg single crystal at the bulk scale, whereas Kim *et al*. did not observe any secondary twin from the uniaxial compression test at the micro scale ([Bian and Shin 09], [Kim *et al*. 10]). This may be due to the difference of the incidence of twinning. At the bulk scale, twins can occur at several points and they meet each other after their propagation. This lead to the heterogeneous stress field in the sample, as a result secondary twin can be generated. In contrast, at the small scale, once the twinning happens, twin propagates and almost all region of the sample is twinned. Therefore, there is no chance for twins to interact each other.

Several twin modes have been studied in hcp metal. Although {10-11}[10-12] twin, so-called compression twin, can be occurred in some cases, e.g, high strain rate ([Barnett MR 07]), {10-12}[10-11] twin, so-called tensile twin, is observed widely. Tensile twin is named because {10-12}[10-11] twin occurs when tensile stress is applied along c-axis.

The deformation mechanism due to twinning can be explained employing Figure 2.7 and Table 2.3. As shown in Figure 2.7, once twin occurs on twin habit plane K_1), atoms translate along η_1 direction with the rotation axis of **R**.
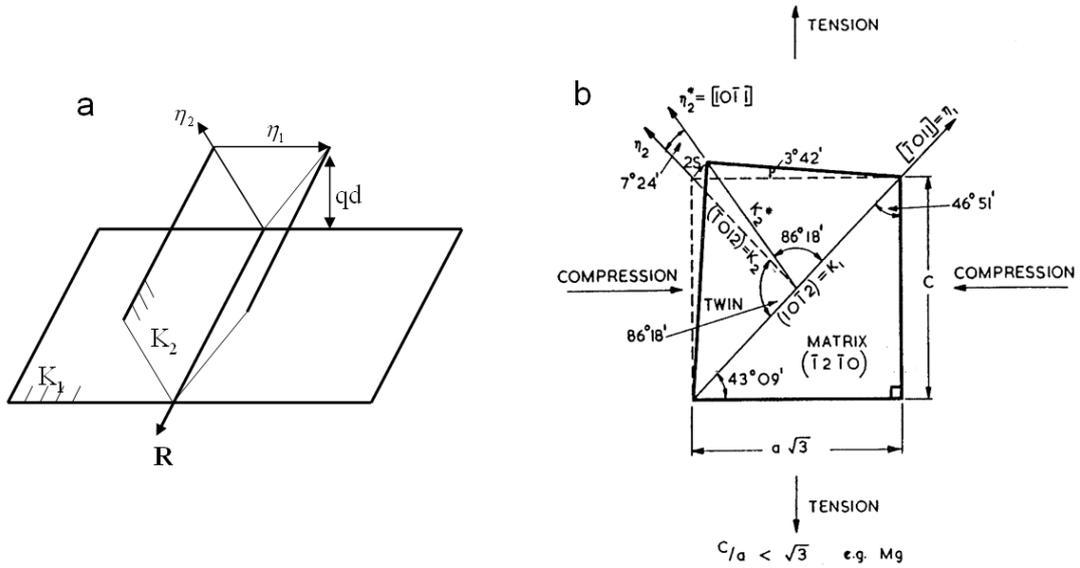
Figure 2.7: Schematic image of twin mechanism. Tensile twin occurs when the tensile loading is applied along c-axis.

One interesting thing is the complexity of atomic shuffling ([Yi 05]). Because of the double lattice system of hcp structure, the translation of four atomic layers is needed to complete the tensile twinning process in case of Mg. The atoms in second or third layers can only have the small amount of translation, so-called shuffling. The parameter q in Table 2.3 indicates the required atomic spacing for twinning. A schematic image of atom translation in tensile twinning is shown in Figure 4.23.

K_1	K_1	η_1	η_2	R	q	twinning shear(2S)
$\{10\bar{1}2\}$	$\{10\bar{1}\bar{2}\}$	$\pm<\bar{10}11>$	$\pm<10\bar{1}\bar{1}>$	$\pm1/3\{1\bar{2}10\}$	4	$\dfrac{2\left|\gamma^2-3\right|}{\gamma^2+3}$

Table 2.3: Some important parameters of tensile twinning in Mg. The parameters corresponds to Figure 2.7(a).

Such a translation of atoms leads to the resultant plastic shear, 2S. The twining shear is defined by the ratio of original atomic distance and the moved distance of atom due to twin. Each twin system has different twinning shear and that is affected by c/a ratio, γ. The equation for calculation of twinning shear is shown in Table 2.3. And the relation of c/a ratio, twinning shear and twinning system is shown in Figure 2.8. In case of tensile twinning of Mg, the twinning shear is 0.129.
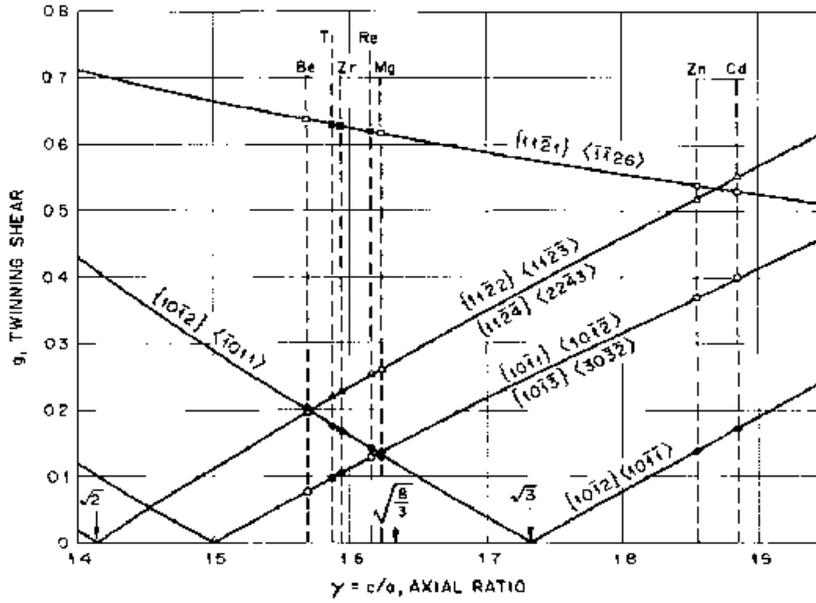
Figure 2.8: The amount of twinning shear with c/a ratio. ([Yoo 81])

2.2.3 Calculation of Schmid factor

Despite the necessity to consider Schmid factor for the investigation of slip/twin activity, the calculation of Schmid factor is not well known in case of hcp material. The asymmetry of c/a ratio and the use of 4 Miller-Bravais indices of hcp material make the calculation difficult in comparison to fcc material. In this section, we summarize how to calculate the Schmid factor in case of hcp material. In addition, some useful general equations for hcp material are given. For details of the calculation, see [Thomas and Goringe 79].

As we discussed in equation 2.1, one can introduce a line direction **r** as [*uvtw*]. In addition, one can introduce a plane **p** as (hikl). If **r** is the normal vector of the plane **p**, they have the relationship given in equation 2.6

$$\left[uvtw\right]=\left[hkil\right]^{*}=\left[hkil\,\lambda^{-2}\right] \quad (2.6)$$

where, $\lambda^{2}=\dfrac{2}{3}\left(c/a\right)^{2}$, $*$ is the reciprocal lattice.

Conversely, the plane $\left(hkil\right)$ normal to the direction $\left[uvtw\right]$ is given by equation 2.7.

$$\left(hkil\right)=\left(uvtw\right)^{*}=\left(uvt\,\lambda^{2}\,w\right). \quad (2.7)$$

To obtain the Schmid factor, it is necessary to calculate the inner product of loading axis and slip direction as well as the loading axis and slip plane. The angle between two

22

vectors, $\mathbf{r_1} = \begin{bmatrix} u_1\, v_1\, t_1\, w_1 \end{bmatrix}$ and $\mathbf{r_2} = \begin{bmatrix} u_2\, v_2\, t_2\, w_2 \end{bmatrix}$, is given by

$$\cos\left(r_1 \bullet r_2\right) = \frac{r_1}{|r_1|} \bullet \frac{r_2}{|r_2|} = \frac{u_1 u_2 + v_1 v_2 + t_1 t_2 + \lambda^2 w_1 w_2}{\left(u_1^2 + v_1^2 + t_1^2 + \lambda^2 w_1^2\right)^{1/2}\left(u_2^2 + v_2^2 + t_2^2 + \lambda^2 w_2^2\right)^{1/2}}. \quad (2.8)$$

where $\mathbf{r_1} \bullet \mathbf{r_2} = \dfrac{3a^2}{2}\left(u_1 u_2 + v_1 v_2 + t_1 t_2 + \lambda^2 w_1 w_2\right).$

By combining equation 2.6 and equation 2.8, we can also derive the angle between the line direction $\mathbf{r_1} = \begin{bmatrix} u_1\, v_1\, t_1\, w_1 \end{bmatrix}$ and plane $\mathbf{p_1} = \begin{bmatrix} h_1\, k_1\, i_1\, l_1 \end{bmatrix}$ as given equation 2.9,

$$\cos\left(r_1 \bullet p_1\right) = \frac{r_1}{|r_1|} \bullet \frac{p_1}{|p_1|} = \frac{u_1 h_1 + v_1 k_1 + t_1 i_1 + w_1 l_1}{\left(u_1^2 + v_1^2 + t_1^2 + \lambda^2 w_1^2\right)^{1/2}\left(h_1^2 + k_1^2 + i_1^2 + \lambda^{-2} l_1^2\right)^{1/2}}. \quad (2.9)$$

Similarly, the angle between two planes, $\mathbf{p_1} = \begin{bmatrix} h_1\, k_1\, i_1\, l_1 \end{bmatrix}$ and $\mathbf{r_2} = \begin{bmatrix} h_2\, k_2\, i_2\, l_2 \end{bmatrix}$, takes as follows,

$$\cos\left(p_1 \bullet p_2\right) = \frac{p_1}{|p_1|} \bullet \frac{p_2}{|p_2|} = \frac{h_1 h_2 + k_1 k_2 + i_1 i_2 + \lambda^{-2} l_1 l_2}{\left(h_1^2 + k_1^2 + i_1^2 + \lambda^{-2} l_1^2\right)^{1/2}\left(h_2^2 + k_2^2 + i_2^2 + \lambda^{-2} l_2^2\right)^{1/2}} \quad (2.10)$$

where, $\mathbf{g_1} \bullet \mathbf{g_2} = \dfrac{2}{3a^2}\left(h_1 h_2 + k_1 k_2 + i_1 i_2 + \lambda^{-2} l_1 l_2\right).$

As a result, Schmid factor can be derived by multiplying of equation 2.8 and 2.9. When the load is applied with the direction of direction $\mathbf{r_1} = \begin{bmatrix} u_1\, v_1\, t_1\, w_1 \end{bmatrix}$, the slip plane of $\mathbf{p_1} = \begin{bmatrix} h_1\, k_1\, i_1\, l_1 \end{bmatrix}$, slip direction of $\mathbf{r_2} = \begin{bmatrix} u_2\, v_2\, t_2\, w_2 \end{bmatrix}$, Schmid factor is given by equation 2.7.

$$\cos\left(r_1 \bullet r_2\right) \times \cos\left(r_1 \bullet p_1\right) = \left(\frac{r_1}{|r_1|} \bullet \frac{r_2}{|r_2|}\right) \times \left(\frac{r_1}{|r_1|} \bullet \frac{p_1}{|p_1|}\right)$$

$$= \frac{u_1 u_2 + v_1 v_2 + t_1 t_2 + \lambda^2 w_1 w_2}{\left(u_1^2 + v_1^2 + t_1^2 + \lambda^2 w_1^2\right)^{1/2}\left(u_2^2 + v_2^2 + t_2^2 + \lambda^2 w_2^2\right)^{1/2}} \times \frac{u_1 h_1 + v_1 k_1 + t_1 i_1 + w_1 l_1}{\left(u_1^2 + v_1^2 + t_1^2 + \lambda^2 w_1^2\right)^{1/2}\left(h_1^2 + k_1^2 + i_1^2 + \lambda^{-2} l_1^2\right)^{1/2}}$$

$$(2.10)$$

Table 2.4 gives Schmid factor of some representative loading axis. As will be discussed in Chapter 3 and 4, [0001], [2-1-12], [10-11], [11-20], [10-10] directions are the initial orientation used in this work and [2-1-1-3], [10-130] are the directions of the twinned specimen. Each of them has an initial orientation of [11-20] and [10-10], respectively.

| Slip System	$[0\,0\,0\,1]$	$[2\,\bar{1}\,\bar{1}\,2]$	$[1\,0\,\bar{1}\,1]$	$[1\,1\,\bar{2}\,0]$	$[2\,\bar{1}\,\bar{1}\,3]$	$[1\,0\,\bar{1}\,0]$	$[1\,0\,\bar{1}\,30]$
Basal	0	**0.50**	**0.43**	0	**0.44**	0	0.03
Prismatic	0	0.20	0.23	**0.43**	0.12	**0.43**	0
Pyramidal (π1)	0	0.29	0.41	0.38	0.21	0.38	0.01
Pyramidal (π2)	**0.45**	0.30	0.22	0.44	0.40	0.33	**0.46**
Pyramidal (π3) *tensile twin*	0	0.27	0.18	**0.37**	0.36	**0.50**	0.50

Table 2.4: Schmid factor of each slip and twin system with some important loading axis. These Schmid factor will be used in this research, repeatedly.

2.3 Recent researches on Mg

Due to the increase of industrial needs of Mg alloys, the mechanical behavior of Mg alloys is extensively studied. Investigations focus on the increase of elongation to improve formability or development of strengthened Mg alloy. The high elongation can be obtained by suppression of basal orientation which is mainly observed after rolling. For example, Mg shows a brittle character with a basal plane oriented texture. If the texture is randomly distributed after rolling, more grains can accommodate the deformation. On the other hand, the strengthening can be achieved by proper fabrication processing such as ECAP which produce grain refinement.

Yi *et al*. controlled the microstructure and deep-drawing was successfully performed ([Yi *et al*.10]). Agnew *et al*. used rare element such as yittrium when they elaborate the Mg alloy ([Agnew *et al*. 01]). The rare materials disperse the normal direction of texture after rolling which lead to higher elongation. On the other hand, Kim *et al*. performed ECAP and obtained high strength Mg alloy ([Kim and Sa 06]).

In contrast, many efforts to understand the basic mechanics of Mg are also invested. For example, Wu *et al*. and Manna *et al*. applied cyclic loading to Mg alloys to investigate the twinning effect which shows a one directional and not reversible deformation ([Wu *et al*. 08], [Manna *et al*. 07]). And they obtained the experimental strain hysteresis displayed in Figure 2.9.
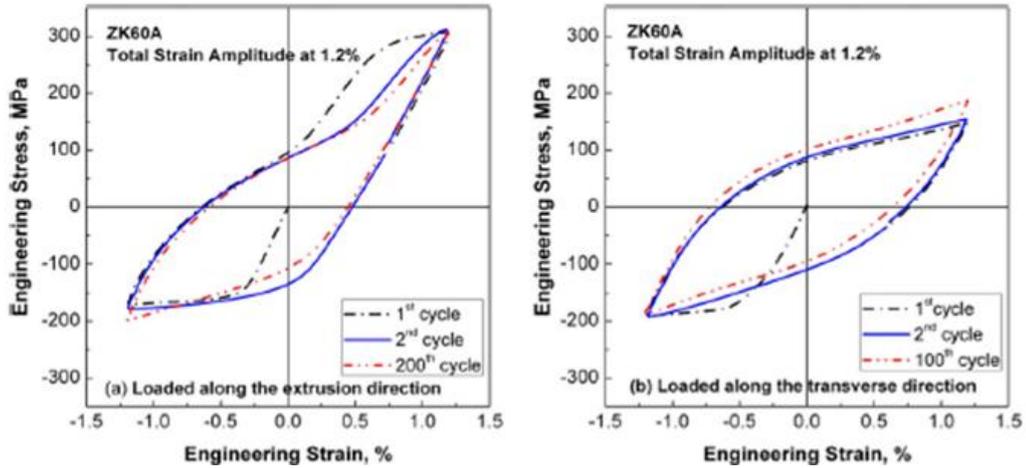
Figure 2.9: Strain hysteresis due to twinning during cyclic loading is shown with two loading direction ([Wu *et al*. 08]).

On the other hand, simulation approaches have also been used. For example, Agnew *et al*. and Yi used VPSC modeling to study the effect of the different slip and twinning systems on the deformation in the polycrystalline Mg alloy ([Agnew *et al*. 05], [Yi 05]).

More fundamental studies have been performed by many researchers. For example, Bian *et al*. performed uniaxial compression test with pure Mg single crystal at bulk scale (~ a few mm) and observed the secondary twinning as shown in Figure 2.10 ([Bian and Shin 09]).
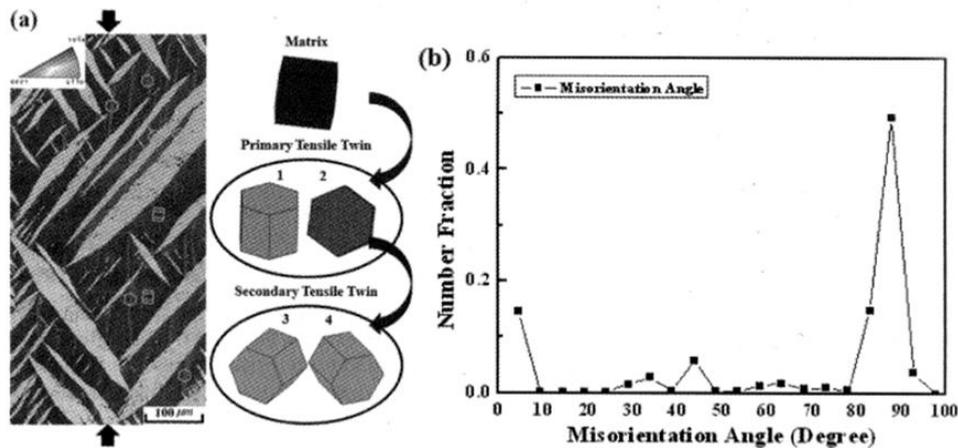

Figure 2.10: Observation of secondary twinning after the uniaxial compression test with pure Mg single crystal at bulk scale ([Bian and Shin 09]).

Graff *et al*. tried to obtain constitutive law by matching ABAQUS simulation results with experimental results performed by Kelly and Hosford. ([Graff *et al*. 07], [Kelly and Hosford 68]). Figure 2.11(a) shows the experimental result of channel die test of Mg single crystal and Figure 2.11(b) shows the matched simulation result. Lilleodden and Byer *et al*. performed microcompression test on (0001) oriented Mg single crystal, however, even such experiment

is meaningful, the study of twinning is excluded ([Lilleodden 10], [Byer *et al*.10]).

Such a lack of fundamental understanding of the deformation behavior of Mg single crystal obviously requires more investigation on both experimental and simulation aspect. From the coming Chapter, we will discuss the observed orientation effect, size effect and deformation mechanism obtained by experiment and simulation.
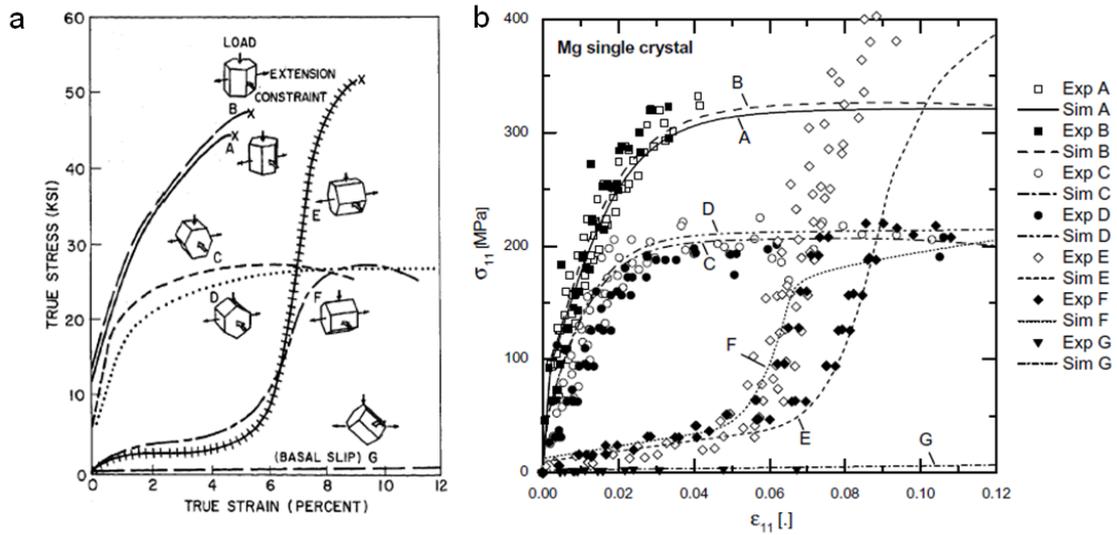
Figure 2.11 (a) experimental result of channel die test of Mg single crystal ([Kelly and Hosford 68]) (b) matched simulation result ([Graff *et al*. 07])

Key points of Chapter 2

1. Mg has four slip systems (basal, prismatic, pyramidal $\pi1$ and pyramidal $\pi2$) and one twin system.

2. The Burgers vector of basal, prismatic, pyramidal $\pi1$ slip systems is <a> dislocation whereas the Burgers vector of pyramidal $\pi1$ slip system is <c+a> dislocation.

3. Twin occurs by atom translation and it is an irreversible process whereas slip is a reversible process depending on the loading direction.

4. Schmid factor can be estimated from following equation.

$$\cos\left(r_1 \bullet r_2\right) \times \cos\left(r_1 \bullet p_1\right) = \left(\frac{r_1}{|r_1|} \bullet \frac{r_2}{|r_2|}\right) \times \left(\frac{r_1}{|r_1|} \bullet \frac{p_1}{|p_1|}\right)$$

$$= \frac{u_1 u_2 + v_1 v_2 + t_1 t_2 + \lambda^2 w_1 w_2}{\left(u_1^2 + v_1^2 + t_1^2 + \lambda^2 w_1^2\right)^{1/2} \left(u_2^2 + v_2^2 + t_2^2 + \lambda^2 w_2^2\right)^{1/2}} \times \frac{u_1 h_1 + v_1 k_1 + t_1 i_1 + w_1 l_1}{\left(u_1^2 + v_1^2 + t_1^2 + \lambda^2 w_1^2\right)^{1/2} \left(h_1^2 + k_1^2 + i_1^2 + \lambda^{-2} l_1^2\right)^{1/2}}$$

5. More fundamental studied are needed to improve the understanding of plastic deformation of Mg.

Part I.

Experimental Micromechanical Investigations

<div align="right">CHAPTER 3.</div>

Experimental Methods

An experimental investigation of the slip and twin activities of magnesium single crystal is presented in Part I. Here, in Chapter 3, the experimental methods employed are described in detail. Specifically, the bulk single crystals sample preparation procedures, the FIB fabrication methods for preparing microcolumns and thin sections for post-deformation characterization, the characterization techniques used to investigate the deformation structures (i.e., SEM, EBSD and TEM), and importantly the microcompression method used to perform the mechanical tests are presented.

3.1 Sample preparation

A [0001] oriented single crystal has been purchased from Goodfellow, GmbH, with a purity of 99.999%. To obtain samples with [11-20], [10-10], [10-11] and [2-1-12] oriented surfaces from the [0001] disk, the sample was polished and the in-plane orientations identified with electron backscatter diffraction (EBSD). The samples were then cut using spark erosion, and subsequently polished, with a final mechanical step of 50nm SiO_2 slurry in a diluted solution of Pril[®] detergent and de-ionized water. A final etching step was used in order to remove some of the damage layer and to reveal the presence of any twins.

Figure 3.1 shows the procedure of the sample preparation for different orientations. After the identification of the orientation of the disk, specimens ①,② and ③ are used for [0001], [1-100], [11-20] oriented sample, respectively, as shown in Figure 3.1(a). In the case of preparing the [10-11] and [2-1-12] orientation samples, a sample holder was fabricated with pure magnesium polycrystal to obtain the 45 degree tilted orientation from the basal plane. As shown in Figure 3.1(b) and (c), the specimen ④ and ⑤ were mounted in a special sample holder for careful polishing. The polished samples of 2 different types of 45degree tilted are shown in Figure 3.1(d). The use of a pure magnesium polycrystal is helpful to calibrate the background during EBSD observations on the single crystalline pillars.
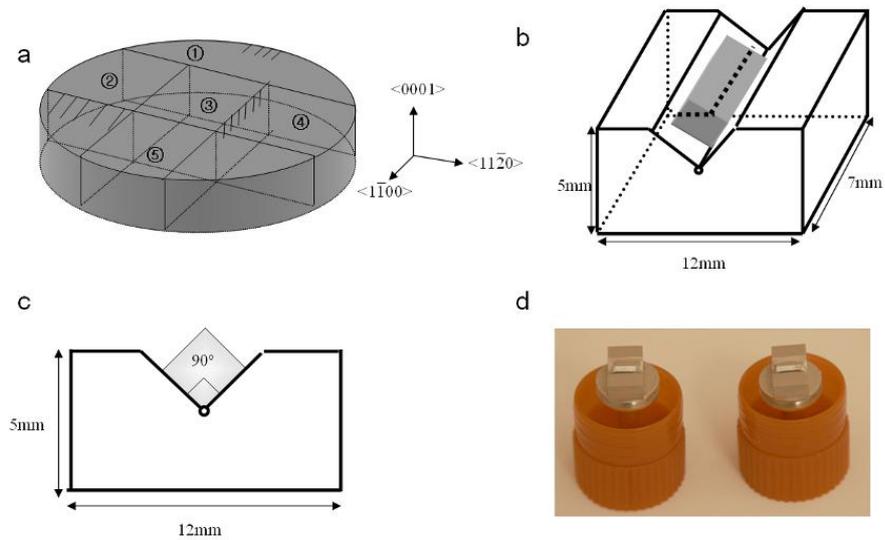
Figure 3,1: (a) Schematic image of the orientation and cutting direction of [0001] disk. (b) The specimen ④ and ⑤ were mounted to sample holder. (c) Front-view image of mounted sample and its holder. (d) Polished sample surface of the specimen ④ and ⑤.

The surface of the sample was imaged after spark erosion, prior to polishing, as shown in Figure 3.2(a). The sample surface is irregular and lots of twins are observed. After polishing, the surface was very smooth with a mirror reflection.
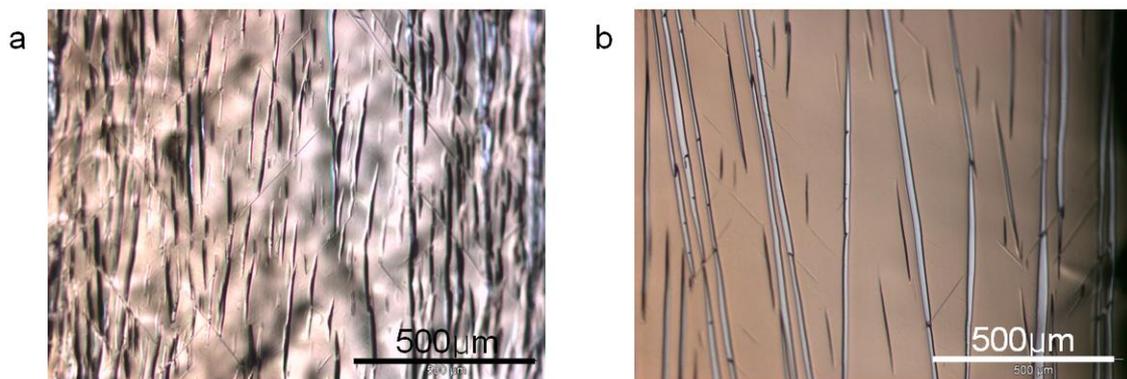

Figure 3.2: Optical micrographs of sample surface (a) after spark erosion and (b) after mechanical and electro polishing. The narrow needle-like structures are twins.

However, despite careful polishing with a fine particle size and minimal pressure, deformation twins were unavoidable. The post-polishing surface sample is shown in Figure 3.1(b), underscoring the possible influence of pre-existing twins in bulk deformation studies.

Prior to fabrication of the microcolumns, EBSD was used to determine whether any pre-existing twins were present in the regions of interest, and to confirm the initial orientation

of the sample surface. The misorientation of the sample surface from the ideal axis was less than 2 degrees. A few twins of thickness on the order of 1~2µm were observed, as shown in Figure 3.3, consistent with the optical micrograph given in 3.2(b). The use of small volume studies along with EBSD for identifying twin-free regions is a strong advantage of the microcompression technique.
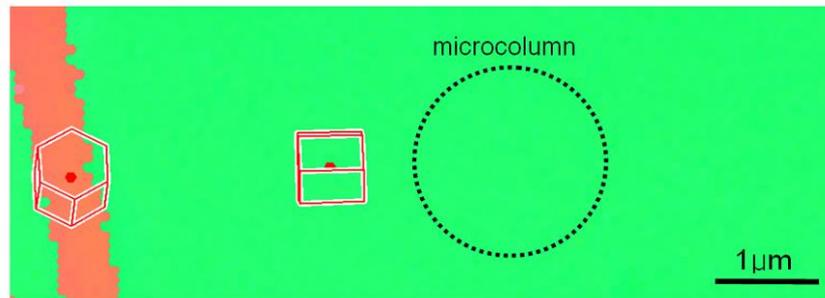
Figure 3.3: EBSD micrograph of the [11-20] sample surface. The [11-20] out of plane orientation is designated in green. Due to spark erosion, deformation twins (shown in orange) were not avoidable. Microcolumns were fabricated in twin-free regions.

3.2 SEM/Focused Ion Beam (FIB)

3.2.1 Principles of SEM/FIB

Focused ion beam (FIB) systems have been produced commercially for approximately twenty years, primarily for the semiconductor industry. FIB systems operate in a similar fashion to a scanning electron microscope (SEM) except that FIB systems use a highly focused beam of ions (usually gallium) rather than electrons. These focused ions can be operated at low beam currents for imaging or high beam currents for site specific sputtering or milling. More recently, FIB systems can be coupled with a SEM system for dual imaging and fabrication capabilities.

The gallium (Ga+) primary ion beam hits the sample surface and sputters a small amount of material, which leaves the surface as either secondary ions or neutral atoms. The primary beam also produces secondary electrons. As the primary beam rasters on the sample surface, the signal from the sputtered ions or secondary electrons can be collected to form an image. Imaging is not necessary however, and typically is not carried out for FIB milling applications, where the focused beam rasters across the sample according to a selected pattern in order to removed material within the pattern. The focused ion beam may alternatively be controlled in a circular path in order to produce ring patterns, so-called annular milling.

3.2.2 Microcolumn fabrication

Microcompression columns were created from the individual bulk single crystals using focused ion beam machining on a Nanolab 200 Dualbeam Scanning Electron and Focused Ion Beam (FIB) microscope from FEI. Typical microcolumns fabricated by FIB are shown in Figure 3.4, with varying diameters from 1 to 10µm. Varying the column diameter was of interest to investigate size effects. Annular cutting was employed with varying probe currents and cutting parameters that depend on the final desired geometry. Attempt was made to ensure a 3:1 aspect ratio of height to mid-plane diameter, and to minimize column taper. In any case where the ratio was greater than 4:1 or less than 2:1, the column was not used in the analysis of stress-strain response. Due to the annular cutting method used, a slightly larger base diameter than top diameter will result, with a typical taper angle of 1.5 degrees for the 5 and 10 µm diameter columns, and approximately 2 degrees for the 1 and 2 µm diameter columns. An elliptical foot leads to a greater taper angle for the lower ¼ of the column. Although this leads to some variation in axial stress along the column, the taper helps to stabilize the column if there is any misalignment between the microcolumn and the flat punch.

The SEM micrographs in Figure 3.5 (a) and (b) show a typical 5 µm diameter column prior to deformation and its cross section after 0.7% compression, respectively. The cross section was prepared with a FIB. The light gray corresponds to a protective Pt layer deposited prior to sectioning, the mid-gray corresponds to redeposited Mg during column preparation, and the dark gray corresponds to the Mg single crystal. Accurate measurement of the height from SEM images prior to deformation is difficult due to surrounding material, and the unavoidable tilted 3D perspective. Errors in geometry measurements can lead to inaccuracies in the analysis of stress and strain. Such cross sectional geometry analyses provide a useful approach to accurate height identification.
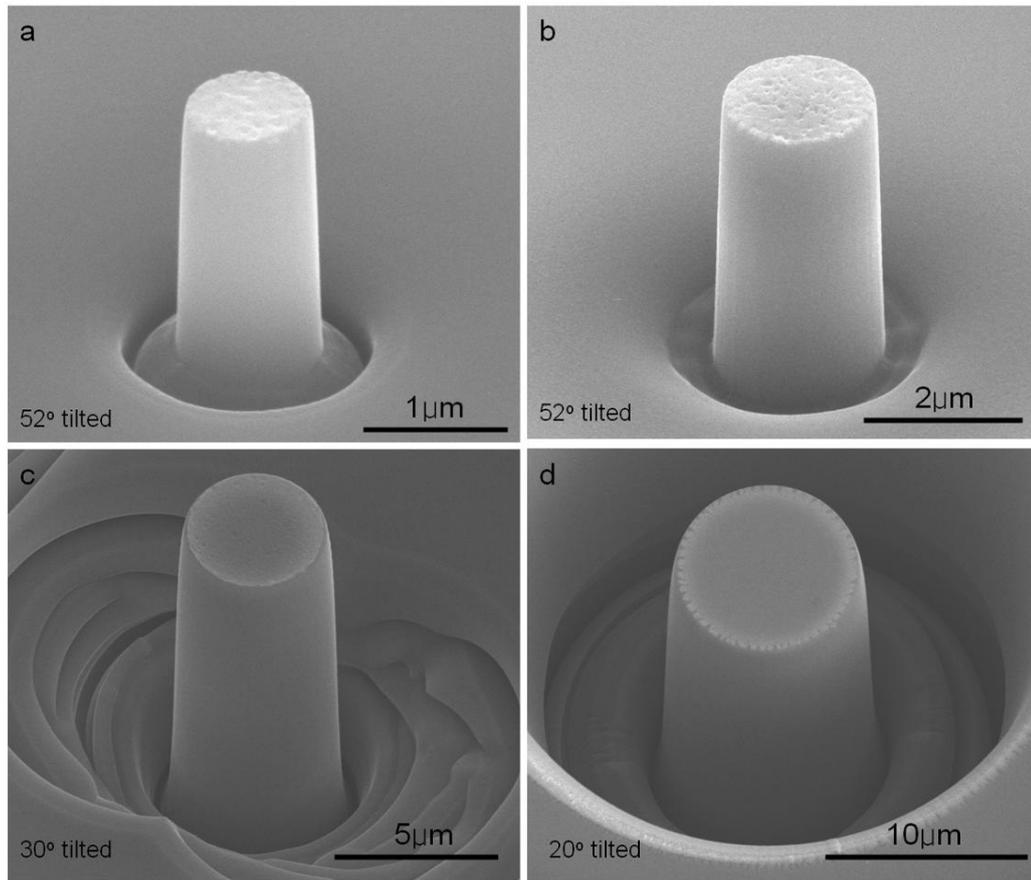
Figure 3.4: Typical microcolumns fabricated by FIB are shown with a nominal diameter of (a) 1µm (b) 2µm (c) 5µm (d) 10µm.
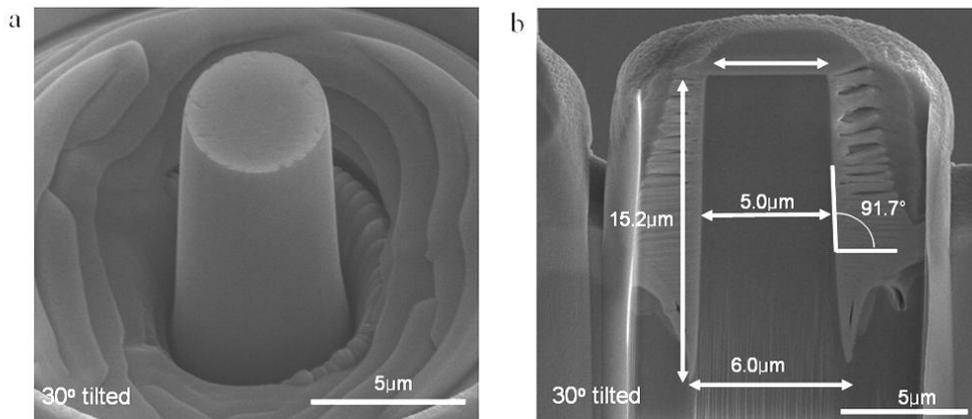
Figure 3.5: SEM micrographs of (a) a pre-deformed column and (b) the cross section of a column deformed to 0.7% strain.

3.2.3 TEM sample fabrication.

After compression testing, deformed columns were observed carefully by SEM to investigate the deformation shape, slip lines, and other potential features. Thin lamella were fabricated from several microcolumns using the FIB milling in order to investigate dislocation

and twin activities by TEM, and to measure the misorientations associated with the deformation by EBSD.

Figure 3.6 shows the procedure of TEM foil by cross-sectional cutting, a recently wide spread technique for TEM sample preparation. The TEM sample preparation is as follows:

(a) At first, platinum was deposited on the column to make a protection layer. Pt deposition covers whole column.

(b) The cross-sectioning has been performed on either side of the to-be prepared foil.

(c) Through-section cutting to free the lamella from the bulk, leaving one connecting section

(d) Lifting out of the lamella using an Omniprobe micromanipulator is performed.

(e) Mounting the lamella on copper grid. Pt deposition is used to glue the lamella to copper grid.

(f) Thinning has been performed until the thickness of the foil reaches below 300nm with 'cleaning cross section' option. The thickness of 300nm is enough to perform TEM observation in case of Mg. Final cleaning has been performed with low voltage (5keV) FIB milling at a glancing angle was conducted to minimize the Ga-induced damage layer. In this step, 'rectangle' sectioning option is used. Prior to TEM analysis, Ar plasma cleaning was performed for up to 5minutes directly before loading the sample into the TEM.
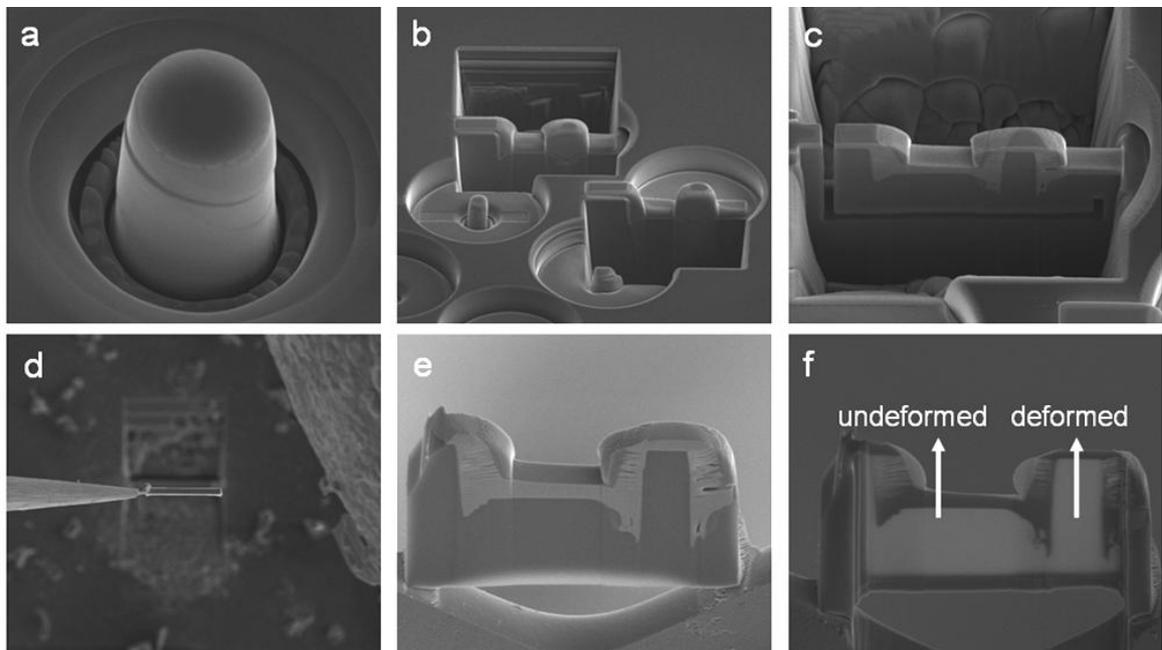
Figure 3.6: Typical working procedure of TEM sample by cross-sectioning. Figure shows (a) the initial deformed column, (b) regular and cleaning cross sections conducted on two columns, (c) through-cutting to partially free the lamella from the bulk material, (d) lift out of the lamella using an Omniprobe micromanipulator, (e) mounting of the lamella on a copper TEM grid, and (f) thinning to electron transparent thickness.

In this research, it is of interest to investigate the slip and twin activities of the columns, and therefore requires the fabrication of TEM specimens taking directly along the slip planes observed from the deformation structure (e.g., as shown in Fig 3.7(a)). A novel method has been demonstrated by Norfleet *et al*. ([Norfleet *et al*. 08]). They directly observed the slip activities of slip planes in Ni single crystal by fabricating the TEM foils parallel to the slip plane. Using this method, TEM samples were fabricated, as shown in Figure 3.7.
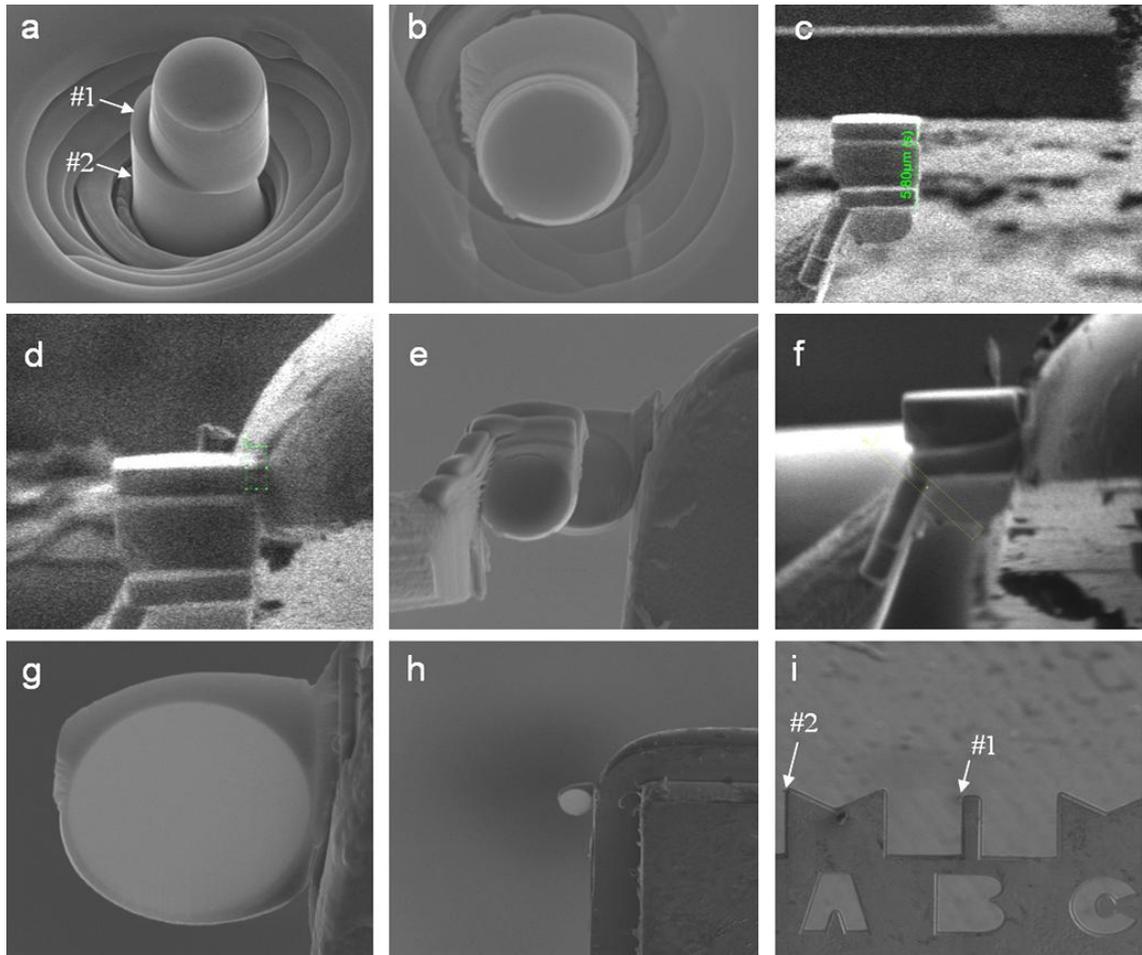
Figure 3.7: A novel method for TEM sample preparation of slip plane sections from compressed microcolumns. A section of the column where massive slip occurred is indicated by (#1) and a section parallel to #1 away from the massive slip is designated as (#2) and have been chosen for TEM foil preparation. Figure shows (a) initial (b) Pt deposition on slip plane (c) lift out, (d) mounting of bottom part #2 of column on copper grid, (e) cutting out of the middle part of column, (f) mounting of #1 on copper grid, (g) after thinning of #2, (h) after thinning of #1, and (i) an overview of copper grid with both TEM foils #1 and #2.

3.3 Electron Backscattered Diffraction (EBSD)

Electron backscattered diffraction (EBSD) is a useful technique for investigating crystal orientation with high spatial resolution. This is particularly important for the work carried out herein, where twinning within micron-scale volumes is to be investigated.

The EBSD is usually installed inside SEM chamber. To perform the EBSD testing, the polished sample should be mounted with tilting angle of 70degree. The electrons emitted collide with the material, as a result, the backscattered electrons exit the material. The electrons which satisfy the Bragg's condition can be detected by phosphor. The diffracted electrons from many different planes form Kikuchi pattern. Each pattern corresponds to one of the lattice plane. From the Kikuchi pattern, the Miller indices can be indexed based on crystal data. Figure 3.8 shows the typical Kikuchi pattern obtained in EBSD system.
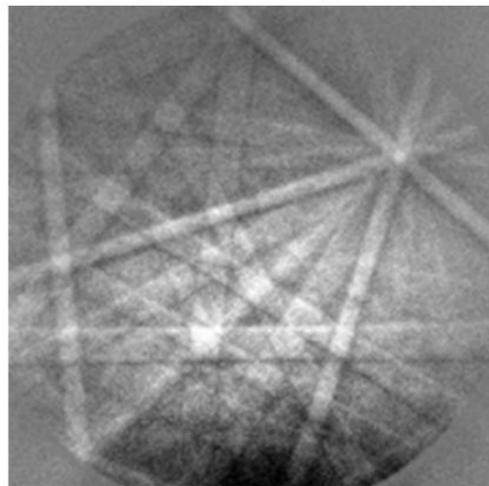
Figure 3.8: A typical kikuchi pattern obtained by EBSD. Each band corresponds to reflection atom plane.

The EBSD system inside FIB is shown in Figure 3.9(a). In order to examine the crystallographic orientation with EBSD, the sample should be tilted 70degrees. Due to the confined internal volume of FIB chamber and high risk of damage during high angle tilting, 45degrees pre-tilted sample tray was prepared, therefore, only 25degrees of sample holder was tilted.

A pure magnesium polycrystalline dummy sample was prepared to calibrate the background of camera. The same sample holder was used to prepare the degree tilted sample as shown in Figure 3.1. Note that this research has been carried out with single crystal, thus, polycrystalline magnesium is needed. The copper grid that contains EBSD or TEM sample was attached on the edge of the surface of dummy sample. Figure 3.9(b) shows the EBSD sample on the copper grid. The bright ring in the middle of the image is the EBSD sample.
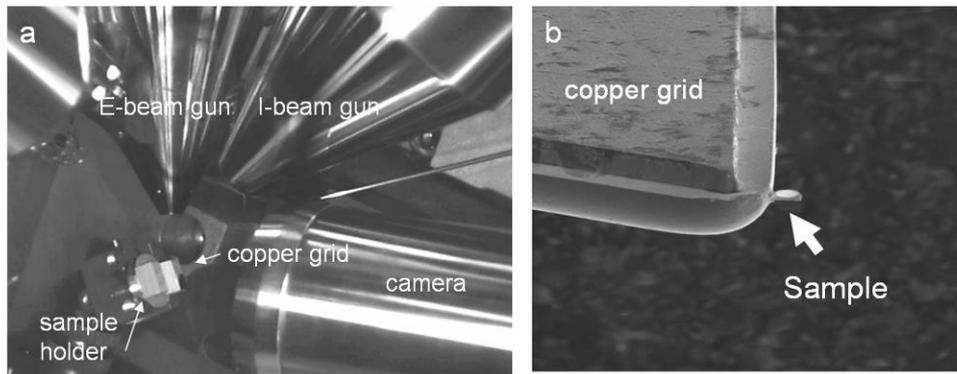
Figure 3.9: EBSD measurement inside the FIB Nanolab 200. A CCD camera image inside the microscope chamber is shown in (a) and an example of a sample used for EBSD measurement is shown in (b). The bright ring in the middle is the sample.

3.4 Transmission electron microscopy(TEM)

In order to investigate the dislocation mechanisms involved in the deformation of Mg, TEM provides the best resolution. Although one must be careful of various artifacts (e.g., from sample preparation), direct observation of the dislocation structures can be achieved, and the Burgers vectors identified. The TEM work in this research was carried out within the Department of Metal Physics at GKSS on a Philips CM200 microscope with an accelerating voltage of 200kV, and a double tilt holder.

While the principles of transmission electron microscopy can be found elsewhere ([Williams and Carter 04], [Thomas and Goringe 79]), a practical aspect to be presented here is the diffraction patterns for the hcp lattice. These diffraction patterns allow the achievement of appropriate imaging conditions and accurate analyses of results. The principle diffraction patterns for the hcp structure are given in Fig 3.10.

The imaging of dislocation was obtained with two beam condition. From the diffraction pattern, we reflected two beams. Figure 3.11(a) shows the typical two beam condition used in this research. Such dislocations are visible or invisible depending on the reflected beam as shown in Figure 3.11(b). The dislocations are analyzed using the dislocation extinguish condition.
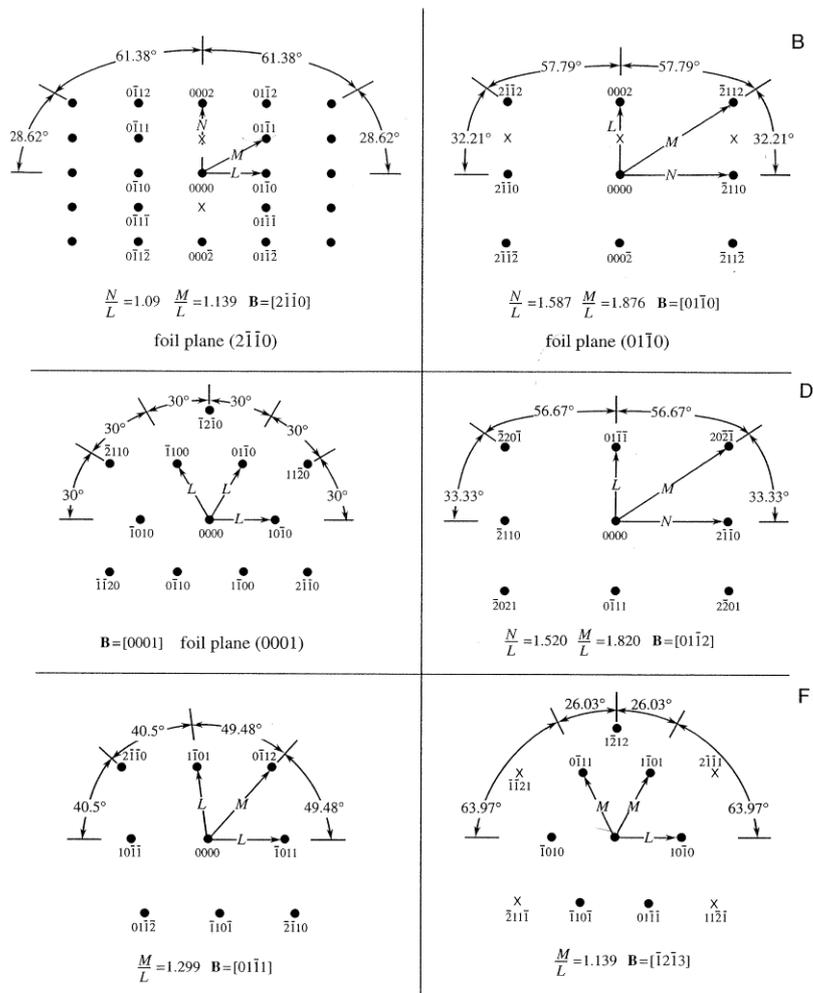
**Figure 3.10**: The principle diffraction patterns needed for investigating Mg, a hcp structure ([Williams and Carter 04]).
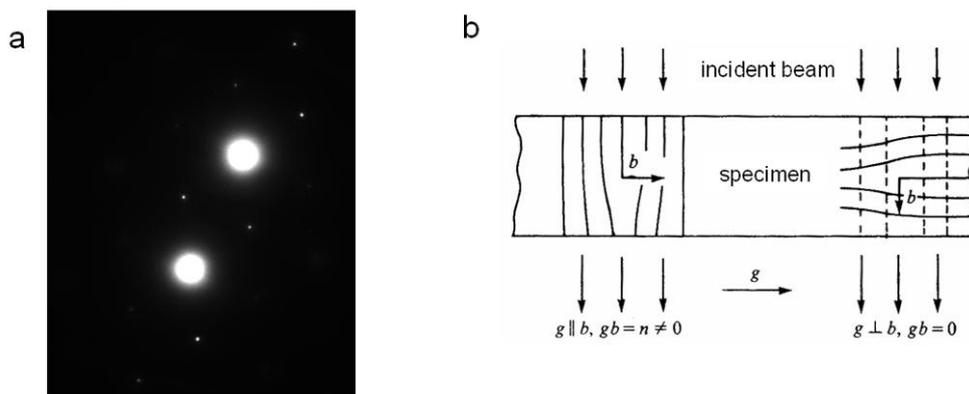
Figure 3.11: (a) Typical two beam condition used in dislocation imaging. (b) The dislocation can be visible or invisible depending on the reflected beam. The dislocations are analyzed by comparing the images of different reflection conditions.

3.5 Nanoindentation-based testing

3.5.1 Principles of Nanoindentation
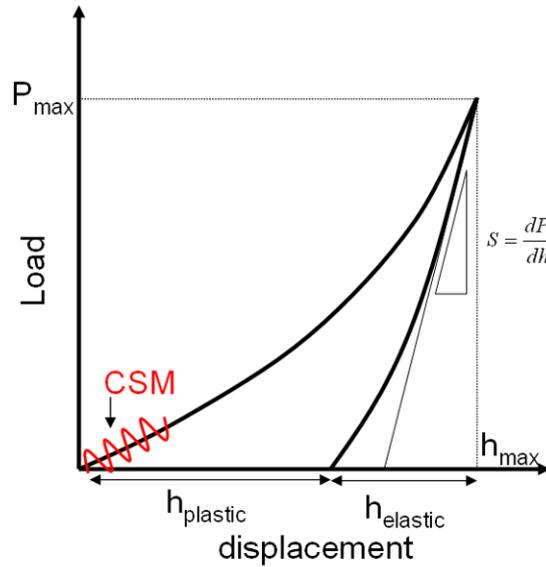
Figure 3.12: Schematic of the load-displacement trace achieved during nanoindentation testing.

Nanoindentation is a mechanical testing method which provides high resolution load and displacement measurements while pressing an indenter tip (typically a sharp pyramidal diamond) into the surface of a sample. From the resultant load-displacement traces, as shown in Fig 3.12, mechanical properties such as elastic modulus and hardness can be assessed ([Oliver and Pharr 92]). The load-displacement curve shows both elastic and plastic deformation. The elastic displacement during the loading is recovered when the unloading is finished. From the unloading process, the elastic stiffness can be directly calculated by $S = dP/dh$, where P is load and h is displacement. One important thing is the determination of the area function. The details are presented in the Oliver's study ([Oliver and Pharr 04]). By determination of an area function, A, the hardness, H, can be derived by equation (3.1). And the elastic modulus, E, can be calculated by equation (3.2)

$$H = \frac{P_{max}}{A} \qquad (3.1)$$

$$\frac{4}{\pi} \frac{P_{max}}{S^2} = \frac{H}{E^2} \qquad (3.2)$$

Recently, the continuous stiffness method (CSM) was developed ([Oliver and Pharr 04]), offering a measurement of the contact stiffness during the entire loading history. In this method, indenter tip indents the material with a small displacement oscillation imposed on the quasi-static loading. The amplitude and frequency can be chosen by the operator, though typically a small displacement amplitude of 2nm is chosen to maintain the assumption of elastic contact during the oscillation cycle.

3.5.2 Microcompression testing

While traditional sharp-tip nanoindentation provides highly localized measurements of the modulus and hardness, the very complex stress and strain state makes it not ideal for studying fundamental mechanisms of deformation and the associated critical stresses. However, through the employment of flat tip indenters and novel sample geometries, micro-scale compression testing can be achieved. This microcompression testing technique was first developed by Dimiduk and Uchic ([Uchic *et al*. 04]) and has been applied to various material systems, although the primary focus has been fcc metals.

The principle of this technique is largely the same as for sharp tip indentation, but the analysis of data differs. For the microcompression testing conducted in this work, the protocol proposed by Lilleodden has been followed, where the governing equations are given in Fig 3.13.

Load:	$P_{sample} = P_{raw} - k_s h_{raw}$
Displacement:	$h_{sample} = h_{raw} - h_{surface} - h_{LF} - h_{substrate}$ where: $\quad h_{LF} = \dfrac{P_{sample}}{S_{LF}}$ & $\quad h_{substrate} = \dfrac{1-\upsilon^2}{E}\dfrac{P_{sample}}{D_{foot}}$
Stress:	$\sigma_{eng} = \dfrac{P_{sample}}{\frac{\pi}{4}D^2_{o,mid}}$
Strain:	$\varepsilon_{eng} = \dfrac{h_{sample}}{H_o}$
P_{raw}: raw load; k_s: instr. spring const.; h_{raw}: raw disp.; h_{surf}: surface position; h_{LFS}: load-frame disp.; h_{sub}: substrate disp.; S_{LFS}: load-frame stiffness; υ: Poisson's ratio; E: Young's modulus; D_{foot}: diam. of column foot; $A_{mid,o}$: initial x-section area at mid-height; H_o: initial sample height	

Fig. 3.13: Governing equations for the analysis of engineering stress-strain response from measured load-displacement data from microcompression tests.

In order to assess the validity of the stress-strain analysis, the elastic modulus can be used. Despite the contention that the elastic modulus of Mg is largely isotropic, the orientation dependent uniaxial moduli can be calculated from the known elastic constants for each of the investigated compression directions. In turn, the elastic modulus can be analyzed from the experimental data and compared to the theoretical value. In order to assess the elastic modulus from microcompression tests, two approaches are used; measuring of elastic modulus from unloading data, and the elastic modulus from the continuous stiffness method.

The compression experiments were conducted with a Nanoindenter XP (Agilent) outfitted with a flat ended conical indenter with a (nominally) 15 micron diameter (nominally) circular punch. This diameter was chosen to ensure that it is larger than the largest column

diameter and smaller than the perimeter of surrounding material from which the column was milled. The sample is ensured to be parallel to the punch by inspection of flat punch indentations prior to the microcompression experiments. The flat punch indentations on the sample of the [0001] and [2-1-1 2] samples are shown in Figure 3.14. The symmetry of the [0001] orientation and asymmetry of the [2-1-1 2] orientation are clearly shown. But more importantly, it is shown that the perimeter of contact is symmetric, indicating good alignment of the surface normal and loading axis. This ensures that the microcolumns will be loaded uniaxially.
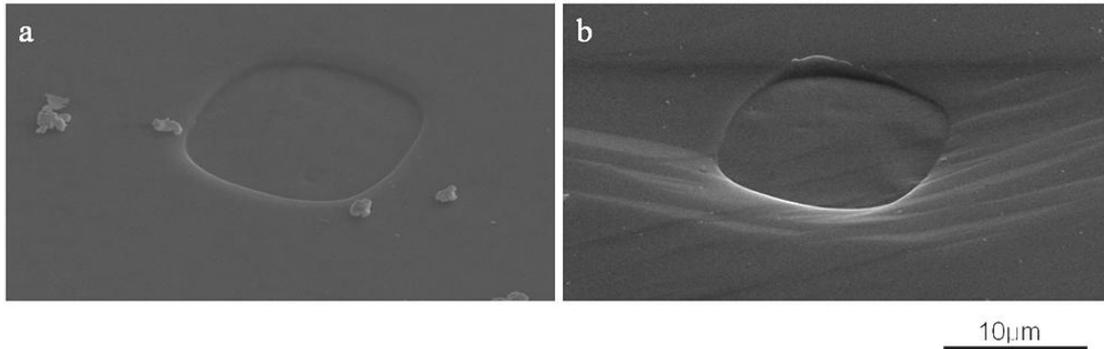
Figure 3.14: The imprint of a flat punch indent on (a) the [0001] surface and (b) the [2-1-12] surface. Microcompression test has been performed with a 15μm diameter circular punch. We also can see the plastic anisotropy of magnesium single crystal from the punch imprint.

The microcompression experiments were run to varying maximum strain using a nominally constant strain rate of 0.001/s. The instrument is an inherently load controlled instrument, and thus the displacement rate was controlled via feedback from the loading signal in order to achieve a specified strain rate. No additional attempt to control the displacement rate was made, and therefore physical instabilities related to material behavior during compression can lead to large displacement bursts. The size of the burst is a coupled effect of material and instrument behavior.

In order to assess the reproducibility of the experiments, at least 5 columns of the 5 micron diameter columns from each of the [0001], [11-20], [10-10], [2-1-12] and [10-11] orientations were carried out. Additionally, 1, 2, 10μm diameter columns have been tested to investigate the size effect.

3.6. Outstanding experimental issues

The microscale experiments carried out within this work are associated with certain outstanding issues which need to be kept in mind during subsequent analyses. The potential problems are discussed here to help provide a realistic background for better understanding this research.

3.6.1 Misalignment during the compression test.

Misalignment between the flat punch and the microcolumn can lead to non-uniaxiality of the stress state. Such misalignment may be due to misalignment of the sample in the sample tray for the Nanoindenter, or when the sample surface is not plan parallel when mounted in FIB prior to column fabrication. Some amount of misalignment is unavoidable. However; the unavoidable taper of our columns due to annular milling actually helps mitigate problems of misalignment.

3.6.2 Ga-damage layer on the surface of column.

It is known that FIB milling creates an amorphized Ga-damage layer ([Ko *et al*. 07]), which depends on the atomic weight of material, voltage, and exposed time. It is not clear how much the thickness of Ga-induced damage layer is in the case of Mg. In the case of Si, it has been observed that the damaged layer is 13nm after 5kV milling ([Ko *et al*. 07]). Mg might have a thicker damage layer due to its low atomic weight. In this research, the Ga-damage layer is formed during annular cutting for column fabrication as well as cleaning cross sectioning for TEM sample preparation. The damage layer on the TEM foils has been minimized by low-voltage milling and Ar plasma cleaning after milling. However, Ga-damage layer from the annular cutting was unavoidable. Attempts to minimize the formation of damage layer were made by minimizing or avoiding FIB-based imaging of the columns during or after fabrication.

> ## Key points of Chapter 3
>
> .
>
> 1. Microcompression pillars have been prepared from varying orientation and with varying diameter using FIB annular milling.
>
>   - Orientation: [0001], [2-1-12], [10-11]. [11-20] and [10-10]
>
>   - Diameter: 1μm, 2μm, 5μm, 10μm.
>
> 2. Micro compression tests have been performed using a nanoindenter outfitted with a flat punch indenter. The stress-strain analysis of measured load-displacement is presented
>
> 4. TEM foils are prepared by FIB.
>
> 5. EBSD and TEM were employed to investigate the twin/slip activity.

<div style="text-align: right;">

CHAPTER 4.

</div>

Experimental results: orientation effects

In this chapter, the deformation behavior of Mg single crystals of 5 different orientations ([0001], [2-1-12], [10-11], [11-20] and [10-10]) with a fixed nominal column diameter of 5 µm is presented. In the following chapter the effect of varying the column diameter will be discussed. Here, the focus is on the orientation-dependent mechanisms of deformation, as revealed through scanning electron microscope (SEM), electron backscattered diffraction (EBSD) and transmission electron microscopy (TEM) characterization of the deformation structures.

4.1 [0001] compression tests

The stress-strain response of 6 cylindrical microcolumns with nominal diameter of 5µm is shown in Figure 4.1. The stress increases linearly up to 2% of strain at the stress level of nearly 250 MPa followed by hardening and then a massive strain burst at a stress level of around 570 MPa. The compliance observed at the early stage of the deformation is widely observed in compression testing at both the micro-scale and the macro-scale, and is likely due to the seating between the loading platen (i.e., flat punch indenter) and the top of the microcolumn. The behavior is shown to be highly reproducible. SEM images of initial and deformed columns are shown in Figure 4.2. It is shown that a slight buckling shape develops during compression, leading to the unstable shearing out of a chunk of material at a critical stress of 570 MPa,
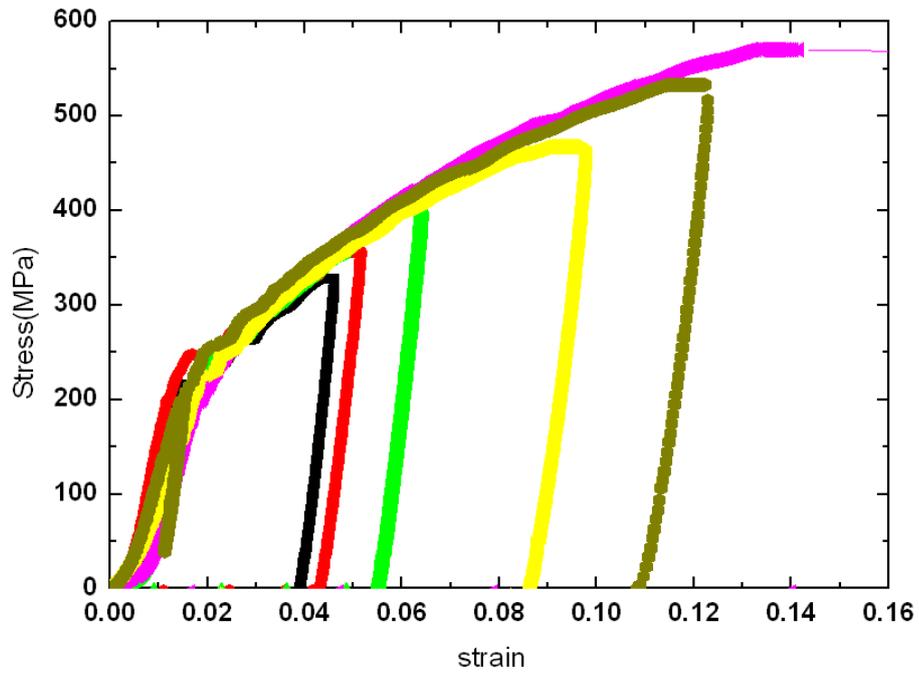
Figure 4.1: Stress-strain behavior of 6 microcolumns with nominal mid-height diameter of 5µm.
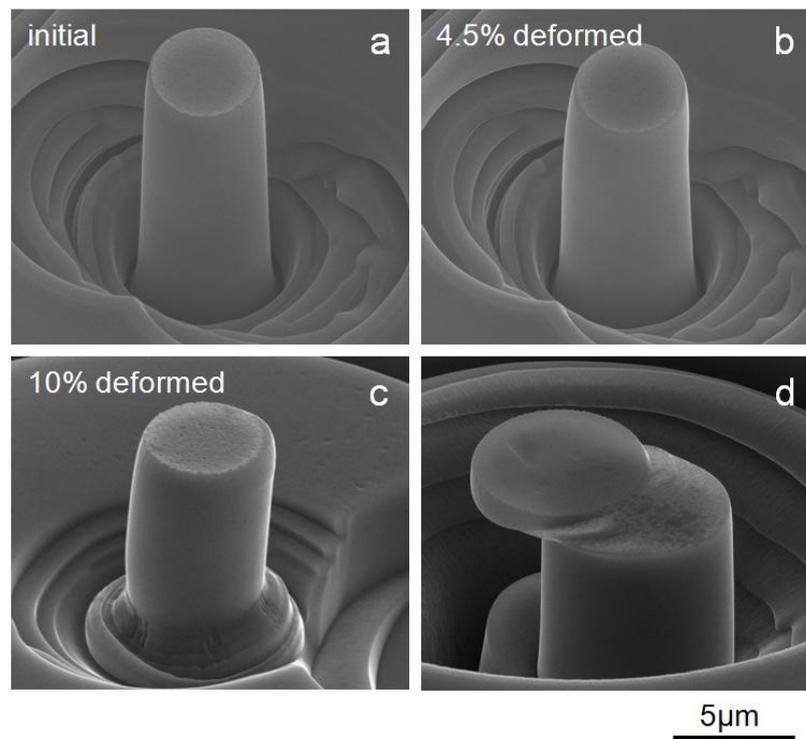
**Figure 4.2**: SEM images of [0001] oriented columns (a) before compression and (b)-(d) after compression to varying strains, as noted.
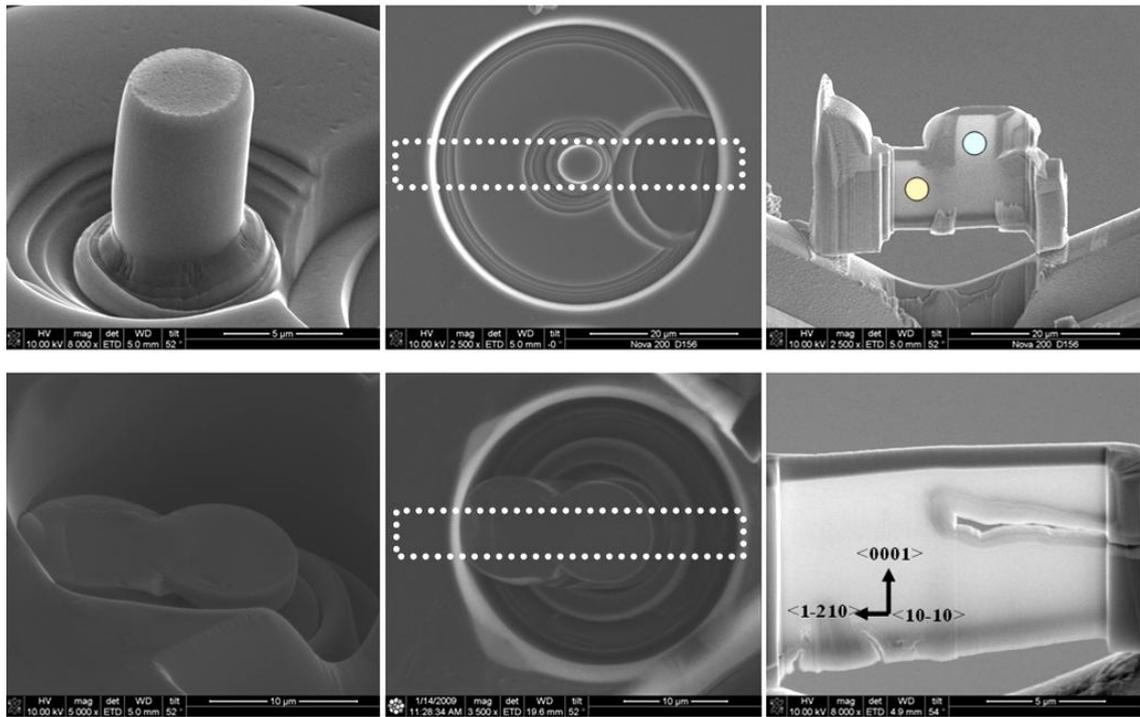
Figure 4.3: FIB-based foil preparation from two columns for TEM and EBSD analyses.

Table 2.4 gives the Schmid factors for the various slip and twinning systems in Mg. It is shown that the Schmid factor for the basal, prismatic, and pyramidal $\pi 1$ systems is zero when the stress is applied along $<c>$ axis. Furthermore, it has been shown that the $\pi 3$ twinning system is not easily activated during $<c>$ axis compression [Partridge 67]. It is therefore expected that the deformation is accommodated by the 6 equivalent pyramidal $\pi 2$ slip systems in case of [0001] orientation. With consideration of cross-slip of $<c+a>$ dislocation onto {2-1-12} and {10-11} planes, there are 12 slip systems that can accommodate the deformation. This would lead to very strong hardening due to the intersection of these slip planes. Furthermore, the slips systems are symmetrically distributed relative to the c-axis. Therefore, if the sample is well aligned the buckling direction and massive shear directions (for highly stressed columns) should show no single preferred direction amongst the compressed columns. This is in fact what was observed, and serves to verify that misalignment issues were negligible as shown in Figure 5.3
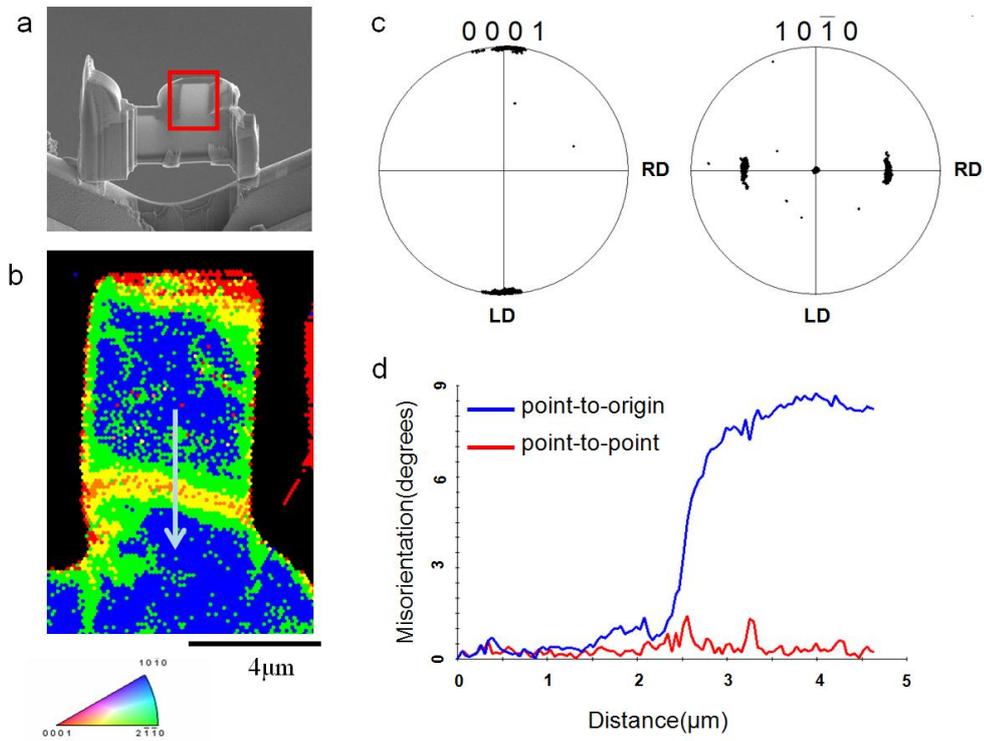
Figure 4.4: EBSD observations of a 10% deformed column. (a) The thinned section of the microcolumn and surrounding material attached to a TEM grid. (b) The EBSD orientation map of the column, along with (c) the corresponding pole figure and (d) point-to-point (red) and accumulated (blue) misorientation profile along a white arrow of (c). RD and LD in orientation map are radial direction and loading direction, respectively.

In order to investigate the actual slip and potential twinning activity, thin foils were fabricated by FIB milling, as described in the preceding chapter. The step by step process for one of the c-axis compression columns is shown in Figure 4.3. The subsequent EBSD analysis of this foil is presented in Figures 4.4 and 4.5, confirming the non-existence of deformation twinning. The results show the localized rotation of the crystal due to dislocation plasticity, where the rotation axis is [10-10]. The misorientation of the column was increased up to 9 degrees along the loading axis of the column (Figure 4.4(d)). The EBSD study of the column showing a massive strain burst is shown in Figure 4.5. The image of the deformation shown from the top of the column is given in Figure 4.5(a) and its cross-sectional structure is shown in Figure 4.5(b). While the boundary between the column and the massively sheared out section is not clearly identifiable in the SEM image due to damage from FIB milling, the boundary orientation is confirmed by EBSD mapping, as shown in Figure 4.5(c). The EBSD map shows that the massive slip occurred along the basal plane and that no twinning occurred even after the massive slip. The misorientation of the bottom section of the column measured along the white arrow in Figure 4.5(c) is 5 degree.

48
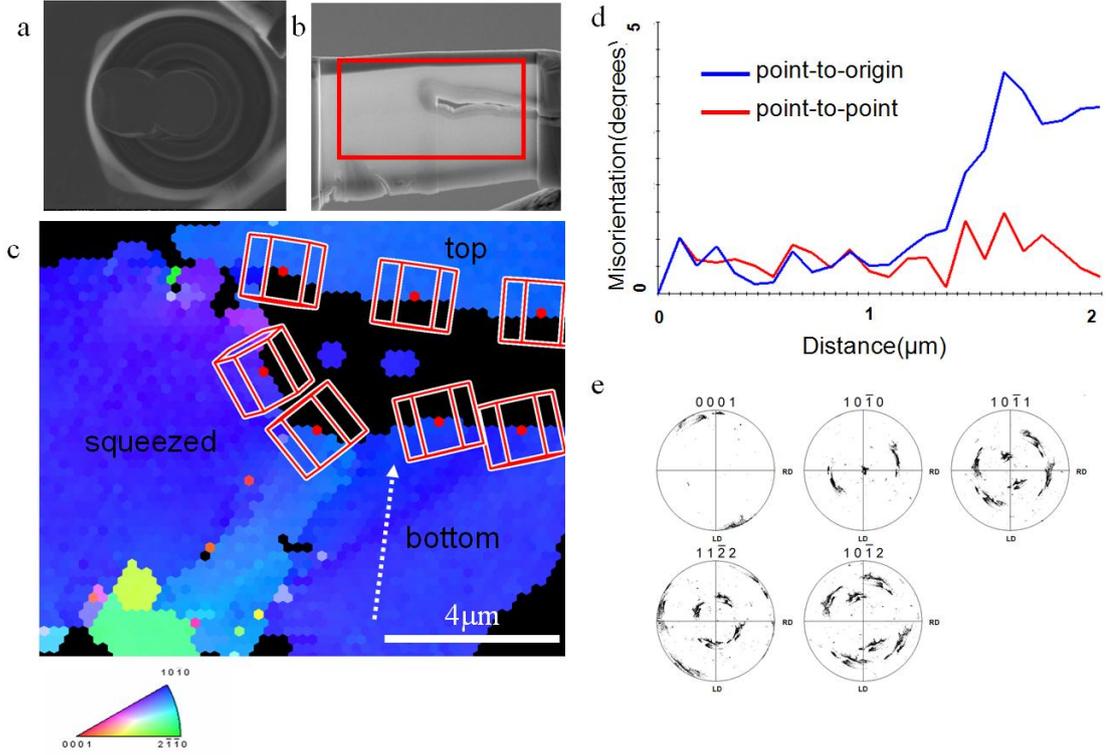
Figure 4.5: EBSD observations of a column having undergone massive, unstable slip. (a) A plan-view SEM image of the deformed column and (b) an SEM of the thinned out cross section through the column. (c) The EBSD orientation map showing the lattice rotations along with the associated (d) misorientation profile and (e) pole figures. RD and LD in orientation map are radial direction and loading direction, respectively.

In order to investigate the effect of the crystallographic rotation of the column on the activation of basal slip during deformation, we can consider the schematic shown in Fig 4.6(a). Here, we see that the normal to the basal plane is rotated by an angle, α, relative to the [0001] loading axis. The required applied stress, σ, for the activation of the basal slip system is calculated based on this misalignment angle, α, and the critical resolved shear stress for basal slip, τ_{crss} . It is well known that the resolved shear stress, τ, due to an applied stress, σ, on a plane with normal oriented an angle α relative to the loading axis and a slip direction oriented an angle of $(\alpha + 90)$ from the loading axis is given by:

$$\tau = \sigma \cos\alpha \cos(90 \pm \alpha). \qquad (4.1)$$

When $\tau = \tau_{crss}$, basal slip will be activated. Substituting $\tau_{crss} = 0.5\text{MPa}$ for the critical resolved shear stress of basal slip as suggested by previous studies ([Yoshinaga *et al*. 63], [Burke *et al*. 52]) the minimum applied stress for the activation of basal slip as a function of misalignment angle is given by:

$$\sigma = 0.5\,\text{MPa}/\left(\cos\alpha\cos\left(90 \pm \alpha\right)\right), \qquad (4.2)$$

which simplifies to:

$$\sigma = \pm \frac{1\,\text{MPa}}{\sin 2\alpha}. \qquad\qquad\qquad\qquad (4.3)$$
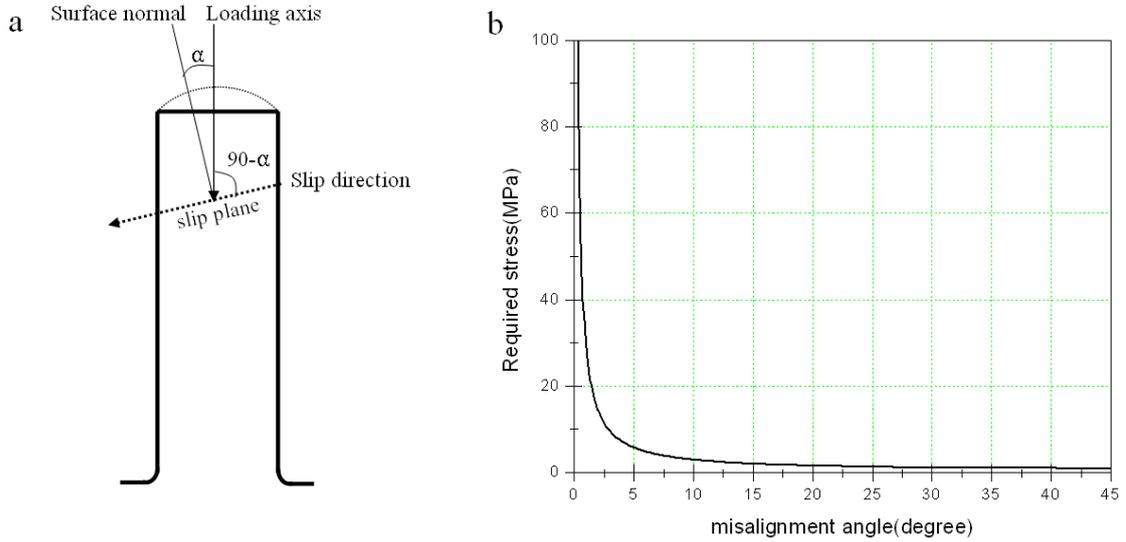
Figure 4.6: (a) Schematic showing a column and basal slip plane with plane normal at an angle of α from the loading axis. (b) Required applied stress for the activation of basal slip as a function of misalignment angle, assuming a CRSS of 0.5 MPa.

According to equation (4.3), the required applied stress for the activation of basal slip is 57.3 MPa with 0.5 degree misorientation, and only 14.3 MPa for a 2 degree misorientation (maximum experimental misalignment, as discussed in Chapter 3). Considering the stress-strain response shown in Figure 4.1, it therefore seems very likely that basal slip is activated at the very early stage of deformation. However, the stress increases up to 250MPa prior to a significant slope change, a value nearly 5times larger than the required stress of the 0.5degree misorientation case. Clearly, basal slip is not the governing mechanism of deformation or we would never have achieved such high stresses. Therefore another slip system must be active. Furthermore, basal slip alone cannot accommodate the resultant longitudinal strain given the little lateral displacement observed. If we consider the resolved shear stress on the pyramidal $\pi 2$ slip systems, which has the only non-zero Schmid factor with a value of 0.45, a 250 MPa applied stress would required a CRSS of 112.5 MPa.

In the hardening stage, the increase of the density of <c+a> dislocations associated with the 6 equivalent pyramidal $\pi 2$ slip systems results in strong dislocation junction formation. A high density of <c> component dislocation of the 6% deformed column has been observed in the TEM, as shown in Figure 4.7. While the increase of the stress due to the activation of the <c+a> dislocation and junction formation, the local misorientation of the

column would be increased with deformation process. Finally, the massive strain burst is associated with the escape of dislocations on the basal slip system when the applied stress is sufficient to overcome the forest of dislocations produced on the pyramidal slip system.
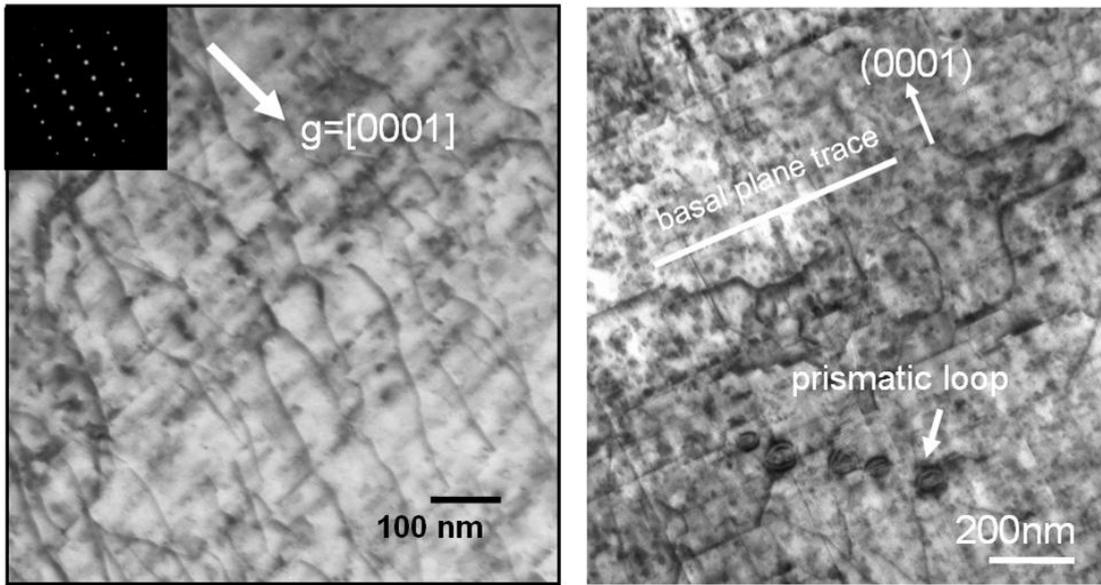
Figure 4.7: TEM shows <c> component dislocation. The zone axis is [2-110]. Prismatic loops were only observed when g=[0001].

Another important observation is the existence of prismatic loops, as shown in Figure 4.7(b). The prismatic loops were only found when g=[0001]. These prismatic loops may be the signature of pyramidal glide ([Legros *et al*. 97A], [Legros *et al*. 97B]).

In summary of the results for the c-axis compression experiments, the basal slip system might be activated at the early stage of the deformation due to its low CRSS but the extent of basal slip is not sufficient to accommodate the observed longitudinal strains. Rather, hardening results from the activation and multiplication of <c+a> dislocations on the 6 equivalent pyramidal π2 slip systems and the resultant junctions formed between the basal <a> dislocations and the pyramidal <c+a> dislocations. Due to the local misorientation of the column evolving from the plasticity and the increase in applied stress, a massive basal slip occurs when the stress on basal <a> dislocation is sufficient to overcome the junction stresses resulting in a mid-section of the column shearing out of the column in a catastrophic manner.

## 4.2 [2-1-12], [10-11] compression tests

In order to investigate the slip activities of basal slip, it is necessary to study the basal slip favorable orientation. Two different kinds of so-called "45 degree" samples have been studied, where the normal to the basal plane is oriented 45 degrees relative to the compression axis. The longitudinal axes of [2-1-12] and [10-11] give a Schmid factor of the basal slip

system with a value of 0.5, as shown in Table 2.4.

The stress-strain responses of the [2-1-12] and [10-11] orientations are shown in Figure 4.8. The applied stress was increased until a strain burst occurs at the stress level of 20~30MPa. Note that 30MPa is already 30 times larger than the expected required stress for basal slip (1MPa) with 45 degree (Figure 4.6(b)). This much higher value is likely due to the size effect in flow stress observed almost universally in single crystalline metals, and as will be discussed further in Chapter 5. Furthermore, this higher than expected value of critical resolved shear stress supports our observation that basal slip is not dominant in [0001] oriented compression during the pre-critical deformation despite sufficient stresses assuming a critical resolved shear stress of 0.5 MPa, as discussed previously. Following equations (4.1-4.3), if we replace the critical resolved shear stress with a value of 30 x 0.5 MPa = 15 MPa, we find that basal slip is not expected to be dominant in the [0001] orientation within 2 degrees misorientation until the applied stress reaches 215 MPa. Considering that pyramidal slip is already active at this stress, the stresses required for overcoming the junctions formed will be even higher. This supports the observation that massive basal slip is not activated during [0001] compression until stresses reach nearly 600 MPa.

With the same lettering given in Figure 4.8, SEM images of the deformed columns are given in Figure 4.9. As shown in Figure 4.8, the surface morphology of the column changes when there is a change in the slope of the stress-strain curve. For example, in the case of column (i) in Figure 4.8 and 4.9, with a small change of the slope at the stress level of 20MPa, a slip step forms on the surface of the column; deviations in the stress-strain curves are associated with discrete slip bands in the columns.

Some SEM images of deformed column are shown in Figure 4.10. The slip marks caused by the massive basal slip is imaged in Figure 4.10(a) and (b). In addition, the wavy topology of the slip plane is shown in Figure 4.10(c) and (d). This is caused by the massive slip.
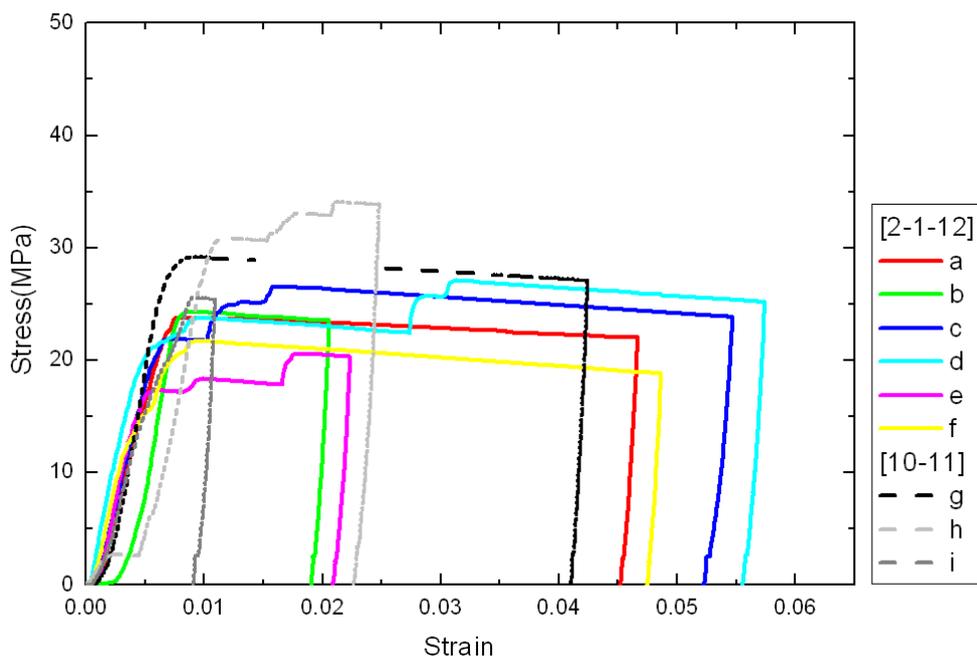
Figure 4.8: Stress-stain curve of [2-1-12] and [10-11] orientation.
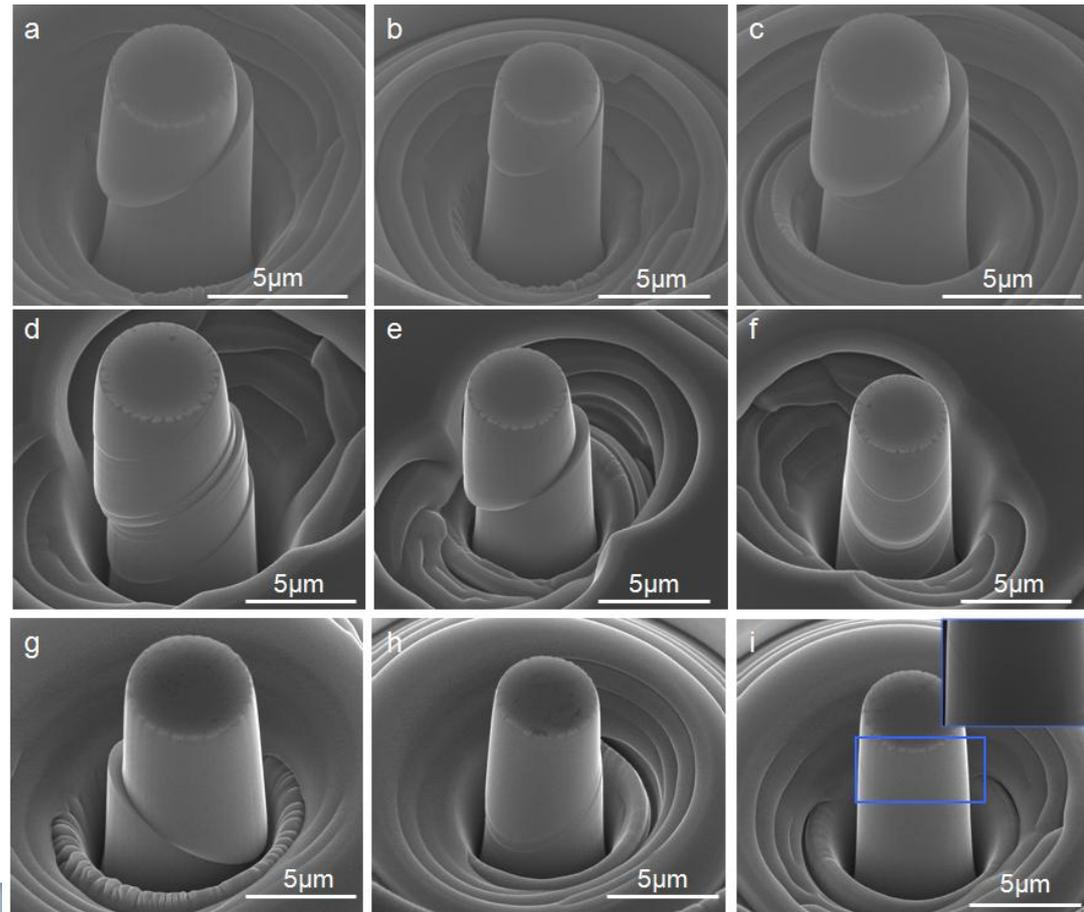
Figure 4.9: SEM micrographs of the post-compression microcolumns associated with the stress-strain curves given in Figure 4.8.

A thin foil for EBSD and TEM has been prepared after [2-1-12] orientation compression testing to check the existence of twinning and to confirm the loading axis orientation. With the column shown in Figure 4.11(a), cross sectioning has been performed, and we carried out EBSD analysis as shown in Figure 4.11(b). EBSD results indicate that twinning has no contribution to the strain accommodation and the loading axis is well aligned at an angle of 45degrees from the basal slip.
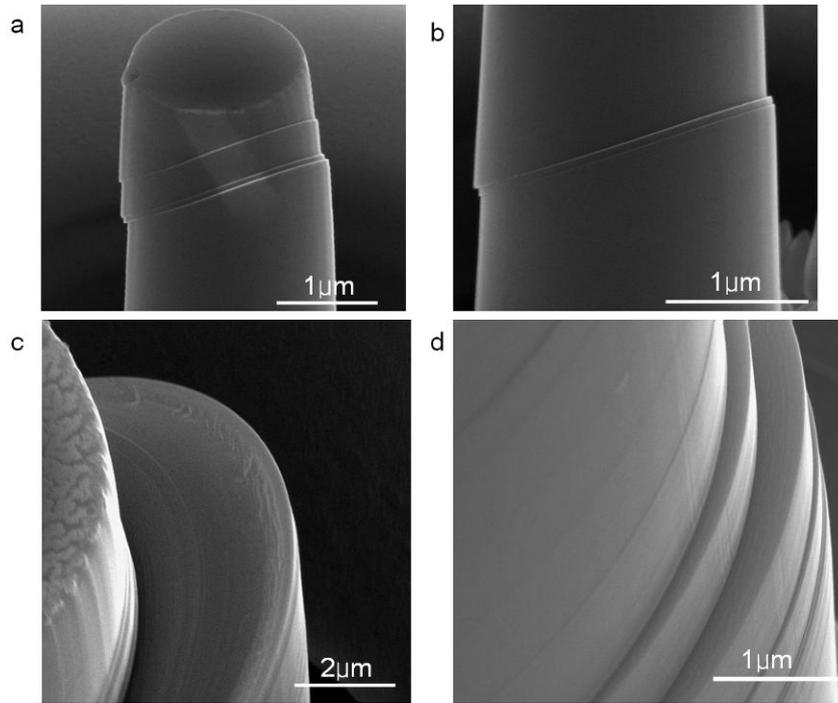
Figure 4.10: SEM images of slip steps occurring from compression in the 45 degree orientation columns. Images are taking from a tilted angle such that the slip lines do not show a 45 degree angle in-plane.
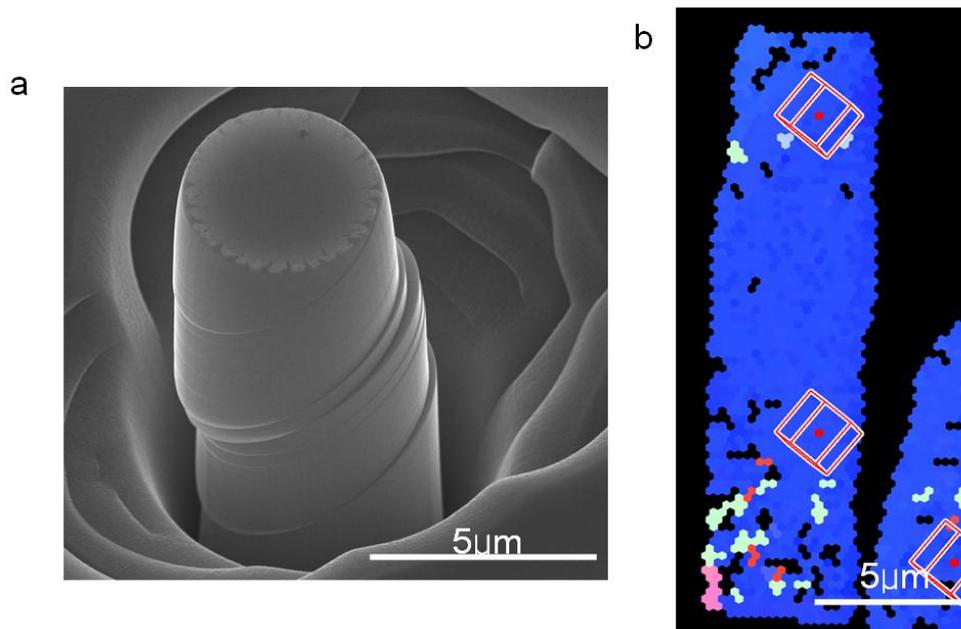
Figure 4.11: An SEM image of a typical deformed [2-1-12] column is shown in (a). EBSD shows no twin in the deformed region, and confirms that the sample is loaded in a direction 45 degrees to the basal plane normal.

TEM was used to investigate the dislocation activities in the samples. A dislocation analysis was carried out using the dislocation extinguish condition. As was discussed in

Chapter 3.4, the Burgers vector can be identified by comparing dislocation features using different diffraction conditions. Here, a TEM foil was prepared with the zone axis of [1-100] and the dislocation features using [11-20], [0001], [11-21] diffraction vectors are compared (Figure 4.12). A qualitative analysis shows that the density of the <c> component dislocations (e.g. <c>, <c+a>) is relatively low, which means the inherent <c> type dislocation content is not large. Since all oriented samples have been fabricated from the same bulk crystal, we can be assured that the <c> component dislocation content found in the [0001] compression columns is a result of deformation, rather than initial content. Cross slip is found, between the basal and prismatic planes. This is not surprising since the Schmid factor on the prismatic system is not zero.
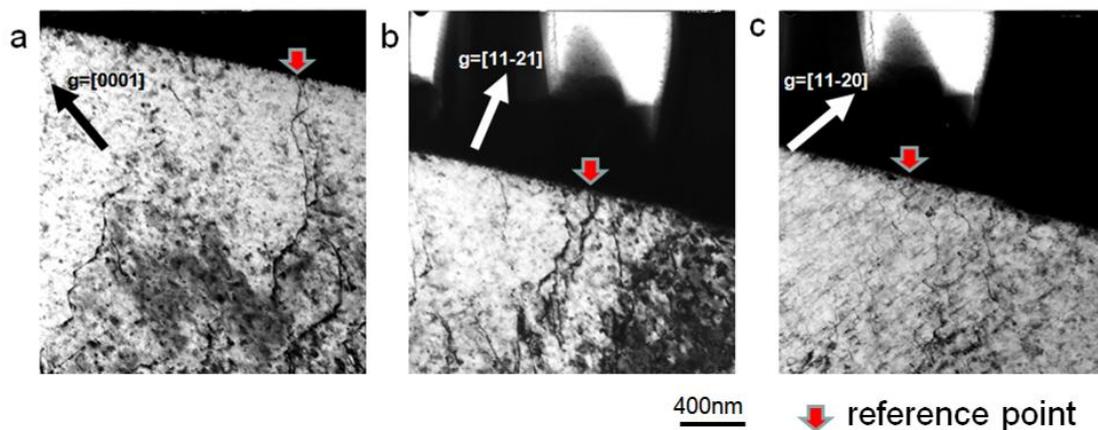
Figure 4.12: The dislocation extinction condition analysis by different diffraction conditions identifies the observed dislocation in (a) and (b) as <a> dislocations. The zone axis is [1-100].

Figure 4.13 shows the dark field image of dislocations lying on the basal plane. A large number of <a> dislocations have been observed. In this case, although we carefully tried to observe the dislocation features, we failed to find the same position after tilting the specimen. In the case of a pure, single crystalline sample, it is hard to do dislocation extinguish analysis due to the lack of a reference point (e.g. grain boundary, precipitate). As shown in Figure 4.12, if we ignore the inherent <c> component dislocations, it is concluded that the dislocations in Figure 4.13 nearly all basal <a> dislocations.

As already stated, previous studies have suggested that the CRSS of the basal slip system is 0.5MPa ([Burke and Hibbard 52], [Yoshinaga and Horiuchi 63]). Recently, the measurement of the CRSS has been carried out experimentally through compression testing of bulk specimens ([Bian and Shin 09]). Their results suggest that the CRSS for basal slip is 0.61MPa as indicated by a slope change in the stress-strain curve at this stress level. However, the determination of the CRSS by compression testing seems to be in dispute. The resolved shear stress and strain of just the early stage of deformation during a microcompression test is shown in Figure 4.14. Although a change in slope at 0.5MPa is observed in this test, it is not sufficient to conclude that basal slip is activated at this stress. Since full contact usually does

not occur until deformation progresses some finite amount, it is more likely that changes in slope of the stress strain curve relate to the evolving contact. In the same curve, the CSM modulus is plotted and shows that the modulus is increasing during this initial deformation range, indicating that full contact is still evolving.
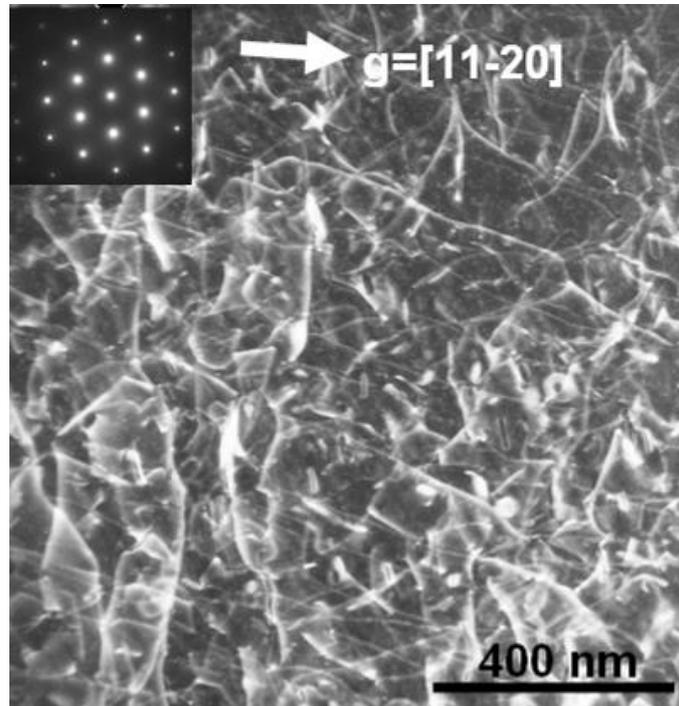
Figure 4.13: The dislocation structure on the basal plane resultant from compression of a [10-11] oriented column. Each of dislocation has the Burgers vector of <a> or <c+a>.
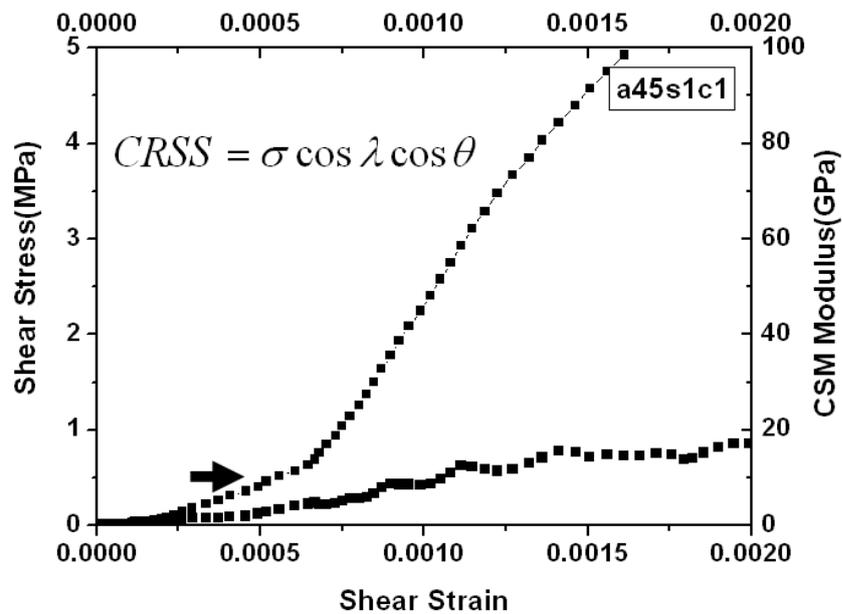
Figure 4.14: A plot of resolved shear stress (small squares) and CSM modulus (large squares) during the initial compression of a column oriented 45 degrees from the basal plane. An estimation of the CRSS of the basal slip system by identifying deviations in the slope of the stress-strain curve is complicated by the evolving contact inherent to compression testing.

4.3 [11-20] compression tests

The engineering stress-strain curves of 6 micro-columns with nominal diameter of 5µm loaded along the [11-20] axes are shown in Figure 4.15. In three of the six columns, it is shown that a critical point occurs at around 1% strain, leading to a massive strain burst. The associated deformed columns are shown in the SEM micrographs given in Figure 4.15. The elastic modulus can be analyzed from the unloading data associated with the three experiments run to approximately 1% strain. Such an analysis of the three curves displaying large strain bursts is obviated by the large shape change due to the strain burst. Twinning is indicated in the SEM micrographs as dark bands, as in Figure 4.16(a). This is not surprising since tensile twinning and prismatic slip are expected mechanisms of plastic deformation for [11-20] compression according to the Schmid factors given in Table 2.4. As will be shown, TEM and EBSD analyses confirm the presence of twining and the correspondence of twins to the dark bands. Note that the twin has been observed even prior to the strain burst. During deformation, a single nucleated twin propagates through the whole column, and massive slip occurs in columns which were loaded past the critical point, such as in Fig 4.16 (d), (e), (f). SEM images from different points of view of one deformed column are shown in Figure 4.17 to provide a more detailed picture of the deformation morphology typical of these columns.
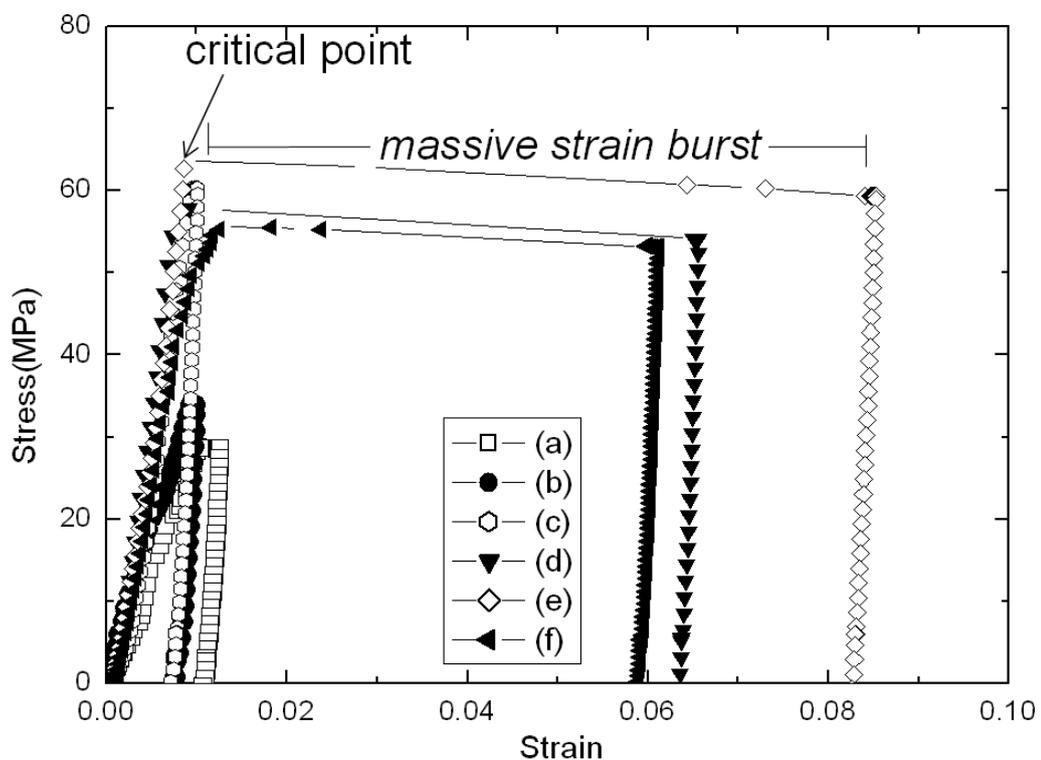
Figure 4.15: Stress-strain responses of [11-20] orientated columns
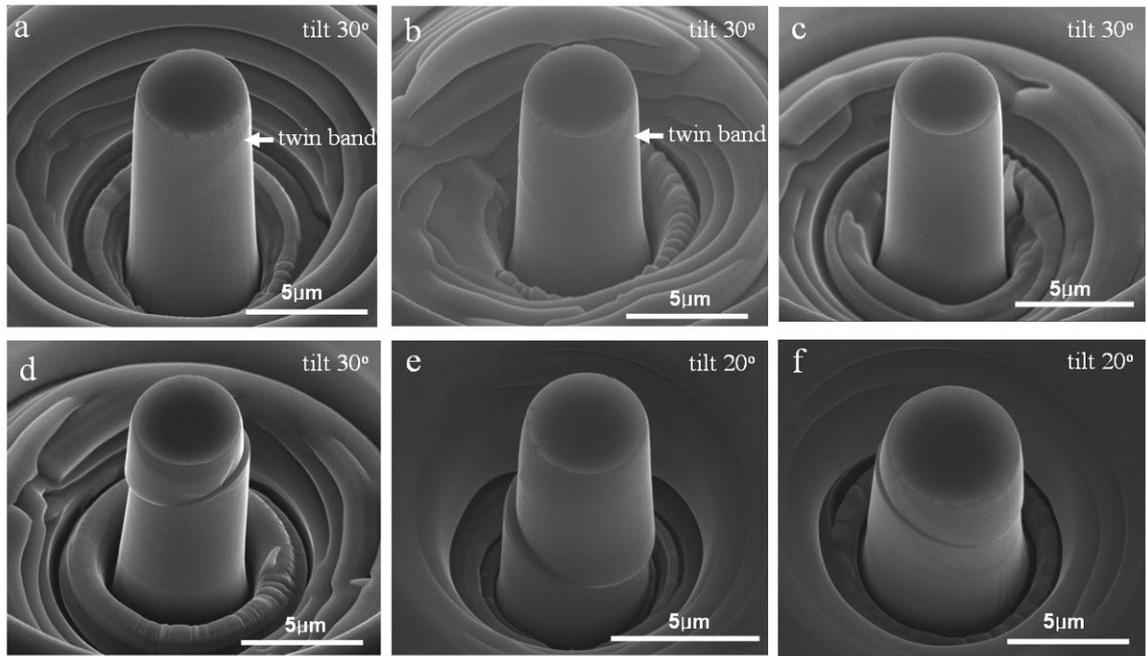
Figure 4.16: SEM images of deformed columns. Each column (a)-(f) corresponds to the stress-strain response of the same letter designation given in Figure 4.15.
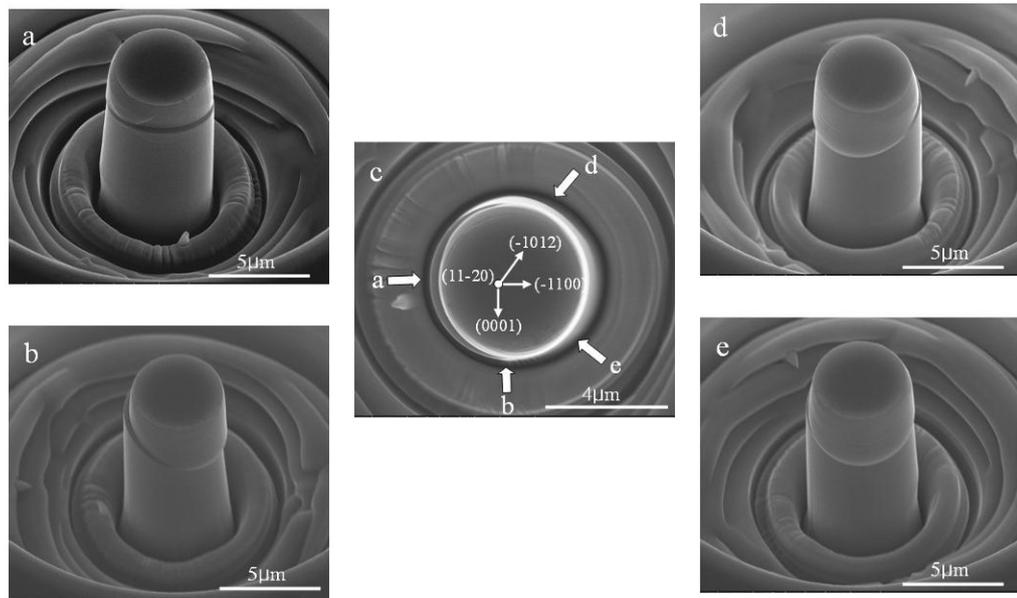
Figure 4.17: SEM images of a deformed column from different points of view, as indicated.

In order to investigate the contribution of the twin to the plastic strain along compression axis as is measured in the stress-strain curve, we need to consider the longitudinal strain due to the twinning shear, as is given by:

$$\varepsilon = VM\gamma ,\tag{4.4}$$

where, V is volume fraction of the twin, M is the Schmid factor, and γ is the shear strain due

to twining. The twinning shear, γ, for magnesium is 0.129 (c/a=1.624) ([Yoo 81]). If the entire column is twinned, this would lead to an axial strain of 0.048 from twinning alone. However, since the critical point occurs at a strain of about 1%, it is clear that the entire column has not been twinned at this stage. Therefore rapid twin propagation must be involved during the strain burst. In other words, basal slip does not account for the entire burst strain.

It is still unclear why the strain burst occurs at around 1% deformation. In order for massive basal slip to occur across the entire diameter of the column, a critical thickness of twin is required. This is shown schematically in Figure 4.18. Using geometric arguments, and knowledge of the original orientation of the column and that of the twin, we can define the critical thickness as follows.

Figure 4.18: Schematic of a microcolumn used to compute the critical twin thickness needed to activate a basal slip band which extends across the entire column diameter.

A pillar with 5μm diameter and 15μm height has been used for the calculation of the critical twin thickness. Figure 4.18 shows the cross section image of pillar with (0001) out-of-plane direction of matrix. We can calculate the volume fraction of the twin using the area fraction from the given cross section. The angle between the twin plane and the loading axis is 120 degrees. Once the twin nu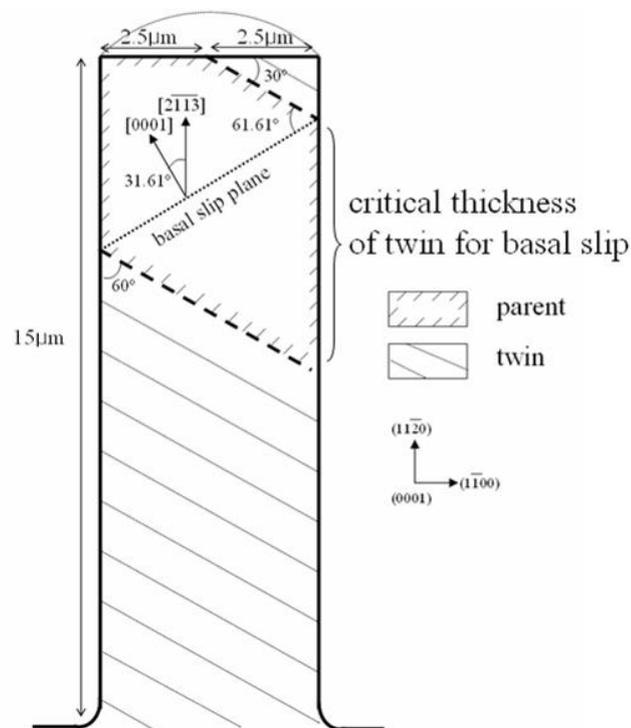cleates, the loading axis of the twin is changed to [2-1-1-3] and the angle between the new loading axis and the basal plane is 31.61 degrees. With this simple calculation, it is deduced that 37.3% of column should be twinned before a basal slip band can extend across the entire diameter of the column. With the calculation by equation 4.4, the minimum longitudinal strain associated with this critical twin thickness is 1.8%, well beyond the observed strain of 1% at which the strain burst occurs. Therefore massive basal slip does not account for the critical point at which the strain burst occurs.
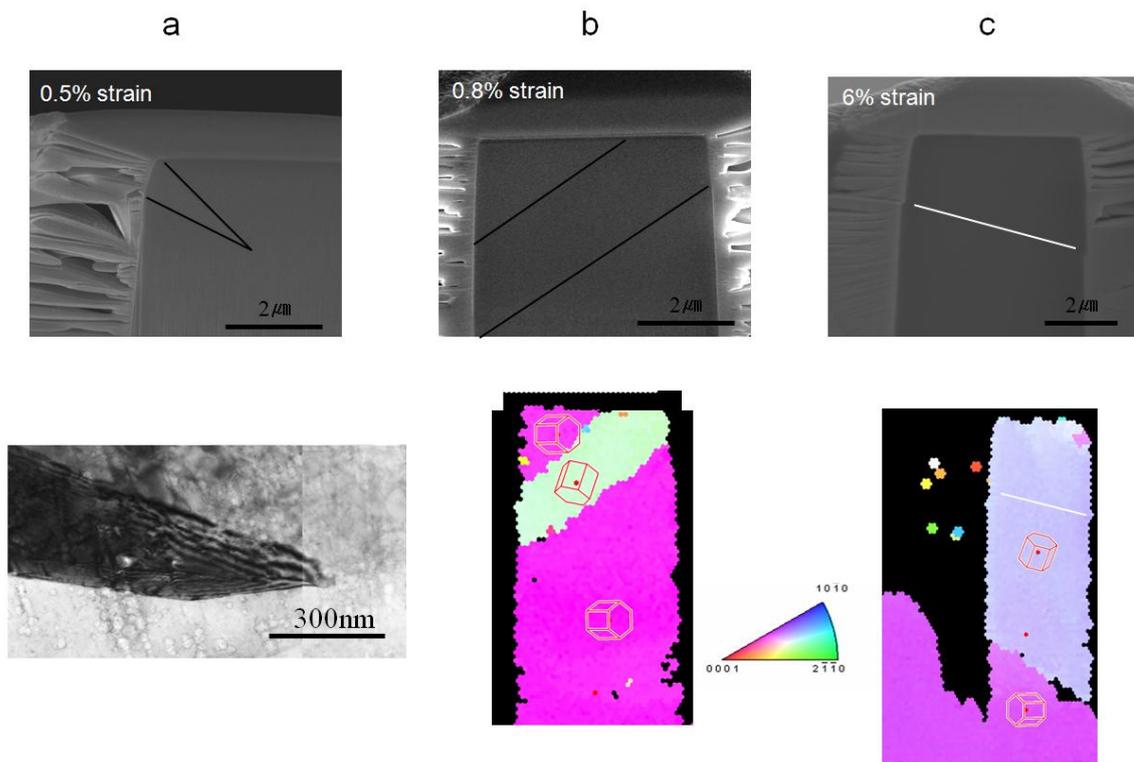
Figure 4.19: Deformation proceeds by (a) twin initiation (b) twin propagation and (c) massive basal slip

It is well known that twins initiate via the sequential formation and propagation of stacking faults ([Partridge 67], [Morozumi *et al*. 76]). EBSD and TEM of cross-sections from the column show twin initiation and propagation, as shown in Figure 4.19. It should be noted that columns designated by (a), (b), (c) in Fig 4.10 correspond to the stress-strain curves designated (a), (b), (d) in Figure 4.15, respectively. Twinning initiates at the early stage of deformation, prior to the critical point. The twin tip with a needle-like shape in the (10-12) twin habit plane has been observed (Figure 4.19(a)). The twins always are observed to nucleate at the top the column, expectedly due to the stress concentration between the indenter tip and column. Only a single twin is observed to nucleate per column. The twin propagates downward in a gradual manner initially, as indicated by the increasing stress needed to propagate the twin until the critical point. Importantly, it is observed in Figure 4.19(b) that the twin has extended across the entire diameter of the column, but is still stable; this configuration is not a critical state associated with the strain burst. After the massive strain burst, nearly the whole column is twinned and a massive basal slip band is observed, as shown in Figure 4.19(c) at a total strain of 6%. It was initially envisaged that the critical point marked the transition from twin propagation across the diameter, where matrix constraint could strongly hinder twin growth, to unconstrained propagation along the column axis after the twin extended across the full diameter. However, the observation shown in Fig. 4.19(b) indicated that other factors beyond matrix constraint control a transition between slow twin propagation and unstable twin propagation, as is associated with the strain burst.
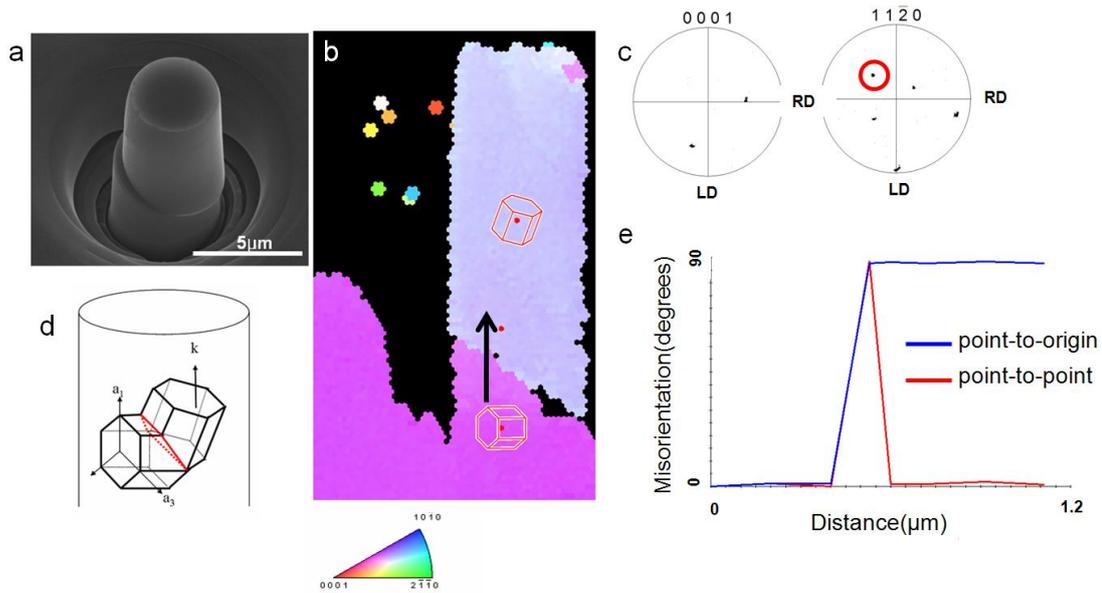
Figure 4.20: (a) SEM image of a deformed column initially oriented along the [11-20] loading axis showing massive basal slip. The associated (b) EBSD map, (c) corresponding pole figure, (d) relationship of the twin and parent orientations, and (e) misorientation profile showing the resultant twinned structure. RD and LD in orientation map are radial direction and loading direction, respectively.

The crystallographic orientation of the twinned column is shown in Figure 4.20. The orientation is changed with the rotation axis of [11-20] and the misorientation angle is 87.2°. The twin is oriented favorably for basal slip, with the compression axis aligned along the [2-1-1-3] direction, allowing massive basal slip to occur at a critical twin thickness.

Interestingly, <a> dislocations on the prismatic plane have been observed within the untwinned region, as shown in Figure 4.21. Although it is unclear how competitive the two mechanisms are, it is clear that both twinning and prismatic slip account for the initial deformation during [11-20] oriented compression. It has been previously reported that the CRSS of the prismatic slip system is much higher than that for basal slip at room temperature ([Ward Flynn P *et al*. 61]). However, prismatic slip has been reported in the case of Mg alloys ([Agnew and Duygulu 05]). Since the Schmid factor for basal slip is effectively 0 for this orientation, and the critical resolved shear stress for pyramidal slip is reportedly higher than for prismatic slip, it is not surprising that prismatic slip occurs here. The observations also indicate that prismatic slip is favorable to additional twin nucleation throughout the column. As will be discussed, the activation of prismatic slip affects the resultant dislocation structure observed within the twin, and may play a role in twin propagation.
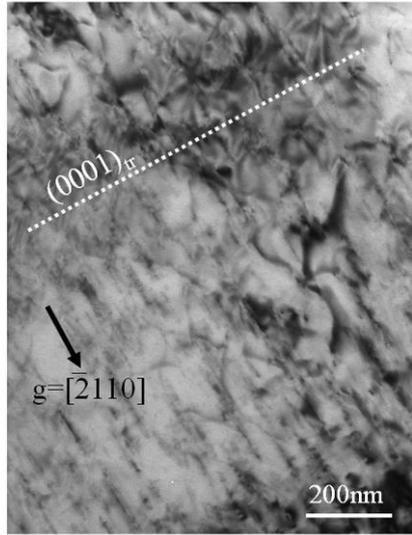
Figure 4.21: <a> type dislocations on the prismatic plane within the untwinned region of a compressed [11-20] oriented column. The zone axis is [0-110].

Another interesting observation is the observation of <c> component dislocations within the twin at the early stage of deformation as well as within the fully twinned structure, as shown in the weak beam dark field TEM micrograph given in Figure 4.22. <c> dislocations are related to crystal growth or debris of dislocation interactions. Observations of <c>-type dislocations have been reported previously ([Morozumi *et al.* 76], [Agnew and Duygulu 05], [Song and Gray 95]). In the case of Zr, Song and Gray proposed that <c> dislocations are trapped in the twinned region because of the dislocation reactions governing twin propagation. Morozumi *et al.* observed <c+a> dislocations in the twinned region in Mg, and proposed a specific mechanism by which <a> type dislocations are transformed to <c> type dislocations and twinning dislocations. While one of the possible three <a>-type dislocations of screw character can be activated within twin because the parent and twin share the same Burgers vector, the other 2 type of <a> dislocations will be transformed according to equation (4.5):

$$2 \times \tfrac{1}{3}\left[1\bar{2}10\right]_m \rightarrow -2b_t + \tfrac{1}{3}\left[11\bar{2}\bar{3}\right]_t \rightarrow -2b_t + \tfrac{1}{3}\left[10\bar{1}0\right]_t + \tfrac{1}{3}\left[01\bar{1}0\right]_t + \left[000\bar{1}\right]_t, \qquad (4.5)$$

where b_t is unit vector of twinning.

Figure 4.23 shows the (11-20) atom projection for Mg. In order to understand the twin mechanism and dislocation transformation due to the twinning, a geometrical calculation about the atom location and translation has been carried out. The coordinates of the matrix atoms are given in black and the coordinates of the twin atoms are given in red. The distance of the two black circles along [0001] direction is 1.624Å and the distance along [01-10] is 1.732Å which corresponds to √3 Å. The black dot-circle is the original atom location and the red-circle indicates the translated atom due to twinning. According to the definition of the

twin, once an atom is twinned on the twin habit plane of (10-12), the atom (①) should translate a certain distance along the [10-11] direction, and the translated atom (②) should be located at the mirror position with the atom (③). The strain introduced by the translation of the atom movement from ② to ③ is 0.065. The twinning shear of the (10-12), [10-11] twinning system is 0.129. However, as was discussed in Chapter 2, due to the double lattice character (ABABAB…), 4 interatomic layers are needed to completely satisfy the twinning shear of 0.129. As shown in Figure 4.21, twinning shear introduced by the translation from atom (④) to (⑤) is 0.129. Although the extent of atom translation is not large, the crystallographic axis is rotated 87.2degree (comparing the [0001] axes of matrix and twin).
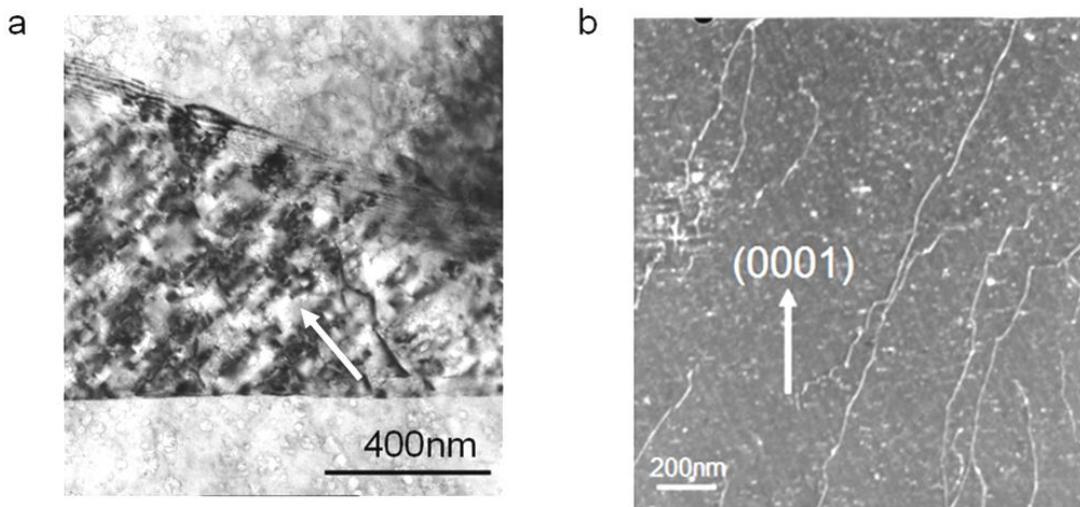
Figure 4.22: <c> component dislocations are observed in (a) a twin at the early stage of deformation, as well as in (b) the twinned region after the whole column is twinned.
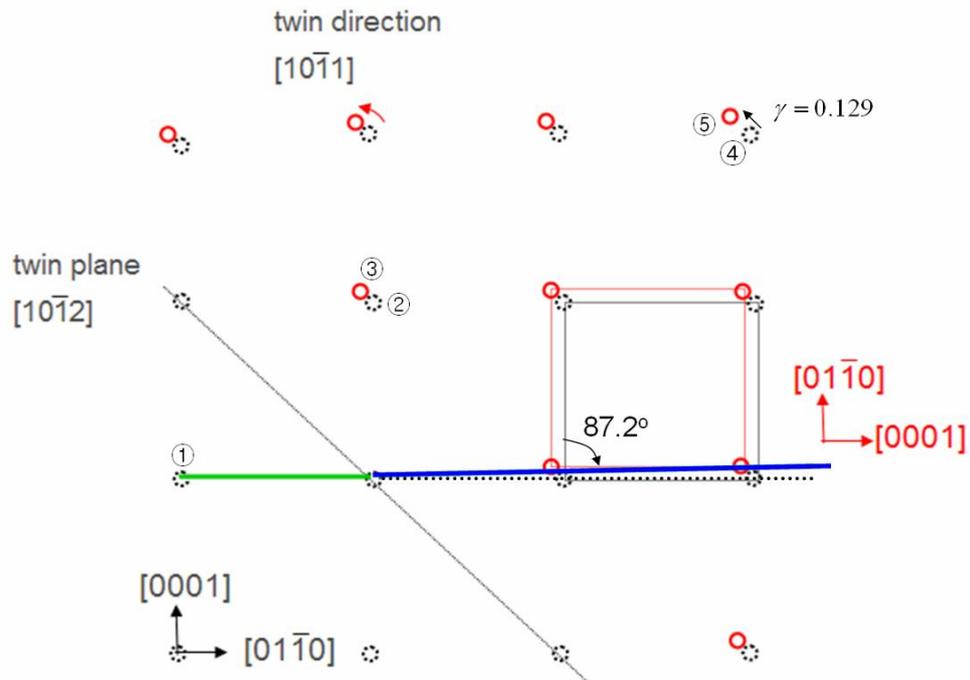
Figure 4.23: Formation of <c> component dislocation from transforming of the <a> type dislocation.

In figure 4.23, the green line is the initial dislocation existing in matrix. If twinning occurs the dislocation line direction will be changed to the blue line. However, the new coordinate reveals that the dislocation in the twinned region is not on the [01-10] axis, but instead lies on the [0001] axis. In conclusion, the <a> dislocations generated by prismatic slip, as shown in Figure 4.17, would be transformed to <c> dislocations after twinning.

As mentioned previously, a massive strain burst occurs at about 1% strain, and cannot be fully explained by the activation of massive basal slip; a minimum strain of 1.8% is required in order to activate basal slip across the entire diameter of the column. This implies that the twinning process evolves via nucleation followed by a slow growth phase of the twin accompanied by increasing stress, and then a phase of rapid twin propagation. In order to investigate the twin evolution and the associated rate dependencies, we have considered the microstructural changes within the column due to the twin using TEM analysis. In order to investigate what happens during twinning, three different columns with varying strain (5.5%, 10.8%, and 12.3%) are chosen, as shown in Figure 4.24. The figure also shows the associated stress-strain responses for these columns, identifying a varying number of massive strain bursts which seem to correlates to the number of massive slip steps observed in the micrographs.
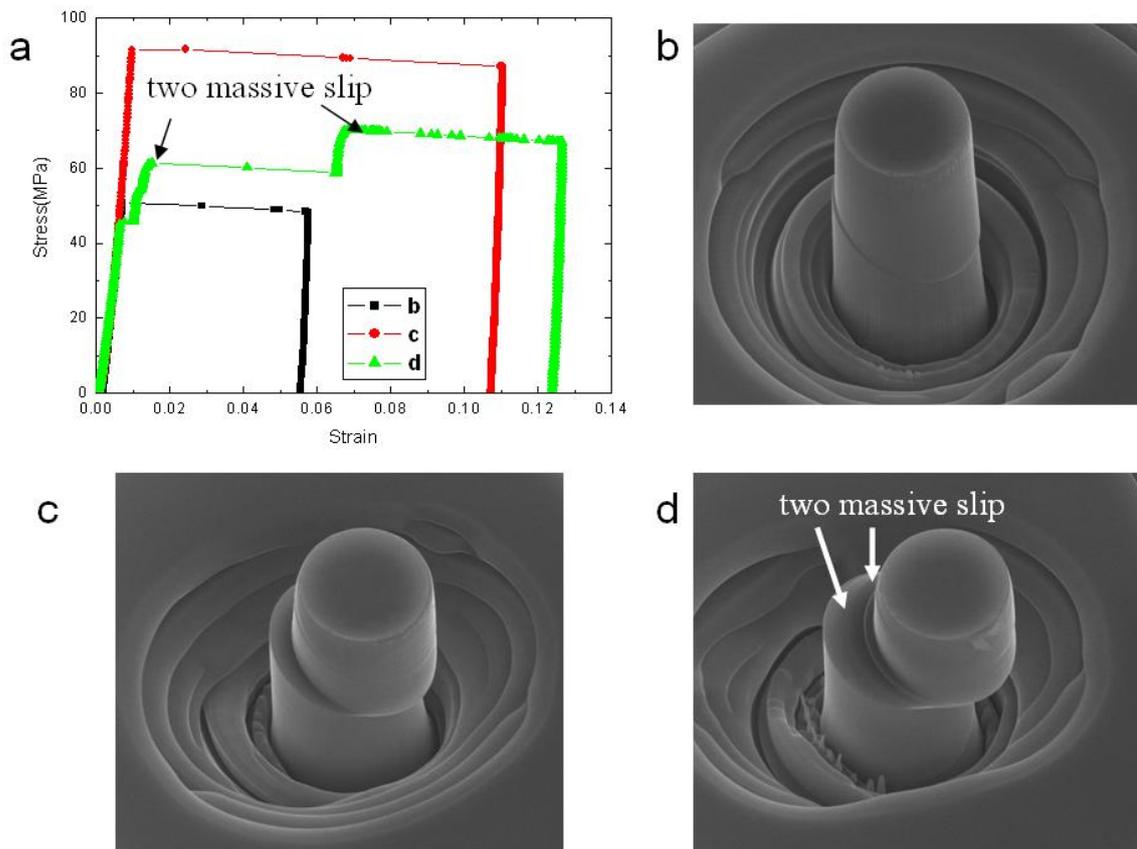
Figure 4.24: Three stress-strain curves and their corresponding SEM images of deformed columns from [11-20] compression.

TEM foils have been prepared from twinned columns according to the method described in Figure 3.6. TEM foils have been prepared at the top, middle and bottom part of the column with the foil plane normal of [0001] to study the microstructure with the twin propagation as shown in Figure 4.25.
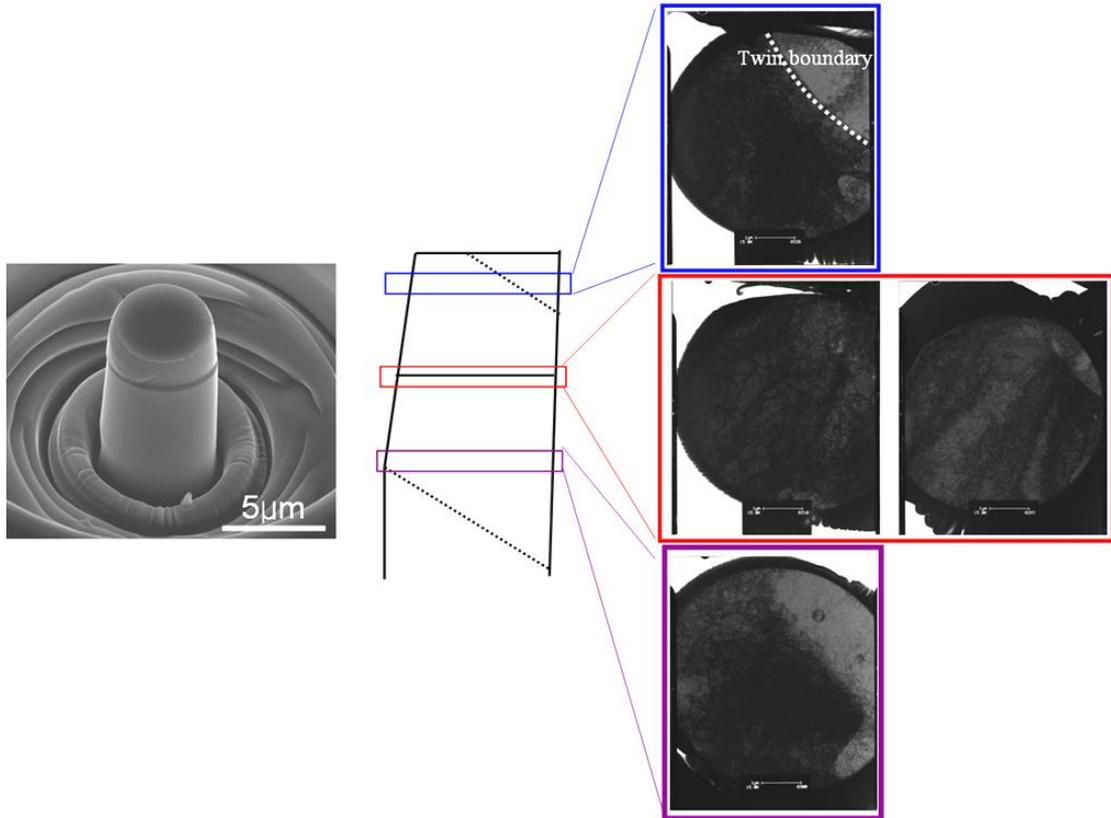
Figure 4.25: A compressed column which has been sectioned for TEM analysis in three positions along its compression axis, along with a schematic identifying the TEM foil positions relative to the twinned region, and TEM images from the three foils.

Figure 4.26 shows the boundary between the twinned and untwinned regions, and their associated diffraction patterns. Subgrains have been observed in the twinned region, and not found in the untwinned region. As is well known, twinning proceeds by the translation of atoms. However, due to the local dislocation plasticity (e.g. prismatic slip), atom translation does not proceed uniformly, and therefore sub-grains are formed simultaneously. Subgrains appear or disappear during the TEM analysis depending on the tilting condition indicating that they have low angle boundaries. Since no subgrains were found in the untwined region, it is unlikely that they were present in the initial material prior to deformation. Figure 4.27 shows the defect structure within the basal plane at the top middle and bottom of a twinned column. It is shown that the size of the sub-grains increase along the compression axis, with the finest subgrains present at the top of the column.

In addition to the longitudinal variation in the subgrain size, the taper of the microcolumn geometry introduces a longitudinal variation in the stress; the stresses are

highest at the top. In order to develop a picture of how the twinning and plasticity evolve, and importantly what dictates the critical point at which the strain burst occurs, it is important to consider both of these variations along the compressive axis. Once the twin is nucleated, stresses on the basal slip system are sufficient to activate slip. However, due to the large number of subgrains, and the limited thickness of the twin, massive basal slip is hindered. The propagation of the twin is also hindered by the subgrain structure and may lack the required dislocations to "feed" the twin front, even after the twin has been extended across the entire diameter of the column. Furthermore, the further down the twin propagates the smaller the applied stress is due to the column taper. Thus higher stresses are required to continue deformation. However, as the sub-structure becomes coarser further along the axis, the twin is less hindered. At the same time, the increase in applied stress providing a larger driving force for twin propagation. At some optimum configuration the resistance to twin propagation is no longer greater than the stress driving twin propagation. The twin becomes unstable since further propagation becomes continually easier due to the ever coarser sub-grain structure. Therefore, it is proposed here that the sharp transition from slow to rapid twin propagation is dictated by the ability of the twin to propagate through the subgrain structure which pins the twin at the subgrain boundaries. Once the twin becomes unstable, the critical twin thickness for massive basal slip is reached, and the stresses acting on the basal system are well above the required stress to activate massive basal slip. The size of the large strain burst is therefore due to both the strain associated with rapid twin propagation and that from massive basal slip.
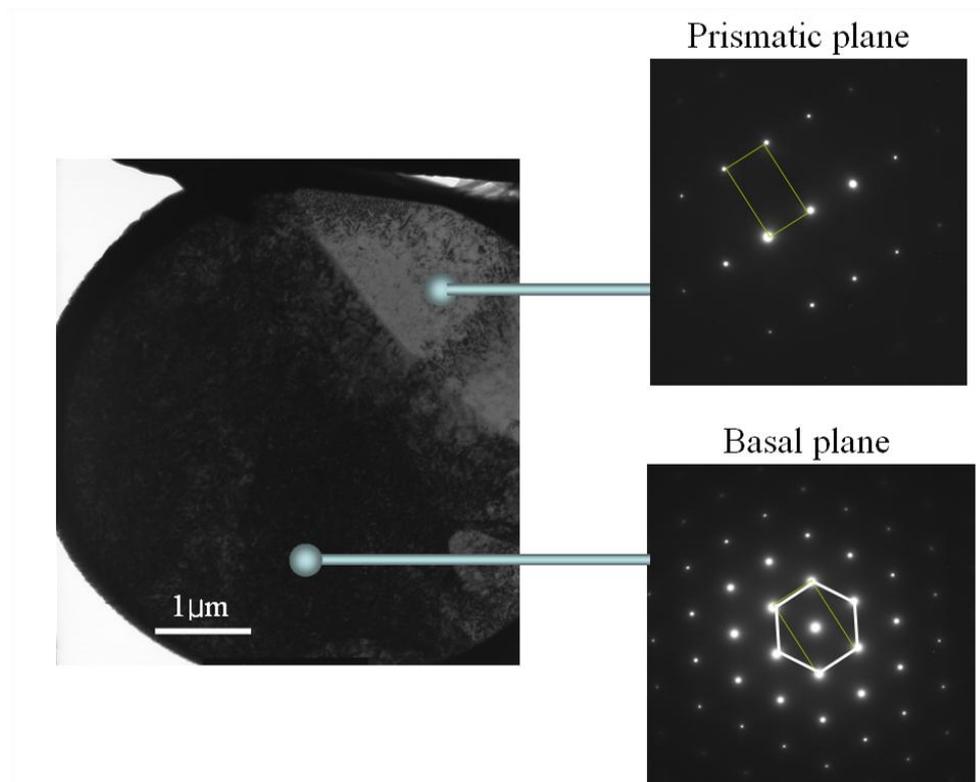
Figure 4.26: TEM micrograph and the two corresponding diffraction patters showing subgrains in the twinned region. Subgrains were not observed in the untwinned region.
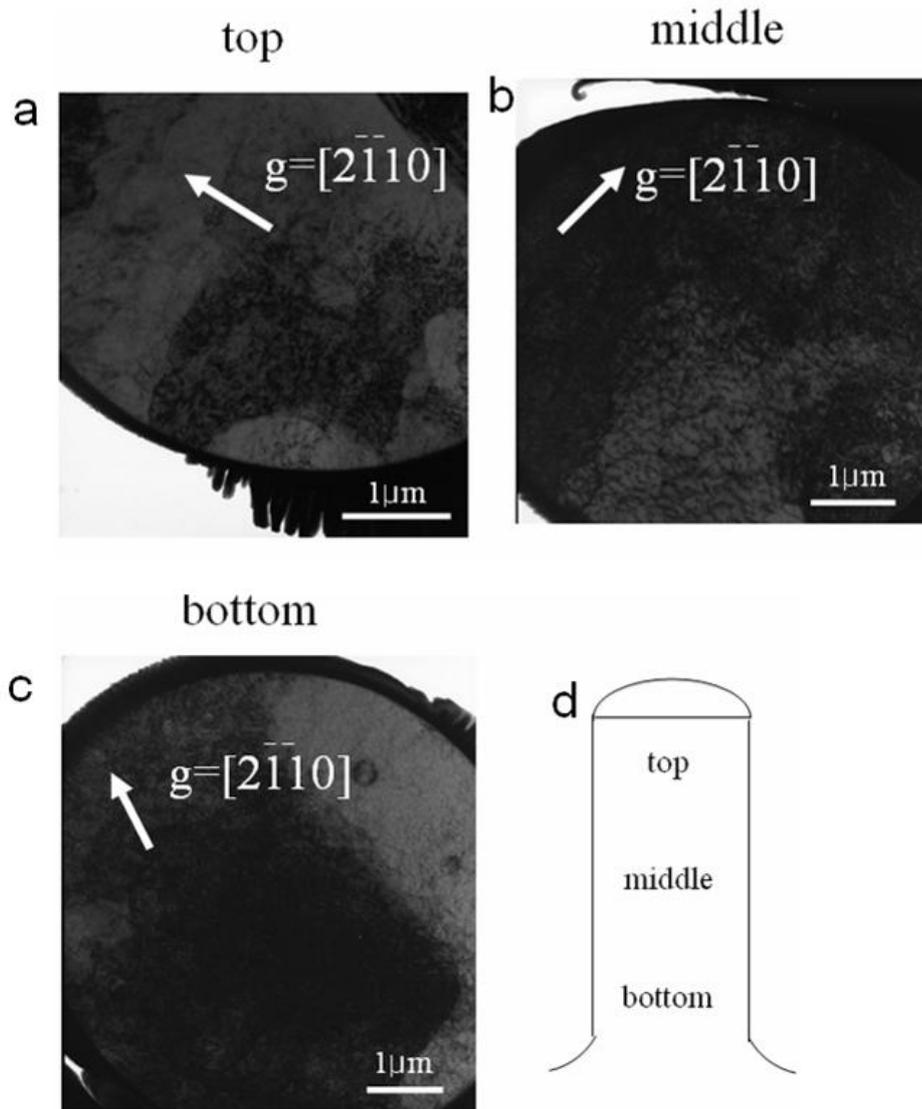
Figure 4.27: Size dependence of subgrain on the distance from the top of the column. With increasing distance from the top part of the column, the number of subgrains decreases and the size of the subgrains increases. The zone axis is [0001].

Figures 4.28(a) and (b) show the basal <a> dislocation on the plane where massive basal slip occurred for two columns deformed to a total strain of 5.5% and 10.8% deformed column, respectively. After massive basal slip, a distinct cell structure was observed, with lower dislocation densities observed within the subgrain interiors. The subgrains and the <c> component dislocations, which together form strong junctions, results in dislocation cell formation during the massive basal slip within the twin. In contrast, such a dislocation cell structure or subgrain structure was not observed on the basal plane in the case of [2-1-12] compression, indicating that the cell formation found in the [11-20] compression orientation is strongly dependent on twinning.
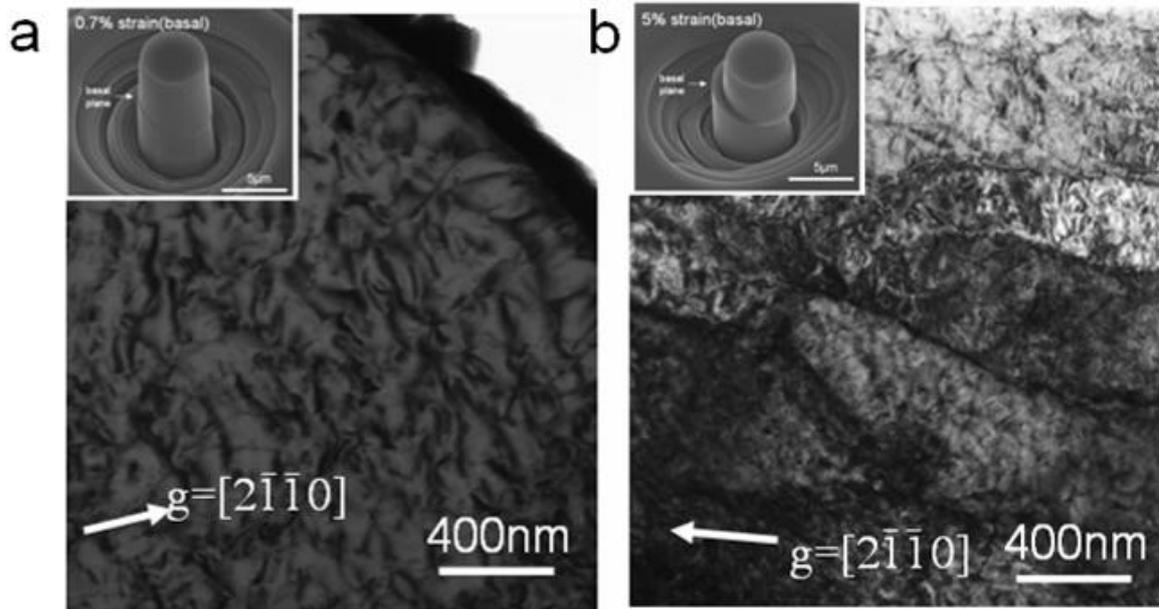
Figure 4.28: Dislocation cell formation on the plane where massive basal slip occurred, after a total strain of (a) 5.5% and (b) 10.8%.

4.4 [10-10] compression tests

We have compressed Mg single crystal along the [10-10] direction in order to compare the deformation behavior of the [11-20] orientation. Like the [11-20] orientation previously discussed, the [10-10] orientation is unfavorably oriented for basal slip. The Schmid factors are given in Table 2.4, and show that tensile twinning is a favorable deformation mode, as we found for [11-20]. In fact the symmetry of Mg that the expected deformation modes for the [10-10] should be very similar to those observed for the [11-20] orientation.

Figure 4.29 compares the stress-strain behavior of the [10-10] and [11-20] orientations, revealing very similar characteristics. In case of the [10-10] orientation, the maximum stress level was between 25MPa and 50MPa, and these values are lower than that of [11-20] compression. This difference is consistent with the difference in Schmid factors shown in Table 2.4 for the two orientations.
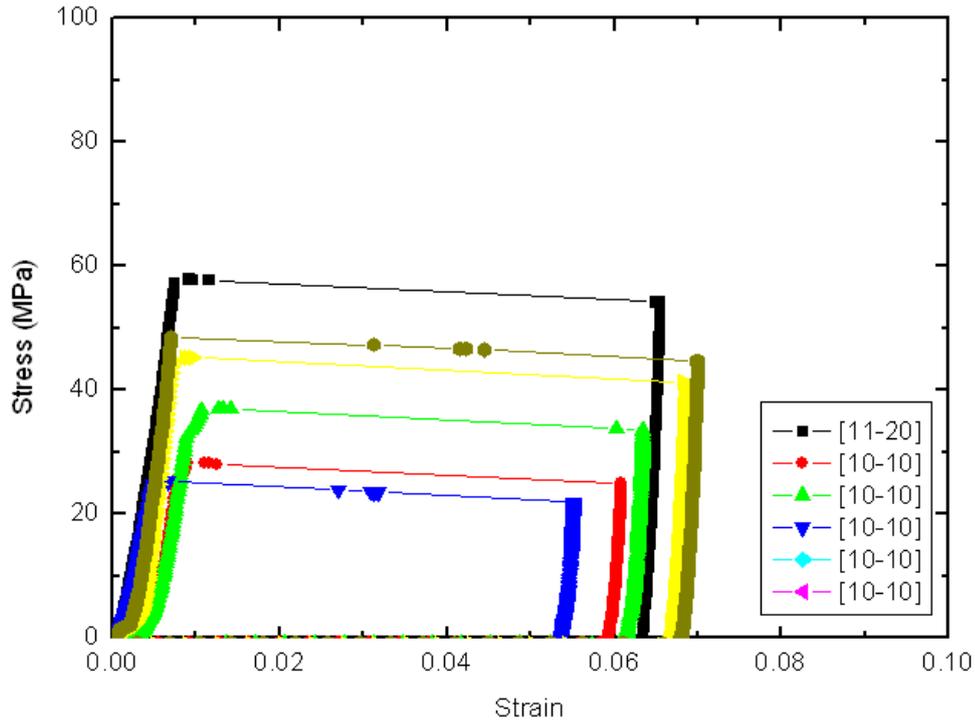
Figure 4.29: Stress-strain response of the [10-10] oriented columns, with one curve for the [11-20] orientation given in black for comparison.

In both crystal orientations, a tensile stress develops along the [0001] direction, and can lead to tensile twinning. The Schmid factor for the pyramidal $\pi3$ system (tensile twinning) of [10-10] and [11-20] is 0.5 and 0.37, respectively, revealing that the twining process is more readily activated in the [10-10] compression case. While twin nucleation is difficult to identify from the stress-strain data, the critical stress for the massive strain burst is lower for [10-10] compression axis.

An SEM micrograph of 5.5% deformed [10-10] orientation column is shown in Figure 30(a). EBSD observations of a cross sectioned column in Figure 30(b) confirms that tensile twinning occurred. Almost 80% of column has been twinned. Here again, the contribution of the twinning shear to the strain has been calculated by the equation 4.4. With whole column twinned, 0.065 of strain is achievable. This result is well agreement with the stress-stain behavior.

Figure 30(c) shows the crystallographic rotation of the column by twinning. After twinning, the compression direction changes from [10-10] to [1 0 -1 30], which has a misorientation of 2.9^{o} with [0001] direction. The new orientation is not favorable for basal slip, in contrast to the twin formed during [11-20] compression. Thus no massive basal slip occurred during the strain burst, as was observed in the case of the [11-20] orientation. Since the new compression direction of the twin is close to the [0001] axis, it might be expected that even higher stresses are required for the twin to deform, as were observed for the [0001] compression tests described previously. Unfortunately, we did not load beyond the post-strain

burst state to see if the twin followed the stress-strain path observed in the [0001] orientation case.
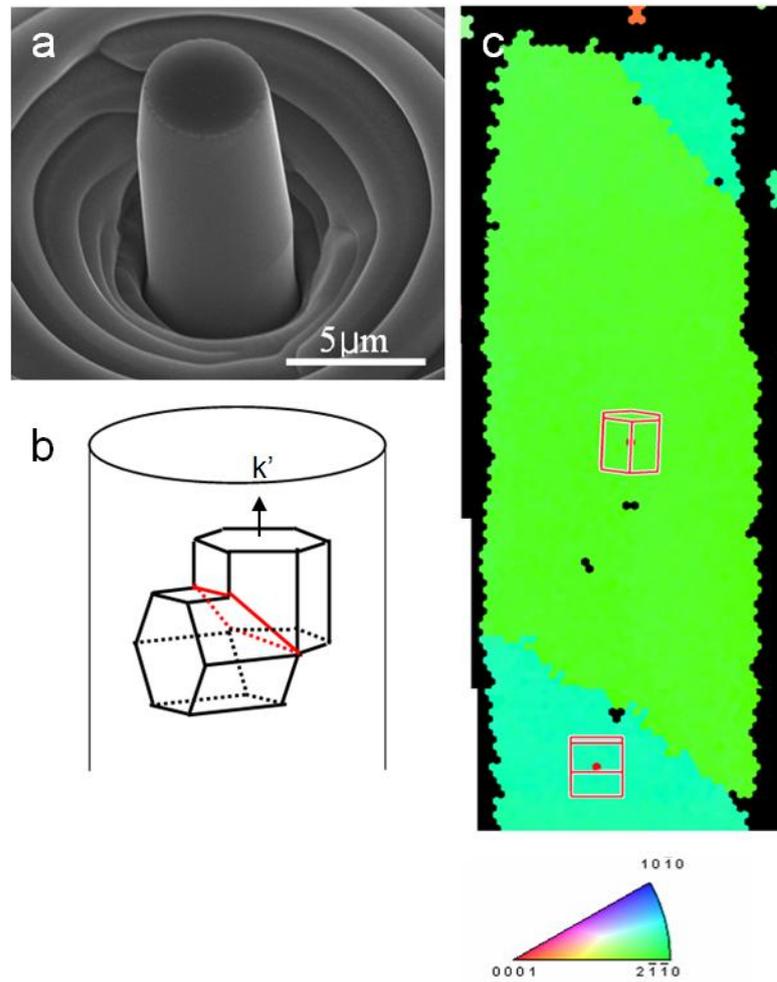
Figure 4.30: Deformation twinning of the [10-10] orientation pillar shown by (a) SEM image, (b) schematic of the twin and parent orientations, and (c) EBSD measurement.

Key points of Chapter 4

1. Slip and twinning behavior was analysed for the following orientation of the micro-pillar: [0001], [2-1-12], [10-11], [11-20] and [10-10]

2. Experimental tools used were microcompression test, SEM, EBSD and TEM.

3. The deformation behavior is strongly governed by the initial crystallographic orientation.

4. Strain burst was evidenced in all cases.

5. In the case of [0001] orientation, the stress increases linearly up to 2% of strain ($\sigma \approx 250$MPa) followed by a hardening and then a massive strain burst ($\sigma \approx 570$MPa). The basal slip system is not sufficient to accommodate the observed longitudinal strains. Hardening results from the activation and multiplication of <c+a> dislocations on the 6 equivalent pyramidal $\pi 2$ slip systems. Strain bursts are attributed to a massive basal slip.

6. In the case of [2-1-12] orientation and [10-10] orientations, the basal slip system is predominant since it feels the highest shear stress. Discrete slips bands oriented $45°$ to the loading axis are observed from exam in the SEM, and homogenously distributed <a> dislocations are observed on the basal plane from TEM investigations

7. In the case of [11-20] and [10-10] orientations, tensile twinning happens due to the tensile stress component along the <c> axis.

8. In the case of [11-20] the twining induced reorientation of the crystal trigger basal slip.

9. All the stress-strain curves show massive strain bursts occurring at 1% of strain.

10. Twinning shear on [11-20] orientation can accommodate the longitudinal strain up to 0.048. Thus, a part of the strain burst is associated to twin propagation. Massive basal slip follows the twinning.

11. In the case of [11-20] compression, <c> component dislocations have been trapped in twinned region. Non-basal <a> dislocation has been also observed in untwined region.

12. For [11-20] orientation, subgrains are observed in twinned region, but not in untwined region. The size of the subgrains increases with the distance from the top of the column. The rapid twin propagation may relate to the subgrain formation and growing.

13. In the case of [10-10] orientation, although massive strain burst happens, no squeezing

due to massive slip has been observed. Tensile twinning leads to a reorientation of the crystal unfavorable for basal slip. With a new loading axis of [10-130] after twinning, the compression stress required to activate basal slip is 10MPa. But the maximum stress measured on the stress-strain curve is 37MPa, 3.7 times larger than this critical stress.

14. In contrast, the [2-1-1-3] orientation which is twinned from the [11-20] orientation only requires 1.1MPa to activate basal slip. The stress measured on the stress-strain curve is 57MPa, 55 times larger than the required stress.

Experimental results and analyses: size effect

5.1 Historical review

During the last few decades, development and improvement of information technology has been required more intensive and comprehensive understanding of material at the small scale. For example, metals are commonly utilized at the sub-micron length scale in micro-electro-mechanical system (MEMS). The reliability of these devices is a critical issue necessitating new methods for characterizing the small volume plastic deformation.

Recently, Uchic *et al*. developed a methodology to investigate the small scale plasticity with the size of few microns ([Uchic *et al*. 04]). In this method, micro columns are fabricated employing focused ion beam FIB techniques, and are subsequently compressed using a flat punch in the nanoindenter, as described previously. Their results showed that the deformation behavior of the metal was strongly affected by the sample size. Specifically, the flow stress increased with decreasing sample size, demonstrating the so-called 'size effect'.

The continuum plasticity theory based on the Taylor hardening could not rationalize such size effect. The classical theory explains the increase of the flow stress by an increase of the dislocation density. In other words, if the dislocation density is increased in the material, more stress is needed for dislocation to overcome the dislocation forest. In the case of single crystalline Au, for example, it has been observed that stresses nearing 1 GPa have been observed. Such a stress requires a dislocation density of about 10^{16}m^{-2} which is associated with a dislocation spacing of 10nm ([Volkert and Lilleodden 06]). Such a high dislocation density is usually observed only in cases of a dislocation wall. In contrast, the micro pillars used in compression testing were single crystalline with free surfaces. Clearly, other mechanisms govern the flow strength in such small, finite volumes.

After the first development of the new microcompression methodology, the method has been used to study size effects by many researchers with different materials, e.g. Ni ([Dimiduk *et al*. 05], [Shan *et al*. 07]), Ni super alloy([Uchic and Dimiduk 05]), Mo ([Bei *et*

al. 07], [Greer *et al*. 08]), Au ([Greer e*t al*. 06], [Volkert and Lilleodden 06]), Cu ([Kiener *et al*. 09]) and Mg ([Lilleodden 10], [Byer *et al*. 10]).

In most of cases, the microcompression tests performed on metal show the strong size dependence in the flow stress and strain hardening.

Dimiduk *et al*. carried out the microcompression test on single slip oriented Ni micropillar with the size of 1~40μm ([Dimiduk *et al*. 05]). They observed that there appears a transition from 'bulk-like' behavior to 'multiplication-limited' behavior at the size of under 20μm.

Volkert and Lilleodden ([Volkert and Lilleodden 06]) performed microcompression tests on Au pillars with diameters in the range of 180nm to 8μm and observed a strong size effect on strain hardening as well as flow stress. They explained the size dependence with the 'dislocation source limited mechanism'. According to this theory, the dislocation density is decreased as the size is decreased because dislocations can be driven out the pillar due to the image stress. Therefore, more stress is needed to generate dislocation sources which can accommodate the deformation.

Greer *et al*. ([Greer *et al*. 06]) performed microcompression tests on Au and observed a size effect in the flow stress. They explained the size effect with the concept of dislocation starvation. According to the dislocation starvation theory, dislocations escape the pillar rather than multiply by the formation of the junction or cross slip as the compressive stress applied. Therefore, the required stress for the deformation is increased for new dislocation source generation. The dislocation starvation theory was supported experimentally by Shan *et al*. ([Shan *et al*. 07]). They carried out the *in-situ* compression tests in the TEM. They observed that the high density of dislocations in the sample was drastically decreased after the compression test for samples with diameters less than 160nm. The results indicate that the plastic behavior can be governed by dislocation starvation.

In contrast, Norfleet *et al*. showed that the dislocation density does not decrease after compression ([Norfleet *et al*. 08]). They performed microcompression tests and measured the dislocation density of undeformed samples as well as deformed samples with various column diameters. Interestingly, the dislocation density increased with decreasing size in both cases of undeformed and deformed pillars. According to the dislocation starvation theory, the dislocation density should decrease as deformation proceeds; the dislocation densities observed by Norfleet and coworkers indicate that dislocations multiply rather than escape the columns. They explained the observed size effect in terms of a 'weak-link source' mechanism. The main idea of this theory is that the weakest source, such as a single pinned dislocation located near the pillar surface or longer Frank-Read source, initially accommodates the deformation, and in turn the next weakest link source accommodates the deformation when the first one is exhausted.

Ng and Ngan used microcompression experiments on tungsten coated aluminum micropillar in order to investigate the effect of a hard layer on the size effect ([Ng and Ngan 09]). They observed that the dislocation density increased up to three orders of magnitude after deformation in the case of a coated pillar. The result reveals that the micropillar can be

strain-hardened and that the deformation can be highly confined by a surface layer.

Bei *et al.* conducted microcompression experiments on Mo micropillars which were fabricated using chemical etching, thereby circumventing the influence of FIB-induced effect ([Bei *et al.* 07]). In their research, no size effect in flow stress was observed and the deformation behavior was similar to the behavior of whiskers; the pillars all failed at a stress of about 9 GPa, a value near the expected theoretical stress. Their research was expanded to compare the two different methods of pillar fabrication, namely chemical etching and FIB milling ([Shim *et al.* 09]). The results show that the stress-strain behavior of a 670nm size of pillar prepared by FIB milling was similar to that of an 8% prestrained pillar fabricated by chemical etching. This means that the FIB milling process can induce defects on the pillar surface which can strongly influence the deformation characteristics.

Recently, the microcompression test was applied to hcp materials, where deformation twinning is known to be a relevant deformation mode. Byer *et al.* performed microcompression tests on (0001) oriented Mg, and concluded that no size effect was found ([Byer *et al.* 10]). In contrast, the microcompression test of (0001) Mg carried out by Lilleodden showed a size effect in flow stress, and no size effect in strain hardening ([Lilleodden 10]). It can be argued that the results from Byer in fact do show a size effect; the lack of sufficient experiments, and the offset in initial strain observed leave sufficient uncertainty in their conclusions. In both studies, no deformation twinning was observed, and pyramidal slip was considered to be the governing mechanism of plastic deformation for this orientation.

A microcompression study of size effects in twinning was first published by Yu *et al.* ([Yu *et al.* 10]). They performed microcompression tests on Ti alloy single crystal micropillars. They observed a strong size effect and a 'stimulated slip' model was suggested to explain the size effect.

In addition to experimental efforts, many computational studies have been carried out to understand size effects in plastic flow using FEM and dislocation dynamics ([Weygand *et al.* 08], [Guruprasad and Benzerga 08], [Tang *et al.* 07], [El-awady *et al.* 09]). The application of dislocation dynamics simulation to microcompression tests will be discussed in the next chapter.

Although the investigation of size effect is not the main subject of this thesis, we discuss the observed size effect in this chapter observations of size effects in pure, single crystalline Mg and their dependence on orientation are presented here. Single crystalline pillars with [0001], [2-1-12], [11-20] and [10-10] compression axes and with diameters of 1, 2, 5 and 10 µm were employed. In the case of the [0001] and [2-1-12] orientations, we investigated the size effect due to dislocation plasticity, whereas in the case of the [11-20] and [10-10] orientations we considered the size effect in twinning as well as dislocation plasticity.

5.2 Size effect due to dislocation plasticity

The stress-strain behavior of the [0001] orientation pillars with varying diameter is shown in Figure 5.1. All stress-strain curves show strain hardening and some of them show a massive strain burst depending on the extent of strain. It appears that the flow stress depends on the pillar size whereas the strain hardening is independent of size. Similar observations were published by Lilleodden([Lilleodden 10]). Another observation is the serration in the stress-strain curve. As the sample size is smaller, the serration gets larger. This is because the effect of one dislocation on the plastic strain is drastically increased at the small scale. In order words, only a few dislocations can introduce large strain if they escape the pillar.

Representative SEM images of deformed pillars of different sizes are shown in Figure 5.2. Each of them was deformed to about 6% strain. The apparent buckling or bending observed is not due to the misalignment of the flat punch tip or an inclination of the sample surface, since the direction of buckling is evenly distributed radially; as shown in Figure 5.3, when massive basal slip occurred it was distributed along one of the three of [11-20] directions with random frequency.

Figure 5.1: Size dependent stress-strain behavior of the [0001] orientation.
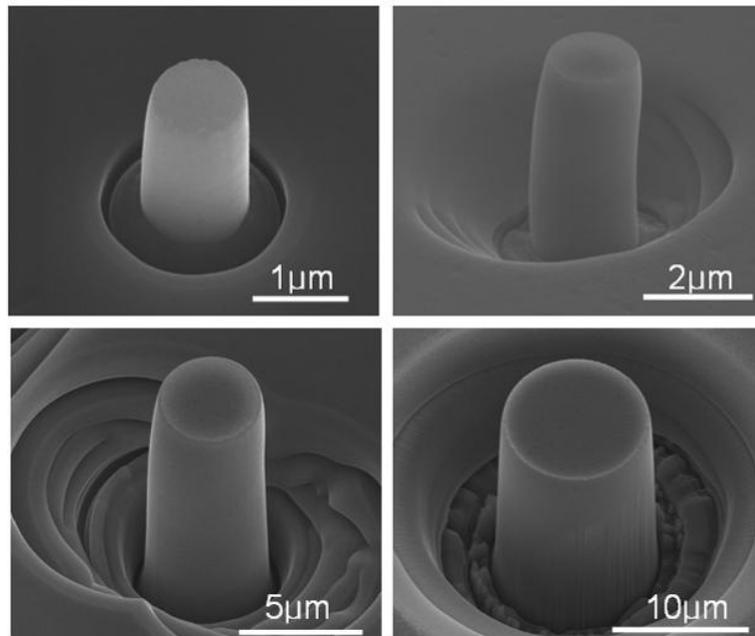
Figure 5.2: SEM images of deformed [0001] pillars of varying size.
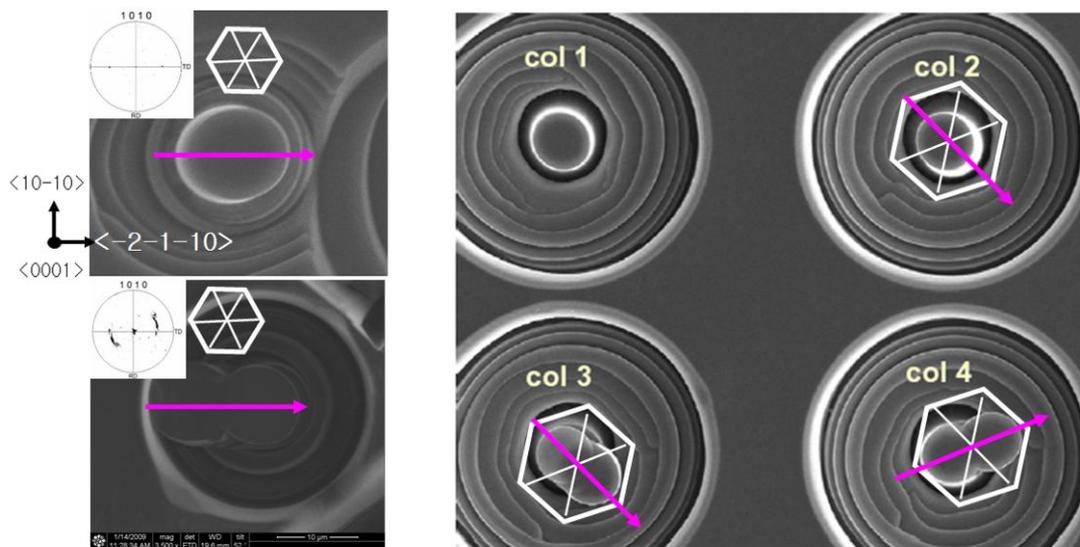
Figure 5.3: Massive shearing occurred along one of the three of <11-20> directions. The apparent buckling or bending observed is not due to the misalignment of the flat punch tip or an inclination of the sample surface, since the direction of buckling is evenly distributed radially.

Figure 5.4 shows the stress-strain behavior of the [2-1-12] orientation pillars. The flow stress of the 10μm size pillars was about 15MPa, which corresponds to 7.5MPa of shear stress. Such a stress level is consistent with the result of the compression tests performed by Kelly and Hosford ([Kelly and Hosford 68]). Strain hardening was not observed and no clearly defined strain burst was observed at the larger size. However, there was a clear and relatively strong size effect in flow stress observed for this orientation. Note that the flow stress of the 1μm pillars is at least 4 times greater than that of the 10μm pillars, whereas in the

case of [0001] compression the flow stress of the 1μm pillars is only about 1.5~2 times larger than that of the 10μm pillars.

In the case of the [2-1-12] orientation, we didn't observe any kind of barreling. This is because deformation is governed by the single slip system. Figure 5.5 shows that only basal slip plays an important role in the deformation of [2-1-12] compression.

In case of the [0001] compression orientation, basal <a> dislocations as well as <c+a> dislocations play an important role for the deformation. In contrast, in the case of the [2-1-12] compression orientation, only basal <a> dislocations play an important role. That is to say, multiple slip was observed in the [0001] orientation whereas only single slip is observed in [2-1-12] orientation. However, it is observed here that the size effect is substantially stronger in the [2-1-12] orientation. It seems reasonable that single slip would favor a stronger size effect, since the dislocation density increases and hardening occurs in the case of multiple slip. Furthermore, in the case of [0001] compression, the substantially higher Peierls stress of the activated pyramidal slip systems would favor a less strong size effect. This is because the correlation length governing dislocation interactions decreases with increasing Peierls barrier. However, according to the research of Volkert and Lilleodden, the flow stress and hardening rate are not strongly influenced by the number of activated slip systems in fcc metals. The differences between their study and that presented here for Mg may be related to the length scale investigated. If dislocation source starvation is governing the size effects at diameters less than 1 micron, as studied by Volkert and Lilleodden, it is possible that the active dislocations leave the crystal before they are able to interact with dislocations on intersecting slip systems. Thus there is no observed affect of multiple or single slip on the size effects observed for these small crystals. However, in the case of the Mg [0001] pillars in the size range of 1 to 10 μm studied here, we observe very strong hardening which demonstrates that strong dislocation-dislocation interactions are occurring.
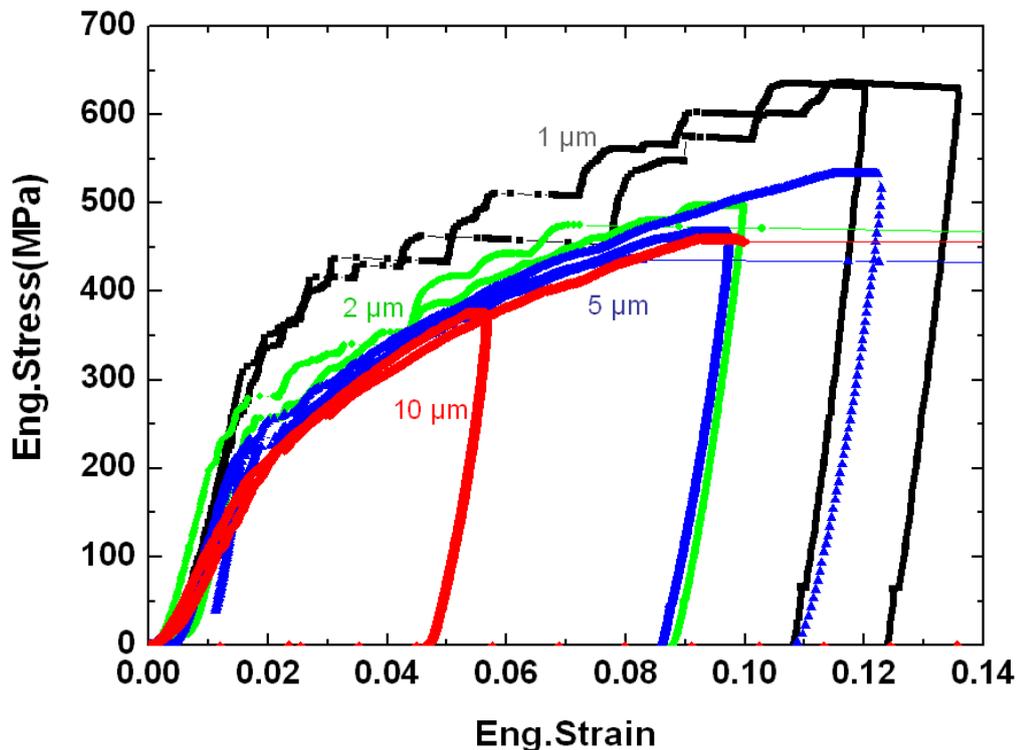
Figure 5.4: Size dependent stress-strain behavior of the [2-1-12] orientation.

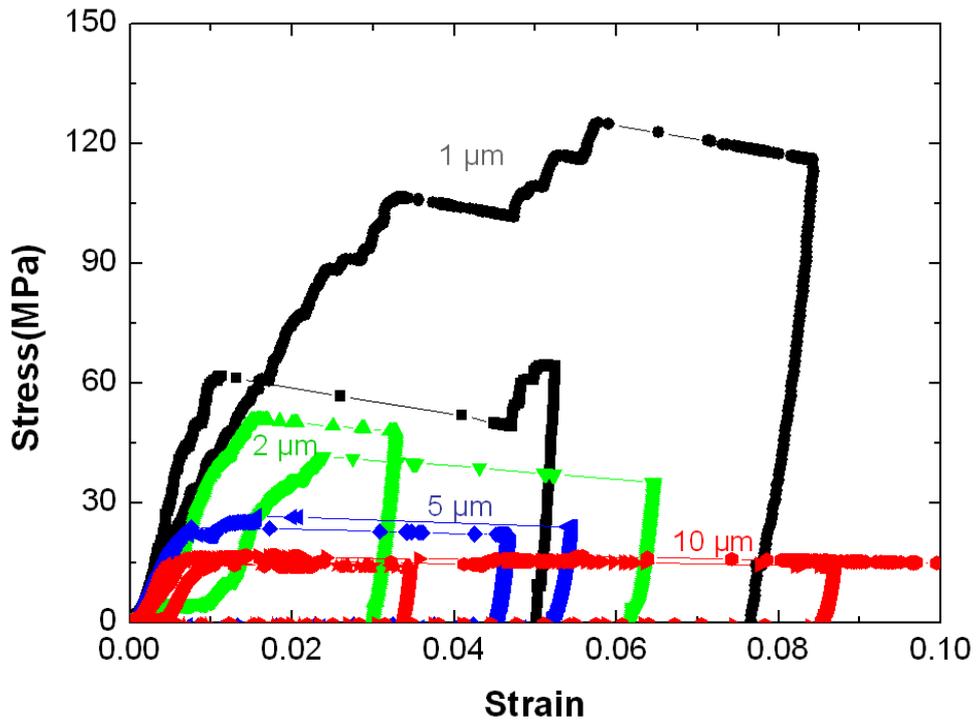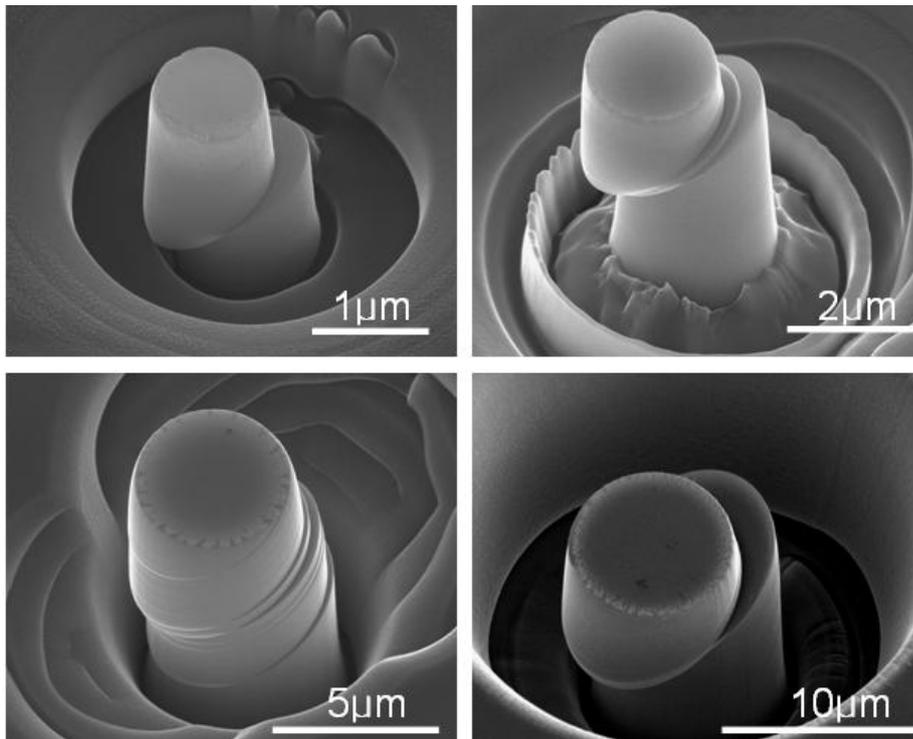**Figure 5.5**: SEM images of deformed [2-1-12] pillars of varying size.

5.3 Size effect of twinning affected orientation

The stress-strain response of uniaxial microcompression along the [11-20] axis is shown in Figure 5.6. The stress was increased largely linearly up to about 1% of strain, although the behavior is not purely elastic. Additionally, a few sharp nonlinearities during this initial loading are sometimes observed, likely due to twin nucleation and/or the onset of dislocation plasticity, as was discussed in Chapter 4. At about 1% strain a large strain burst is observed for all column sizes. As discussed in Chapter 4, the strain burst is due to rapid twin propagation as well as massive basal slip.

One interesting observation is that the amount of plastic strain after the burst increases with decreasing column size. This is likely due to the increased stress acting on the basal slip system with decreasing diameter, as dictated by the size effect. Such phenomenon was not observed in case of [10-10] orientation as shown in Figure 5.8, which does not show massive basal slip. Thus the size-dependent burst observed for the [11-20] orientation is attributed to the increase in basal slip activity with increasing stress. Figure 5.7 shows the SEM image of deformed [11-20] oriented pillars associated with varying size and plastic strain. As the size decreases, multiple massive slip bands were observed after strain burst.
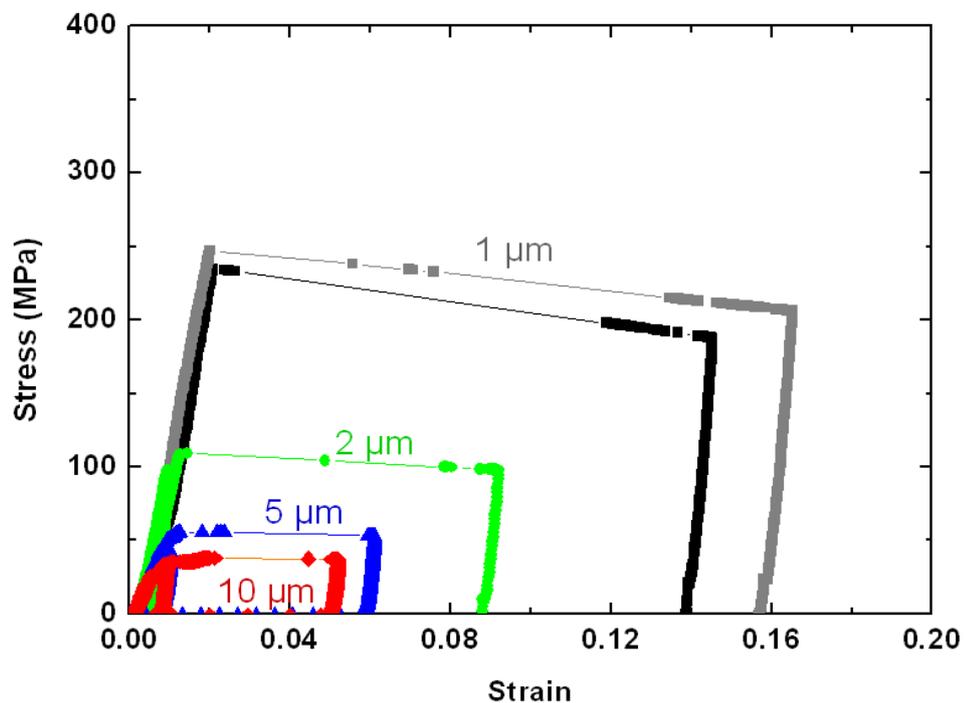
Figure 5.6: Stress-strain behavior of the [11-20] orientation pillars of varying size.
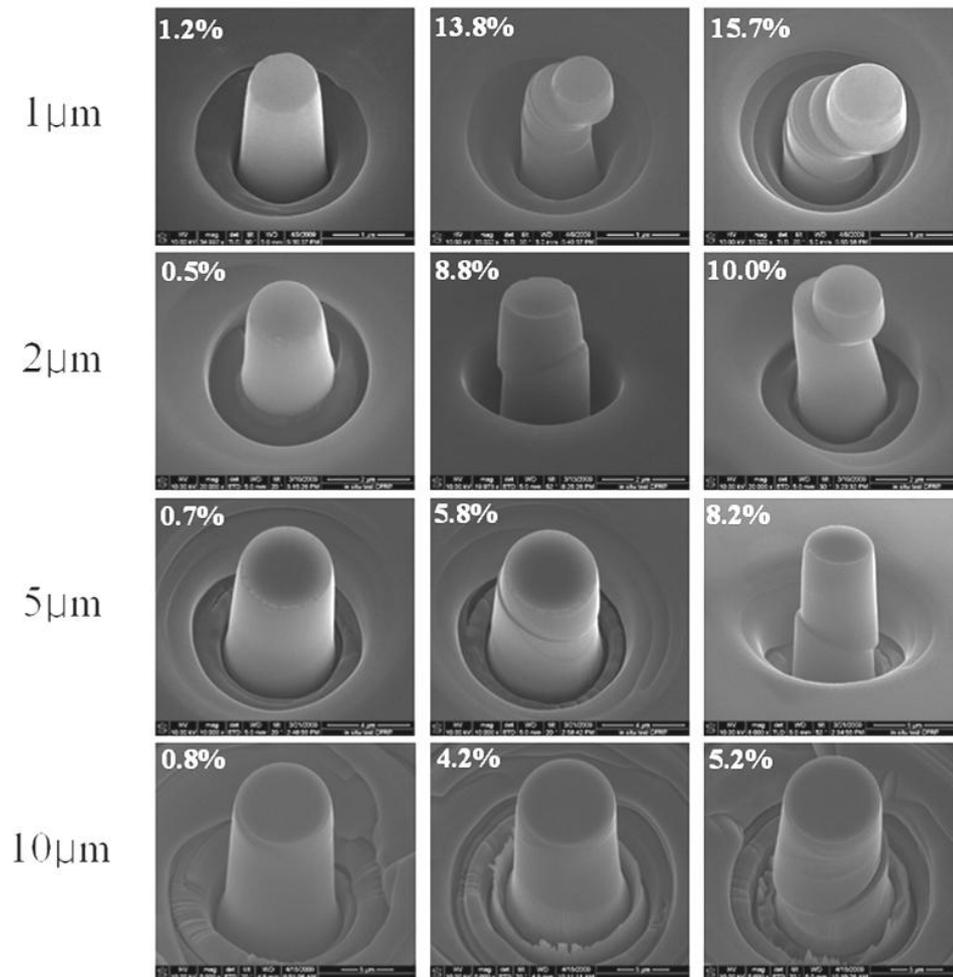
Figure 5.7: SEM images of deformed [11-20] oriented pillars with varying size and plastic strain. As the size decreases, multiple massive slip bands on the basal plane were observed after the strain burst.

Figure 5.8 shows the stress-strain response of the [10-10] orientation with varying size. Similar to the case of the [11-20] orientation, a size effect in flow stress was observed. Again, we observed strain bursts at round 1% of strain, but didn't observe any massive slip, as shown in Figure 5.9. In the case of the [10-10] orientation, such massive dislocation activity on a single slip plane is suppressed, as discussed in Chapter 4.3. The orientation of the twin is non-favorable for basal slip. The twin orientation is close to that of the [0001] compression pillars, which require a substantially higher stress to deform than is associated with the stress applied during the strain burst. Unfortunately these columns were not compressed further to see if they would follow a stress-strain path similar to the [0001] compression pillars, as we would expect.
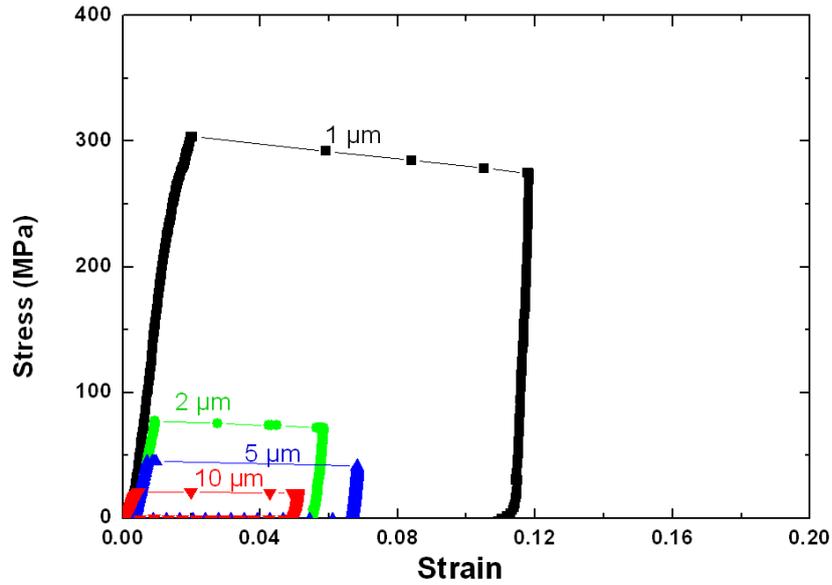
Figure 5.8: Stress-strain response of the [10-10] oriented pillars of varying size.
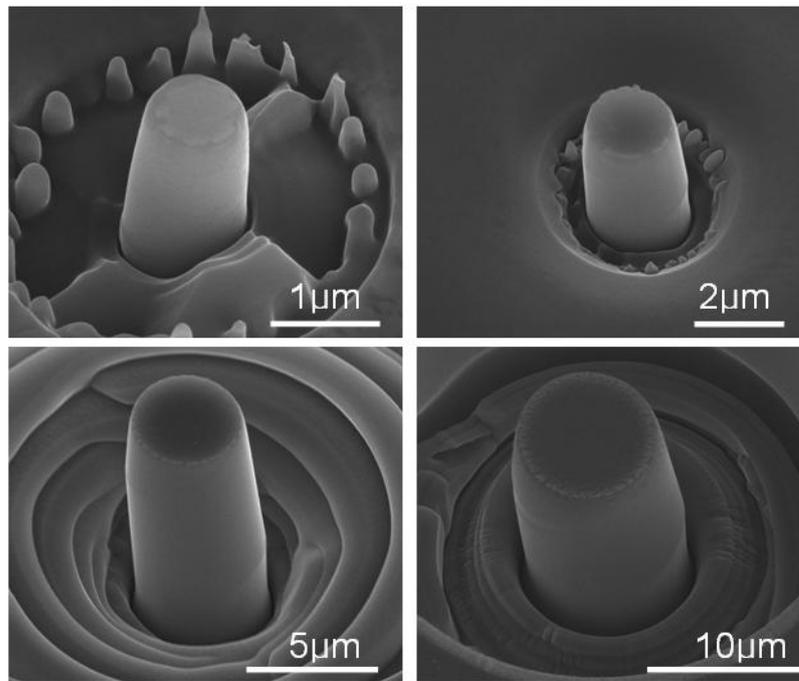
Figure 5.9: SEM images of deformed [10-10] oriented pillars of varying size and plastic strain.

Given the very similar size effect observed for both of the twinning orientations, namely [11-20] and [10-10], it is clear that the size effect must be influenced by the twin itself. In particular, we have shown in Chapter 4 that the size-dependent critical stress observed is associated with a transition from slow to rapid twin propagation. The size effect for the twinning orientations can be explained by considering both twinning and dislocation plasticity.

In a general sense, if twinning is mediated by the dislocation plasticity occurring concurrent with twin nucleation and propagation, one could rationalize the size effect in terms

of the same dislocation-based models already proposed for fcc metals. Such an explanation has been given by Yu *et al.* ([Yu *et al.*10])

The second rationale for the size effect is more directly related to twin propagation, based on the sub-structure observed in the case of the [11-20] orientation. It is already discussed that a strain burst occurs due to the rapid twin propagation. As shown in Figure 4.27 and discussed in Chapter 4.3, the size of the formed subgrain structure after the twin has propagated through the column was shown to increase with increasing position along the column: the finest subgrain structure was observed at the top of the column. It is thus possible that the sharp transition from slow to rapid twin propagation is dictated by the ability of the twin to propagate through the subgrain structure which pins the twin at the subgrain boundaries. As the sub-structure becomes coarser, the twin is less hindered. At the same time, the applied stress increases providing a larger driving force for twin propagation. At some optimum configuration the resistance to twin propagation is no longer greater than the stress driving twin propagation. The twin becomes unstable since further propagation becomes continually easier due to the ever coarser sub-grain structure.

A schematic comparison of the subgrain structure as a function of pillar size is given in Figure 5.10. In the case of the smallest pillar, the size of subgrain will still be small even at the bottom of the pillar. Therefore, more stress is required for twin propagation. Although this hypothesis should be proved by additional observations at different smaller or larger than 5μm column, and ideally through in situ experiments, the observed gradient in the subgrain size provides an alternate explanation of twin involved size effects than those previously given.
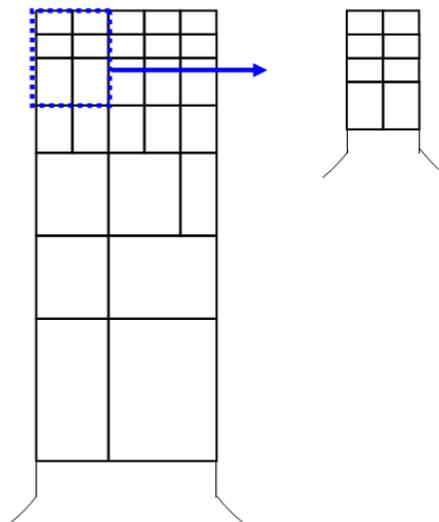
Figure 5.10: Schematic image showing the gradient in the size of the subgrain structure for a relatively large and relatively small pillar. It can be seen that the absolute size of the subgrain structure at the mid-height position in the small pillar is smaller than that for the large pillar.
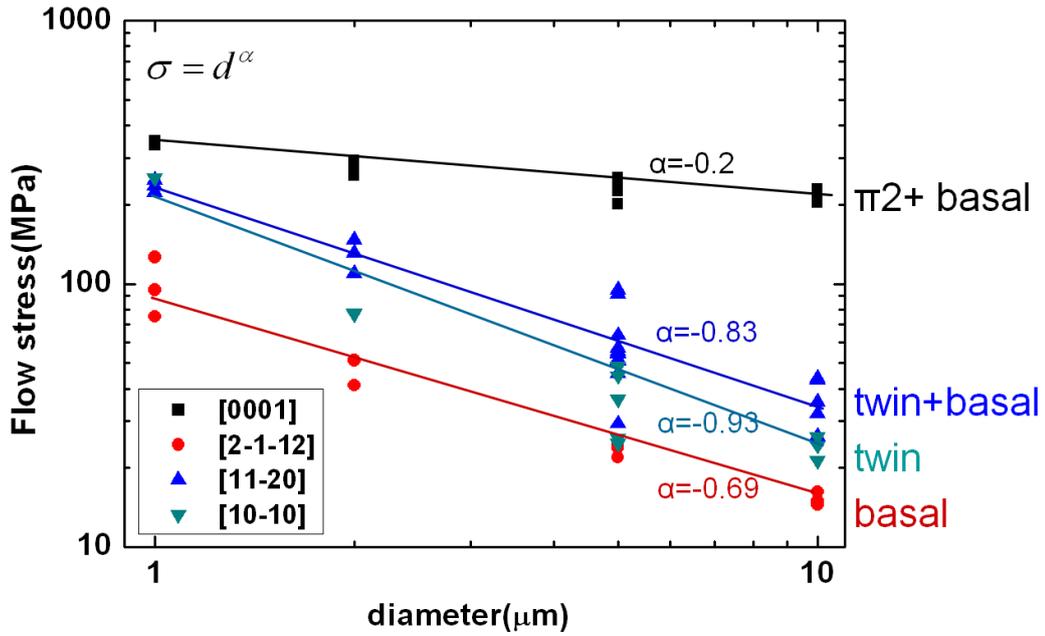
Figure 5.11: Flow stress versus diameter on a log-log plot of the [0001], [2-1-12], [11-20], [10-10] orientated pillars, with best fit scaling exponent given per orientation.

Figure 5.11 shows the flow stress versus pillar diameter for all orientations. The best-fit exponent for each orientation is also given in order to investigate how the size effect is dependent on deformation mode. In the case of the [0001] and [2-1-12] orientations, the stress at 2% of strain is chosen. This is because the strain hardening starts at round 2% of strain in the case of [0001] orientation, and an earlier yield stress is difficult to identify due to inherent small scale plasticity and issues arising from initial contact. In the case of the [11-20] and [10-10] orientations, the stress at 1% of strain was chosen as this is associated with the critical point which is most obviously assessed from the data. It is acknowledged that this is not the stress at which either plasticity or twinning is initiated, but serves as an identifiable parameter for comparison across varying size.

At first, let us consider the case where deformation is limited to dislocation plasticity. In the case of the [0001] orientation, for which pyramidal slip dominates the deformation prior to the critical point, an exponent of -0.2 is found and this orientation exhibits the weakest size dependence. In contrast, the [2-1-12] orientation which deformed mainly by basal slip shows and exponent of -0.69 and a relatively strong size dependence. A similar exponent of -0.61 is reported by Volkert and Lilleodden ([Volkert and Lilleodden 06]) from experiments on Au and a value of -0.69 reported by El-awady *et al.* ([El-awady *et al.* 09]) from dislocation dynamics simulations on Ni.

On the other hand, the two twinning dominated orientations showed the strongest size dependence. An exponent of -0.83 was found for the [11-20] orientation was and a value of -0.93 was found for the [10-10] orientation. Although the twinning activity observed in these two orientations is also affected by dislocation plasticity, it seems reasonable that the relatively high exponents found relative to the dislocation dominated orientations is due to the

twinning mechanism. Such a tendency was also observed by Yu *et al.*, as shown in Figure 5.12. They observed that the size dependence in strength is more severe when the Ti alloy is deformed by deformation twinning rather than dislocation plasticity.
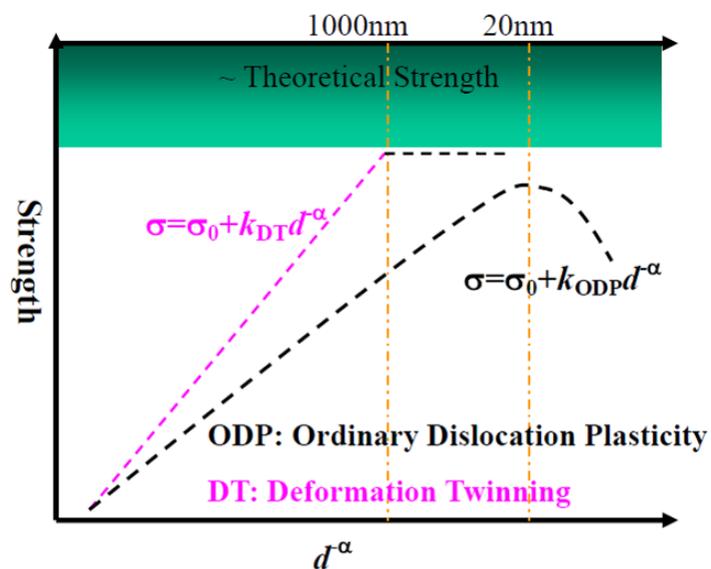
Figure 5.12: "Comparison of Hall-Petch scaling and Hall-Petch breakdown between ordinary dislocation plasticity (ODP, black curve) and deformation twinning (DT, magenta curve). Deformation twinning is much more size aware than ordinary dislocation plasticity in bcc and hcp metals." ([Yu *et al.* 10])

Key points of Chapter 5

1. Size effect is discussed for 4 orientations ([0001], [2-1-12], [11-20], [10-10]). In all cases, a size effect in flow stress is observed

2. The flow stress was plotted as the function of diameter and the scaling exponent was fitted. The magnitude of the exponent associated with the twinning dominated orientations was found to be larger than the dislocation dominated orientations indicating a stronger size dependence.

3. To explain the size effect due to dislocation plasticity, a brief review of research was summarized. It is observed here that the size effect is substantially stronger in the [2-1-12] orientation than in the [0001] orientation. The single slip would favor a stronger size effect, since the dislocation density increases and hardening occurs in the case of multiple slip

4. The size effect observed in the twinning dominated orientations was discussed in terms of both dislocation and twinning effects. Since dislocation plasticity occurs alongside twinning, it is possible that the same rationales given for size effects in dislocation plasticity hold for these orientations. A second explanation given described the size effect in terms of the gradient in subgrain structure size observed which can influence the transition from slow to rapid twin propagation.

Part II.

3D Discrete Dislocation Dynamics

Principles of dislocation dynamics

6.1 Historical background of DDD

The 3 dimensional discrete dislocation dynamics (3D DDD or DD) simulation was firstly imagined by the author of [Canova and Kubin 91] in order to predict and analyze the collective motion of dislocations. In this modeling, a dislocation line is discretized in a set of pure edge and screw dislocation segments. For each segment, the dislocation mobility is derived from the effective stress evaluated at its center as the superposition of the internal stress induced by the entire set of dislocation and the applied external stress. Each of the segments can then glide or multiply in the simulation box according to local rules describing the local reactions that may occur during the flight such as annihilation, junction or cross slip. This type of modeling is now referred as the *edge-screw model* and the code TRIDIS used in this work belongs to this category. Through the years, the code TRIDIS has been continuously improved both in terms of capabilities ([Fivel *et al*. 96]) and computer efficiency ([Verdier *et al.* 98], [Shin *et al.* 06]).

More recently, a new generation of DD codes has been developed: *the nodal model*. The dislocation lines are now represented by sets of nodes connected by segments with any possible orientation. The first 3D nodal code was proposed by Kukta ([Kukta 98], [Shenoy *et al.* 00]). It relies on a finite element description of the system in which the set of unknown corresponds to the node velocities. The same formalism has been widely used in all the more recent codes such as the one developed in Europe ([Weygand *et al*. 01]), [Numodis] or in the USA ([Schwarz 99] [Zbib *et al. 99*], [Ghoniem and Sun 99], [Arsenlis *et al.* 07]).

The nodal codes are based on a better description of the dislocation lines leading to a more accurate description of dislocation plasticity. On the other hand, the edge-screw models are more efficient in terms of computer calculations so that they can handle relatively larger dislocation densities.

Although different, all the DD codes rely on a similar algorithm. A computation step can be decomposed into the following 4 steps;

i) Discretization of the dislocation lines into segments or nodes
ii) Computation of the effective stress on each dislocation segment.

iii) Determination of the dislocation velocity using the mobility function.

iv) Updating the dislocation position.

Due to the efforts of many researchers within the last few decades, DDD has been applied to study the plasticity in various fields. In the case of fcc materials, one could quote the studies of nanoindentation in copper single crystals ([Fivel *et al.* 98], [Chang *et al.* 07]), the fatigue behavior of 316L stainless steel ([Déprés 04]), the fatigue of precipitate hardened materials ([Shin *et al.* 07], [Shin 04]), fatigue of copper via ([Kim GS *et al.* 10]), microcompression test ([Weygand *et al.* 08], [Tang *et al.* 07], [Greer 08]. [El-awardy *et al.* 08]) and micro-bending test ([Motz *et al.* 09]). For bcc materials, DD was used to investigate crack propagations ([Devincre and Robert 96]), plastic behavior of Molybdenum ([Tang *et al.* 98]), dislocation activity in Fe ([Chaussidon *et al.* 08]).

Very few simulations were performed in hcp materials, mainly because of the complex topology of the slip systems and the difficulty to measure the dislocation mobility in the various glide systems. Recently, dislocation glide in prismatic slip systems of Zr was studied in [Monnet *et al.* 04]. Creep simulations of ice single crystal was also investigated by Chevy who used code TRIDIS ([Chevy 08]).

To summarize, up to now, DD simulations have been widely used to investigate crystal plasticity in confined volumes and mainly in fcc crystals. Although the amount of cumulated plasticity is limited to a few percents of plastic deformation because of computational constraints, DD gives insights of the physics underlying the early stage of crystal plasticity.

The DD simulations presented in this thesis were all performed using the edge-screw model TRIDIS developed in Grenoble, France. Version 9.1 was used. This version was devoted to fcc crystals and outlines of the code are given in the next section (6.2). The modifications done in order to shift to the hcp Mg will be detailed in section 6.3.

6.2 The edge-screw code TRIDIS

6.2.1 Edge-screw model

In edge-screw models, a dislocation line is represented by a combination of pure edge and screw dislocation segments. A typical example is shown in Figure 6.1. Assuming that the black dot line is the actual dislocation line, the discretization into edge and screw segments leads to the blue solid line. As depicted in the Figure, each dislocation segment starts and ends on a particular points corresponding to a physical position of an atom of the crystal lattice.
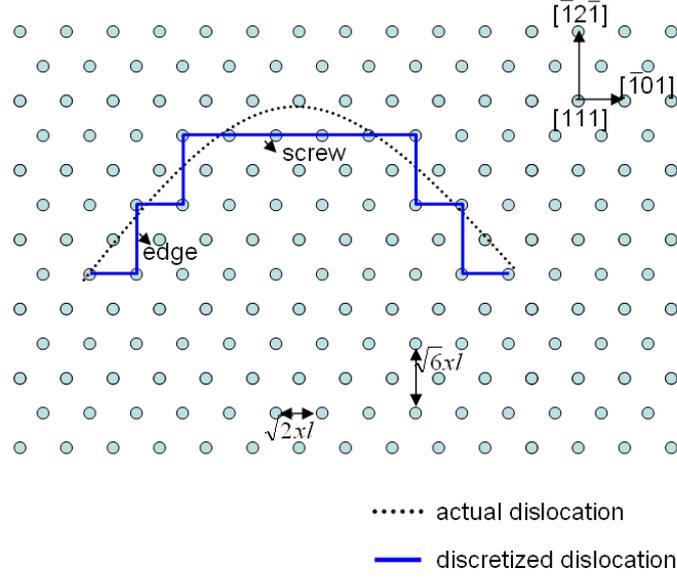
Figure 6.1: Edge-screw discretization of a dislocation line located in the (111) slip plane in TRIDIS code. The simulation lattice is defined by distance of '*xl*'. The out of plane direction is [111].

As opposed to atomic simulations, the minimum distance between two points of the simulation lattice (parameter *xl*) is much bigger than the lattice parameter a. Typically, the simulation lattice, *xl,* usually retained for fcc simulations is set to 10 times the Burgers vector magnitude: *xl*=10*b*. Note that this size is not a fixed parameter. It has been reduced down to *xl*=0.1*b* by Nogaret when he looked at dislocation-Frank loop interactions in irradiated stainless steels ([Nogaret 07]). At a larger scale, Kim used xl=b to model dislocation activity in copper via of a few hundreds of nanometer ([Kim GS *et al.* 10]).

In this thesis, *xl* was fixed to *xl*=10*b*. Since two dislocations cannot co-exist at a distance smaller than *xl*, this means that we will not be able to account for partial dislocations and rather restrict our study to the case of perfect dislocations.

6.2.2 Effective stress calculation

In order to calculate the dislocation mobility, the effective resolved shear stress τ^{eff} is estimated for each dislocation segment using equations 6.1-3.

$$\tau^{**}b = \left\{ \left| \left(\overline{\overline{\sigma}}^{app} + \overline{\overline{\sigma}}^{int} \right) \cdot \overline{b} \right| \times \overline{l} \right\} \cdot \overline{g} \qquad (6.1)$$

$$\tau^{*} = \tau^{**} + \tau^{lt} \qquad (6.2)$$

$$\tau^{eff} = \tau^{*} - sign(\tau^{*}) \cdot \tau^{peierls} \qquad (6.3)$$

,where $\overline{\sigma}^{app}$ is the applied stress tensor, $\overline{\sigma}^{int}$ the internal stress tensor induced by the other dislocation segments, $\overline{b}$ the Burgers vector, $\overline{l}$ the unit line vector of the dislocation segment, $\overline{g}$ the segment's gliding direction, τ^{lt} the line tension correction needed to account for the self stress and $\tau^{peierls}$ the Peierls stress under which the dislocation cannot move.

After the summation of the internal stress and the externally applied stress of all segments, the stress on the slip system is computed by Peach-Koehler equation as shown in equation 6.1, then, the line tension which depends on the local curvature of the dislocation line is added (equation 6.2). Finally, the effective resolved shear stress is obtained after the consideration of the Peierls stress.

6.2.3 Dislocation mobility

Assuming a simple viscous glide, the dislocation velocity v is derived from the effective stress as:

$$v = \frac{\tau^{eff} \cdot b}{B} \quad (6.4)$$

,where B is the viscous drag coefficient and b the Burgers vector magnitude.

For each time step, the dislocation velocity is calculated for each dislocation segment. Each segment is then translated along the glide distance $dx = v \cdot dt$. Therefore, the value given to the time step dt is an important parameter in DD simulations. Coming back to the discussion in section 6.2.2, smaller time step is needed when a smaller distance xl is selected.

6.2.4 Dislocation multiplication

The easiest way to increase the dislocation density consists to introduce a set of dislocation sources in the simulation box. Each source is made of a segment pinned at both ends. Then, when the effective stress is high enough, the dislocation will bow out and act as a Frank-Read source, emitting successive closed dislocation loops.

The total dislocation length can also increase by the generation of new dislocation sources as in the case of dislocation interactions (junctions) or when dislocation cross slip. Classically, in DD simulations, cross-slip events have been introduced as a local rule applied to screw dislocations. The cross-slip probability is given by equation 6.5

$$P = \beta \frac{l}{l_0} \frac{\delta t}{t_0} \exp\left(\frac{\tau_d - \tau_{III}}{kT} V_{act} \right) \qquad (6.5)$$

,where β is a normalization coefficient, l is the length of the considered screw segment, l_0 is 1μm, t_0 is 1 second, τ_d is the resolved shear stress in the deviate slip system, τ_{III} is the threshold stress, k is the Boltzmann coefficient, K is the temperature and V_{act} is the activation volume. A random number p is generated by the computer and the cross slip event is permitted only if the random number is lower than the probability P. In the case of copper, typical value of τ_{III} and V_{act} is 32MPa and 350eV, respectively.

It is known that cross slip strongly relates to the stacking fault energy: the higher the stacking fault, the higher the cross-slip probability. The stacking fault energy of copper, aluminum is $40mJm^{-2}$, $140mJm^{-2}$, respectively. In the case of magnesium, the value of $36{\sim}50mJm^{-2}$ were reported in many research, as shown in Table 2.2. Therefore, it may be reasonable to use the same values of τ_{III} and V_{act} in copper and magnesium.

6.2.5 Definition of virtual segments

When the simulated volume contains at least one free surface, dislocations may cross the surface and enter a so-called '*virtual space*' where their stress field is cancelled. These virtual segments do not interact with the real segments located within the sample. They are however stored in memory in order to keep track of the dislocation line connectivity so that it will be possible to compute the deformed shape of the surface as a post-treatment: the free surface is meshed into a set of points at which the dislocation displacement field is computed.

Full details of TRIDIS are described in [Verdier *et al*. 98] and [Shin 04]. Any readers who want to study TRIDIS or basic background story of the DD may read the above article and thesis (published in English).

6.3 Adaptation of TRIDIS to hcp

6.3.1 Simulation lattice

The first conversion of TRIDIS to hcp structure has been attempted by J. Chevy ([Chevy 08]). Using TRIDIS, she studied the creep behavior of ice single crystals by performing torsion test at a bulk scale (typically within a cylindrical box of 1mm diameter). In this study, the adaptation to the hcp crystallography was restricted to basal and prismatic slip systems.

In this work, pyramidal slip systems had to be considered in order to simulate the

uniaxial compression test as described in the preceding chapter. Thus, we introduced 4 different slip systems: basal, prismatic, pyramidal π1 and π2. Figure 6.2 shows how the vector transformation was performed from fcc to hcp. Figure 6.2(a) shows the 3 different Burgers vectors on the [111] plane of the fcc structure. Similarly, Figure 6.2(b) shows the 3 different Burgers vector on the basal plane and the c-axis. The [0001] direction in hcp can correspond to the [111] vector in fcc, and the 3 different Burgers vector of the basal plane ([2-1-10], [-12-10], [11-20]) in hcp can be replaced by the fcc vectors ([-101], [1-10], [01-1]), respectively. Using this trick, basal and prismatic slip systems are simply converted. This was precisely the method used by Chevy.

In contrast, the conversion of pyramidal slip systems is more complicated if we want to keep the fcc crystallography for the simulation lattice (Figure 6.3(c)). For example, the expression of <c+a> (<11-23>) dislocation in TRIDIS can be calculated by the summation of vectors. During the calculation, any kind of <a> vector was divided by its magnitude to make it unit vector, whereas <c> vector which is presented as [111] is used without any normalization. As a result, <c+a> dislocation was expressed as equation 6.6:

$$< c + a >=< 0001 > + \frac{1}{3} < 11\bar{2}0 > \xrightarrow{conversion} [111] + \frac{1}{\sqrt{2}} [0\bar{1}1] \qquad (6.6)$$

Note that this gives a ratio c/a=1.732. The c/a ratio of actual Mg is 1.624. Such a mismatch of c/a ratio is inherent to the fcc discretization and this issue will be dealt in Chapter 6.3.3.
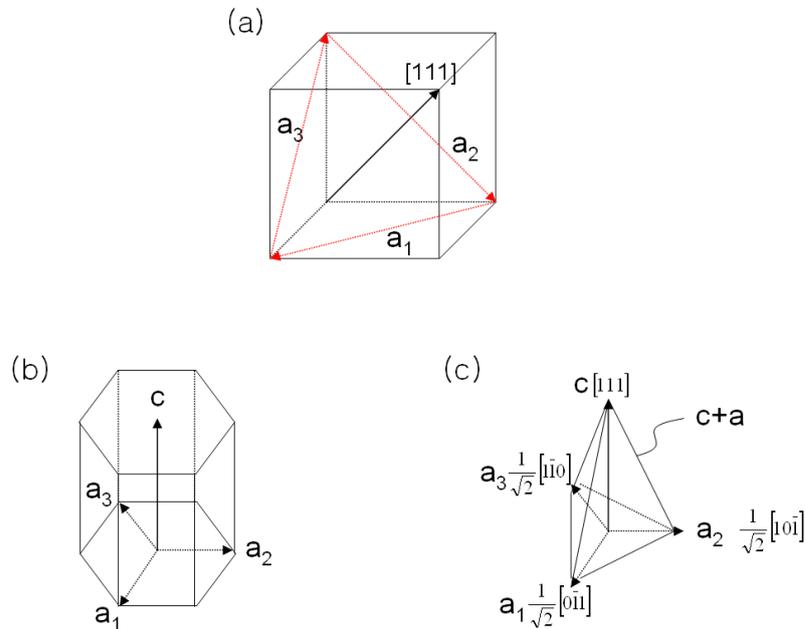
Figure 6.2: Conversion of TRIDIS-fcc to the hcp structure: (a) Burgers vectors in fcc structure (b) Burgers vectors in hcp structure (c) conversion of Burgers vectors

6.3.2 Slip system and line directions

As discussed in Chapter 2.2.1, it is known that magnesium has at least 4 different slip systems; basal, prismatic, pyramidal $\pi1$, pyramidal $\pi2$. Although other slip system such as <c+a> dislocation on pyramidal $\pi1$ slip plane has been reported, we only considered here the four most frequently observed or used slip systems. Table 6.2 lists the line vectors retained for the edge and screw line directions as well as the plane normal of 4 different slip systems, again expressed in the fcc lattice. According to the conversion rule discussed in Chapter 6.3.1, the vectors can all been calculated. The slip system number 1, 3 and 5 are the basal slip system, 2,4 and 6 are the prismatic slip system, 7 ~ 18 are the pyramidal $\pi2$ slip system and 19 ~ 24 are the pyramidal $\pi1$ slip system. In the case of pyramidal $\pi2$ slip system, each vector was used twice, for example, system numbers 7 and 8 have the same dislocation vectors i.e. they define the same slip system. This was introduced in order to account for cross-slip in the same manner for every slip system. In Table 6.2 the systems are arranged so that two consecutive slip systems share a common Burgers vector. In the case of pyramidal $\pi2$ slip system, the cross-slip was not accounted for in this simulation. Thus, the deviate system was imposed equal to the primary one.

System	1	2	3	4	5	6
Screw	[$\bar{1}$01]		[1$\bar{1}$0]		[0$\bar{1}$1]	
Edge	[$\bar{1}$2$\bar{1}$]	[111]	[$\bar{1}$12]	[111]	[$\bar{2}$11]	[111]
Plane normal	(111)	(1$\bar{2}$1)	(111)	(11$\bar{2}$)	(111)	($\bar{2}$11)

System	7	8	9	10	11	12
Screw	[3 17 10]		[3 10 17]		[10 3 17]	
Edge	[11$\bar{2}$]	[11$\bar{2}$]	[$\bar{1}$2$\bar{1}$]	[$\bar{1}$2$\bar{1}$]	[$\bar{2}$11]	[$\bar{2}$11]
Plane normal	(22 $\bar{8}$ 7)	(22 $\bar{8}$ 7)	(22 $\bar{7}$ $\bar{8}$)	(22 $\bar{7}$ $\bar{8}$)	(7 22 $\bar{8}$)	(7 22 $\bar{8}$)

System	13	14	15	16	17	18
Screw	[17 3 10]		[17 10 3]		[10 17 3]	
Edge	[$\bar{1}$$\bar{1}$2]	[$\bar{1}$$\bar{1}$2]	[12$\bar{1}$]	[12$\bar{1}$]	[21$\bar{1}$]	[21$\bar{1}$]
Plane normal	($\bar{8}$ 22 7)	($\bar{8}$ 22 7)	($\bar{8}$ 7 22)	($\bar{8}$ 7 22)	(7 $\bar{8}$ 22)	(7 $\bar{8}$ 22)

System	19	20	21	22	23	24
Screw	[$\bar{1}$01]		[1$\bar{1}$0]		[0$\bar{1}$1]	
Edge	[13 34 13]	[$\bar{2}$7 $\bar{6}$ $\bar{2}$7]	[27 27 6]	[13 13 34]	[6 27 27]	[34 13 13]
Plane normal	(17 $\bar{1}$3 17)	($\bar{1}$ 9 1)	(1 1 $\bar{9}$)	(17 17 $\bar{1}$3)	(9 $\bar{1}$ $\bar{1}$)	(13 $\bar{1}$7 $\bar{1}$7)

Table 6.1: Definition of the slip systems used in the hcp simulations. Systems number 1, 3 and 5 are the basal; 2, 4, and 6 are the prismatic slip system; 7 ~ 18 are the pyramidal $\pi2$ slip system and 19 ~ 24 are the pyramidal $\pi1$ slip system.

6.3.3 Schmid factor estimations

As we mentioned above, TRIDIS for hcp is developed based on the fcc code. The distance from origin to [111] point in fcc is $\sqrt{3}$ (≈ 1.732) whereas, in Mg, the distance along [0001] is 1.624. This inaccuracy in the system coordinates induces some artifacts in the Schmid factors for the hcp crystallography. Table 6.3 gives the Schmid factor computed on each slip systems for different directions of the uniaxial applied stress. The Schmid factors of actual Mg are also reported. Values are almost the same in the case of basal and prismatic slip systems. In contrast, the case of pyramidal slip systems leads to a maximum discrepancy of about 10% mismatch.

Table 6.2: Schmid factor of each slip systems with different loading axis.

Slip System	Miller-Bravais Indices		TRIDIS			Loading Direction											
	Plane	Burgers	Plane	Screw	Edge	c		a		Prismatic		45-degree from c		45-degree from c		31 degree from c	
						[0001]	[111]	[1120]	[011]	[1010]	[11-2]	[1122]	[102]	[1011]	[811]	[1123]	[10 3 17]
Basal (0001)<11-20>	(0001)	[2-1-10]	(111)	[-1 0 1]	[-1 2 -1]	0	0	0	0	0	0	0.249	0.245	0.432	0.433	0.447	0.431
	(0001)	[-12-10]	(111)	[1 -1 0]	[-1 -1 2]	0	0	0	0	0	0	0.249	0.245	0	0	0.223	0.215
	(0001)	[11-20]	(111)	[0 -1 1]	[-2 1 1]	0	0	0	0	0	0	0.499	0.490	0.432	0.433	0.223	0.215
Prismatic	(01-10)	[2-1-10]	(1-21)	[-1 0 1]	[1 1 1]	0	0	0.433	0.433	0.433	0.433	0.199	0.173	0.230	0.214	0	0
	(10-10)	[-12-10]	(11-2)	[1 -1 0]	[1 1 1]	0	0	0.433	0.433	0	0	0.199	0.173	0	0	0.119	0.107
	(-1-100)	[11-20]	(-2 1 1)	[0 -1 1]	[1 1 1]	0	0	0	0	0.433	0.433	0	0	0.230	0.214	0.119	0.107
Pyramidal(π1) (01-11)<11-20>	(01-11)	[2-1-10]	(17 -13 17)	[-1 0 1]	[13 34 13]	0	0	0.382	0.388	0.382	0.388	0.293	0.264	0.407	0.384	0.210	0.191
	(0-111)	[2-1-10]	(-1 9 1)	[-1 0 1]	[-27 -6 -27]	0	0	-0.382	-0.388	-0.382	-0.388	-0.059	-0.047	0	0	0.210	0.191
	(10-11)	[-12-10]	(11 -9)	[1 -1 0]	[27 27 6]	0	0	0.382	0.388	0	0	0.293	0.264	0	0	0.210	0.191
	(-1011)	[-12-10]	(17 17 -13)	[1 -1 0]	[13 13 34]	0	0	-0.382	-0.388	0	0	-0.059	-0.047	0	0	0.210	0.191
	(-1101)	[11-20]	(9 -1 -1)	[0 -1 1]	[6 27 27]	0	0	0	0	-0.382	-0.388	0.235	0.217	0	0	0	0
	(1-101)	[11-20]	(13 -17 -17)	[0 -1 1]	[34 13 13]	0	0	0	0	0.382	0.388	0.235	0.217	0.407	0.384	0	0
Pyramidal(π2) (11-22)<11-2-3>	(-12-12)	[1-213]	(22 -8 7)	[3 17 10]	[11 -2]	0.446	0.431	-0.112	-0.108	0	0	0.302	0.339	0.209	0.218	0.193	0.189
	(-2112)	[2 1 -13]	(22 -7 -8)	[3 10 17]	[-1 2 -1]	0.446	0.431	-0.112	-0.108	-0.335	-0.323	0.078	0.091	-0.164	-0.162	0	0
	(-1-122)	[11-23]	(7 22 -8)	[10 3 17]	[-2 1 1]	0.446	0.431	-0.447	-0.431	-0.335	-0.323	-0.189	-0.162	-0.164	-0.162	0.193	0.189
	(1-212)	[-12-13]	(-8 22 7)	[17 3 10]	[-1 -1 2]	0.446	0.431	-0.112	-0.108	0	0	0.078	0.091	0.209	0.218	0.394	0.407
	(2-1-12)	[-2113]	(-8 7 22)	[17 10 3]	[1 -2 1]	0.446	0.431	-0.112	-0.108	-0.335	-0.323	0.302	0.339	0.225	0.277	0.402	0.437
	(11-22)	[-1-123]	(7 -8 22)	[10 17 3]	[2 -1 -1]	0.446	0.431	-0.447	-0.431	-0.335	-0.323	0.260	0.335	0.225	0.277	0.394	0.407

6.3.4 Critical resolved shear stresses (CRSS) of each slip system

As introduced in equation (6.3), the Peierls stress is the critical shear stress required to make a dislocation move in an otherwise perfect crystal. In other words, a certain amount

of shear stress is needed for the atoms to overcome the energy barrier when one atom moves from its original position to another position. Peierls stress gives raise to the unique CRSS value for each slip system. It is well known that the CRSS of fcc material such as copper is about 1.25MPa and this value is same for all the 12 equivalent slip systems. In contrast to fcc materials, hcp materials have several families of slip systems with different CRSS value that we need to identify from literature. Values retained for the different CRSS values are listed in Table 6.3. One should be aware that there is still a lack of understanding of the CRSS for the pyramidal slip systems. In contrast to the case of basal and prismatic slip systems, the CRSS of pyramidal system is still unclear. Moreover, the CRSS of pyramidal $\pi1$ slip system has not been reported yet, to the author knowledge. Therefore, we decided to vary the CRSS on $\pi1$, and the results will be discussed in the next chapter.

Slip system	CRSS(MPa)	note	reference
basal	0.5	experimental	[Yoshinaga et al. 63]
			[Burke et al. 52]
			[Conrad et al. 57]
	0.6	experimental	[Bian et al. 09]
prismatic	39.2	experimental	[Reed-Hill 57]
	22	numerical	[Liu et al. 07]
	23	numerical	[Sun et al. 06]
pyramidal($\pi2$)	102	numerical	[Staroselsky et al. 03]

Table 6.3 CRSS values of slip systems of magnesium.

6.3.5 Rotation of the loading axis

In the case of tensile uniaxial loading conditions, it is well known that when a perfect single crystal deforms by accumulating plastic shear strains on the different slip systems, the orientation of the tensile axis in the crystallographic frame changes. As an example, in the case of [0001] orientation, the initial loading axis was perfectly aligned with [0001] axis. The Schmid factor corresponding to basal slip systems, therefore, is zero although we have observed experimentally a large dislocation activity in these systems, leading to strain bursts. It is possible to reproduce numerically this instability by continuously updating the position of the tensile axis in the crystallographic frame according to the rotation induced by the anti-symmetric part of the displacement gradient.

In the case of [0001] compression, the shear strains cumulated on the pyramidal $\pi2$ slip systems may induce a global rotation of the simulated sample that will change the Schmid factors and consequently may promote dislocation activity on the basal systems. This global rotation of the tensile/compression axis in the microscopic frame has been implemented in

TRIDIS in order to check these ideas.

6.3.6 Geometry of the simulated volume

The simulated volume is taken as a cylinder with 2µm of diameter and 6µm of height. This volume contains the real dislocation segments interacting with each other. The volume is surrounded by a bigger cylinder defining the virtual space. This virtual space contains the virtual segments who escaped the crystals and that will be used for the calculation of the shape of the deformed sample.

6.3.7 Reducing computation time

A key limitation of DD simulations is the CPU time required to perform a realistic simulation. In the case of micro-pillar compression, the amount of plastic strain accumulated during a typical simulation can be quite large. It is therefore interesting to use specific tricks in order to save time.

Removing virtual closed loops

In order to boost the calculation speed, dislocation loops totally located outside the pillar are removed, as shown in Figure 6.2. This reduces the calculation of the dislocation interactions located outside the pillar (i.e. the virtual segments). Of course these segments are taken into account in the post-treatment calculation of the deformed volume.
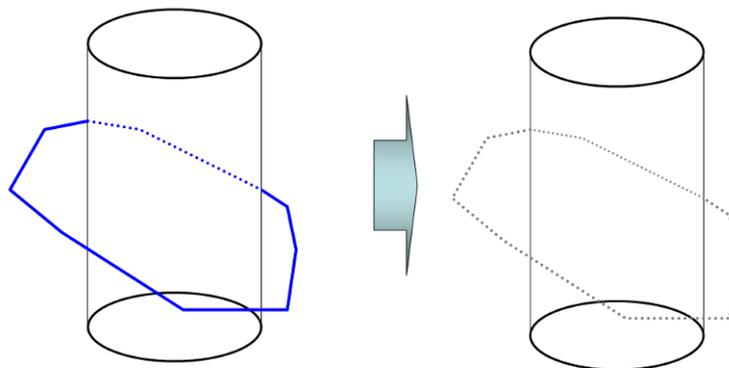
Figure 6.3. Elimination of dislocation loops when totally located outside the pillar.

Image forces are neglected

In real materials, all the surfaces of the micro-pillars (except the bottom one) are traction-free. This means that the normal stress vector computed at these positions is zero. However since we introduce dislocations in the cylinder, they generate stress fields that do not

satisfy this condition. In practice one should compute the stress vector at the surfaces induced by the dislocation and solve the elastic problem for which these forces are imposed with an opposite sign on the free surface. This would create an image stress field that needs to be added to the internal stress field induce by all the dislocations in order to compute the effective stress at each dislocation center. The image stress field can be computed using finite element methods as proposed by Needleman *et al.* in 2D and implemented in 3D in TRIDIS ([Giessen & Needleman 95]).

In the simulations presented here, these image stresses are neglected in order to save computation time.

Cross-slip is neglected

Although the slip systems have been all defined in a way that cross-slip is possible between slip systems sharing a given Burgers vector (see section 6.3.2), we decided not to allow cross-slip in these calculations in order to reduce the number of parameters to vary in our study.

6.3.7 Simulation parameters

TRIDIS simulation parameters used in the simulations of hcp micro-pillars are listed in Table 6.4. Note that the material properties such as the dislocation mobility, might be different depending on the slip system. However, due to the lack of the understanding of hcp, especially magnesium, the viscous drag coefficient was fixed with the value generally attributed to basal planes. The initial dislocation density consists of a set of initial dislocation sources whose length and CRSS are used as variable. Simulation results will be discussed in the next chapter.

Material property	value
shear modulus	17GPa
poisson's ratio	0.34
Burgers vector	3.2Å
simulation lattice	32Å
viscous drag coefficient	0.5×10^{-6}Pa·s
time step	1×10^{-10}s

Table 6.4 Some important parameters used in DD simulations

Key points of Chapter 6

1. fcc version of TRIDIS was adapted to hcp systems using an equivalence between the [111] direction of fcc crystals and the [0001] direction in hcp.

2. The 4 different slip systems (basal, prismatic, pyramidal $\pi1$ and pyramidal $\pi2$) are introduced. A CRSS is attributed to each slip system.

3. The micro-pillar compression is simulated by applying a uniaxial compression stress along a loading axis. The orientation of the loading axis is updated during the deformation as a result of the dislocation activity.

4. The simulated volume is defined as a cylinder (2µm diameter – 6µm height) containing the dislocations, surrounded by a virtual space where virtual segments are stored in order to give access to the shape of the deformed volume.

5. Image forces are neglected in order to save computation time

6. Cross-slip is not accounted for in the simulations

<div align="right">

CHAPTER 7.

</div>

Simulation results and discussion

7.1 Effect of simulation parameters on the simulation results

It is well known that the initial dislocation microstructure plays an important role in plastic behavior at the micron or smaller scale ([Motz *et al*. 09], [Norfleet *et al*. 08]). In order to investigate this effect, DD simulations were performed with different initial dislocation configurations: Both the length and the number of the dislocation sources are modified.

In addition, various CRSS were tested to find the best fit between the simulations and experimental results.

In section 7.1, we will summarize the simulation results obtained with the different simulation parameters in the case of [0001] orientation of the compression axis. Following this section, some representative simulation results are presented in section 7.3 in order to discuss the deformation behavior of micro compression test of [0001] and [2-1-12] orientations.

7.1.1 CRSS effect

As we discussed in Chapter 6.3.2 and 6.3.3, there is no consensus regarding the CRSS value on each of the hcp slip systems. Large uncertainties still exist so that we have used DD simulations to test how the CRSS values affect the simulation results.

According to Table 6.3, the CRSS of basal slip system is very low and generally estimated to 0.5MPa in the literature.

For prismatic slip system the CRSS was reported about 20~40MPa as shown again in Table 6.3. However, in some macroscopic simulations performed using the Visco Plastic Self Consistant model (VPSC) model, it is suggested that the prismatic CRSS is about 10 times greater than on basal slip system which leads to 5MPa ([Agnew *et al*. 01]). Thus, we decided to test the three following values of the CRSS on prismatic slip system: 5, 30 and 100MPa.

Estimating the CRSS on pyramidal slip systems is quite complicated. As mentioned in Chapter 2, although many reports dealing with the existence and observation of pyramidal $\pi 1$ slip system in actual magnesium have been published, it has never been possible to measure

the CRSS of pyramidal π1 slip systems because there is no way to activate only the pyramidal π1 slip system excluding the other slip systems nor the twin systems experimentally. Due to such a lack of understanding about the CRSS of pyramidal π1 slip system, some researchers decided not to take into account pyramidal π1 slip system in their modeling ([Agnew *et al.* 05]). In our study, we assume that the CRSS of pyramidal π1 slip system is equal to the one of pyramidal π2. And the CRSS on these two pyramidal systems was varied within the set 1, 20, 30, 40 and 100MPa.

For this study of the effect of the CRSS, the initial dislocation density is fixed to $1.2\times10^{13}m^{-2}$, and the length of the initial dislocation sources is varied in the range 1.5μm~2.5μm. The loading axis is [0001].

In order to compare the simulation results to experiments, a typical loading curve corresponding to a microcompression test of a 2μm diameter column is presented with the black solid line in Figure 7.1.
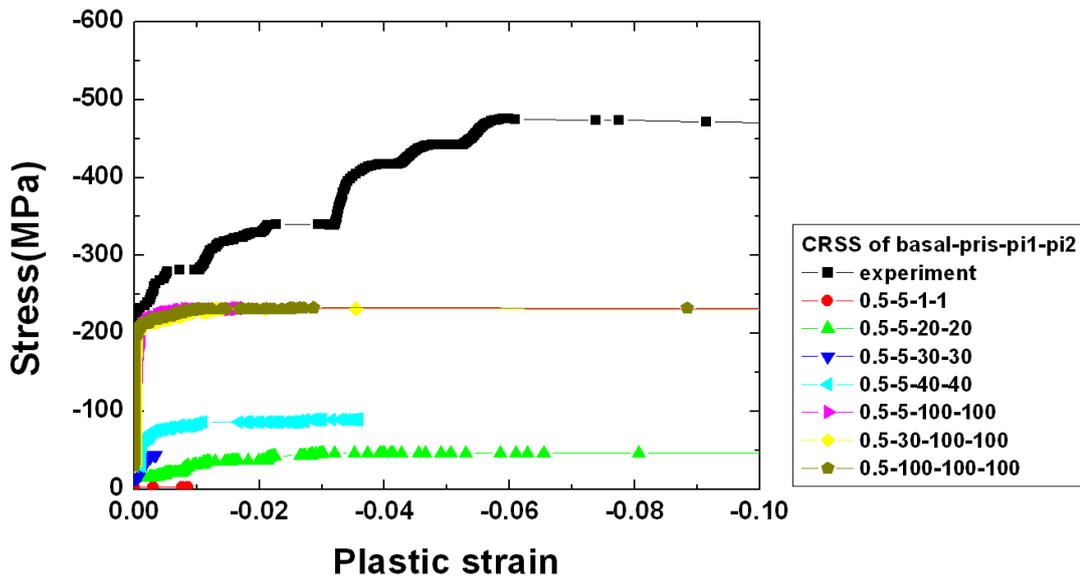
Figure 7.1 Stress-plastic strain curve with different CRSS on the hcp slip systems.

As we discussed in Chapter 4.1 and presented in Figure 4.1, we have evidenced a plastic deformation region for strain in the range of 0~2% although the mechanical response was linear. We attributed this plastic deformation in the linear part to a micro yielding at some part of the column, most likely the top part, due to the friction between the column and the flat punch. Without such a boundary effect, the overall behavior would have been purely elastic. In Figure 7.1 plotted above, only the plastic part of the curve has been reported by subtracting the linear response to the global experimental curve. This way, the experimental curve can be directly compared to DD simulations.

Figure 7.1 also shows the stress-strain response of DD simulations with different values of the CRSS on the slip systems. The stress strain behavior is undoubtedly dependent on the CRSS of pyramidal π2 and the best fit was found for a CRSS of 100MPa on pyramidal

systems π2. This value is consistent with the value given in Table 6.3. The green curve (triangle symbols) in Figure 7.1 has been obtained for a CRSS value on pyramidal π2 of 20MPa. This choice of CRSS on π2 obviously induces a much lower applied stress compared to the case of 100MPa. In contrast, figure 7.1 shows that there is no remarkable effect of the CRSS on prismatic slip system. This can be explained because the prismatic slip system does not play a major role in the case of uniaxial compression along a [0001] orientation.

Strain burst was observed in all DD simulations and the critical strain above which strain burst occurs is getting smaller as the CRSS of pyramidal π2 slip system is increased. This may be explained by the fact that a relatively low CRSS on π2 induces an easy activity for the <c+a> dislocations at the early stage of the deformation so that the dislocations can all reach a position that minimizes the energy stored in the system. In contrast, when the CRSS on pyramidal π2 slip system is higher, <c+a> dislocations are hard to move, leading to a bigger energy stored inside the column. The CRSS being the same in the two cases, the energy released when the basal system is activated leads to a larger massive glide of <a> dislocations in the case of the high CRSS on π2. as will be discussed in Chapter 7.2.

Another remarkable result of the DD simulations is the difference of hardening behavior between experiments and simulation. The hardening was not reproduced even when we changed either the initial dislocation length or the initial dislocation density. This will be also discussed in Chapter 7.2.

7.1.2 Effect of the initial dislocation density

The dislocation density is well known to induce two different opposite actions in terms of deformation behavior of a material. For example, a higher forest dislocation density introduces higher probability of junction formation which causes strain hardening. On the other hand, a higher density of mobile dislocations would make deformation easier. When we introduce a set of pinned dislocation sources in the simulation box, we do increase the later quantity (mobile dislocations) but we will also promote the generation of forest dislocations.

The choice for the initial dislocation density should be dictated by experimental observations. Unfortunately, it is unclear how many dislocations exist in the undeformed Mg sample we used in this research. Despite our efforts to perform TEM observation, we didn't succeed to quantify the initial dislocation density. Probably, the number of dislocations was not big enough to be observable or the TEM foil was too much damaged by Ga ions. However, some measurements are available in the literature although not on pure Mg pillars. Norfleet *et al*. ([Norfleet *et al*. 07]) have measured in Ni micro pillars the initial dislocation density as well as its evolution with the column deformation. To do so they used the interception method from TEM observations ([Norfleet *et al*. 08]). In the case of a 2µm diameter column, they found an initial dislocation density comprised between $1.5 \times 10^{13} \text{m}^{-2}$ and $7.5 \times 10^{13} \text{m}^{-2}$ as shown in Figure 7.2.
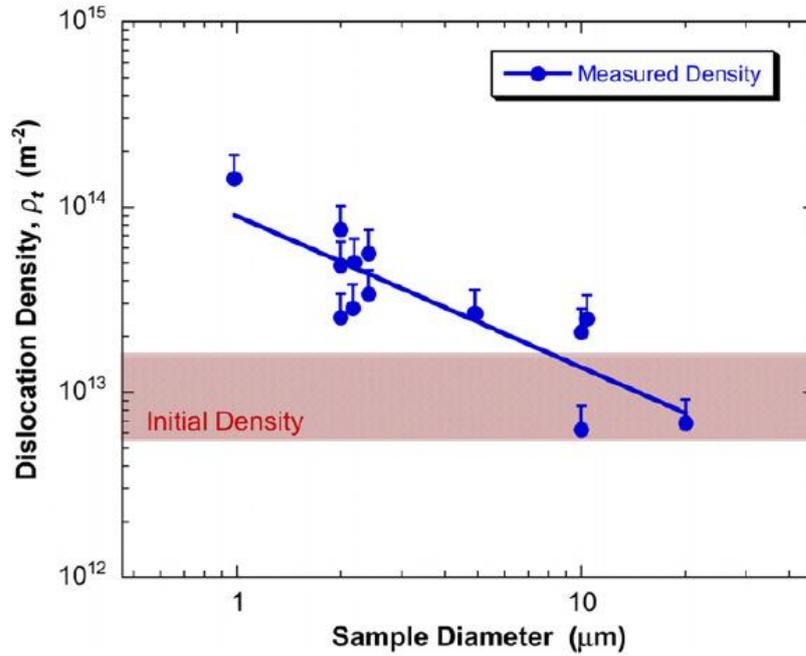
Figure 7.2: Initial dislocation density of undeformed pure Ni column. ([Norfleet *et al*. 08])

Based on this work, we decided to perform DD simulations with the two following values for the initial dislocation density: $1.2 \times 10^{13} \text{m}^{-2}$ and $2.4 \times 10^{13} \text{m}^{-2}$. Note that a similar initial dislocation density of $2.2 \times 10^{13} \text{m}^{-2}$ was selected by Weygand *et al*. ([Weygand *et al*. 08]).

Figure 7.3 shows the two designs of the initial dislocation configuration. The blue, green, yellow and red colors correspond to the basal, prismatic, pyramidal $\pi1$, pyramidal $\pi2$ dislocations, respectively. The CRSS on basal, pyramidal $\pi1$ and pyramidal $\pi2$ is 0.5, 100, 100MPa, respectively. Two values will be tested for the CRSS on prismatic slip system: 5MPa and 30MPa. The set of initial dislocation sources was distributed randomly with a random length in the range [1.5~2.5μm].
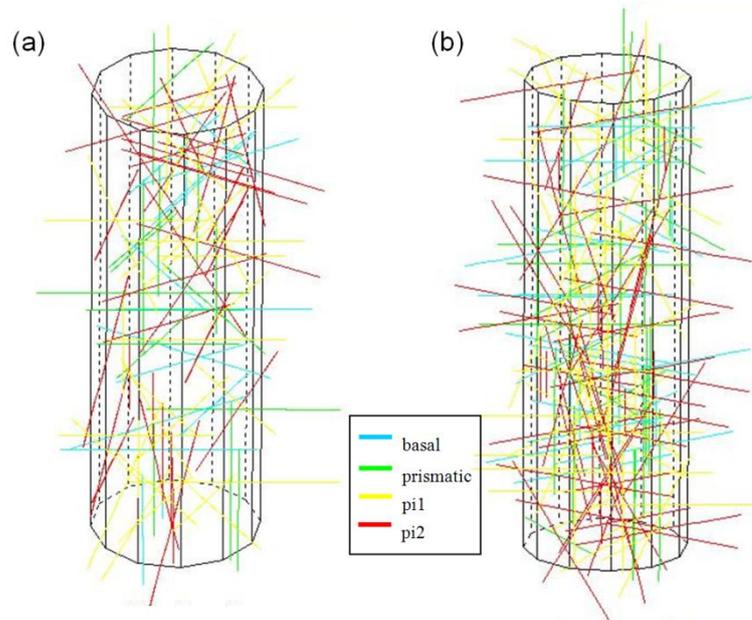
Figure 7.3: Initial dislocation configurations used in the simulations (a) $1.2\times10^{13}\text{m}^{-2}$ (b) $2.4\times10^{13}\text{m}^{-2}$. Each of pillars has 2µm of diameter.

Figure 7.4 shows the stress-strain curves obtained from the DD simulations. There is no clear evidence that the initial dislocation density affect the maximum stress. One of the major effects of the initial dislocation density on the stress-strain curve stands in the occurrence of the strain burst. According to our experimental data, strain burst occurred at around 6% of cumulated plastic strain. In the DD simulations, the strain bursts are delayed when the dislocation density is increased. In the case of the largest dislocation density, the strain bursts are no more evidenced and the loading curve display a continuous strain hardening. For lower density, strain burst occur for a very low value of the cumulated plastic strain.

Figure 7.4 also reveals that the increase of the CRSS on the prismatic slip system causes a shift of stress-strain toward the left side. Since prismatic slip system does not accommodate the applied loading along [0001], it is not easy to understand this effect which cannot be explained in term of stored energy. It may rather be related to the capability for the dislocations to interact with the highly mobile basal dislocations. But more simulations are needed to draw a conclusion on this effect.
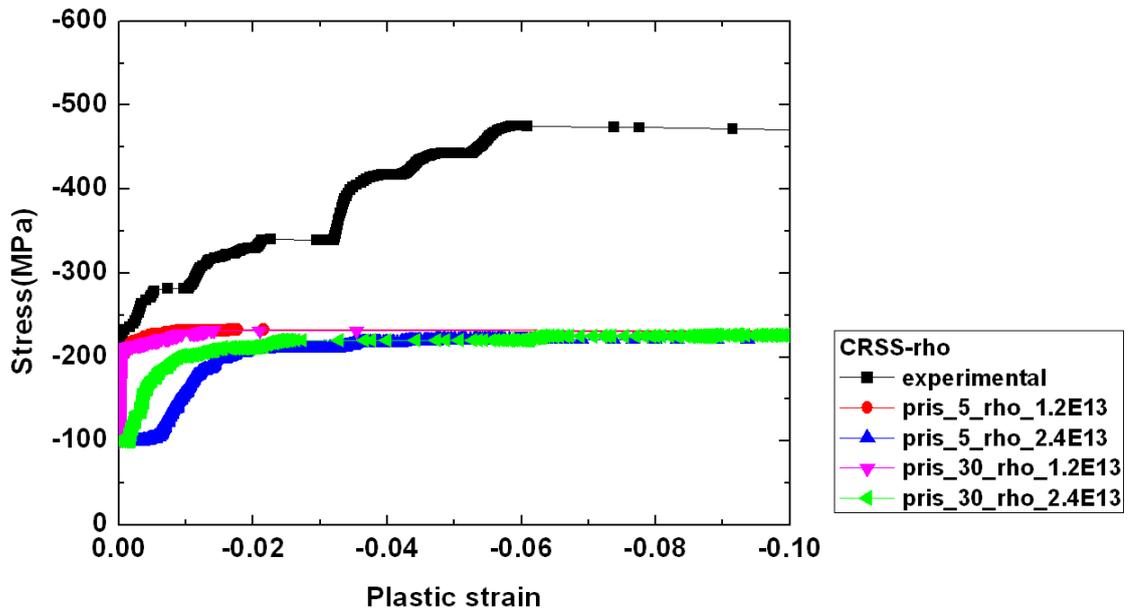
Figure 7.4 Stress-strain curves obtained for different CRSS of prismatic slip system and initial dislocation density. The CRSS values of basal, pyramidal $\pi 1$ and pyramidal $\pi 2$ slip system are 0.5, 100, 100MPa.

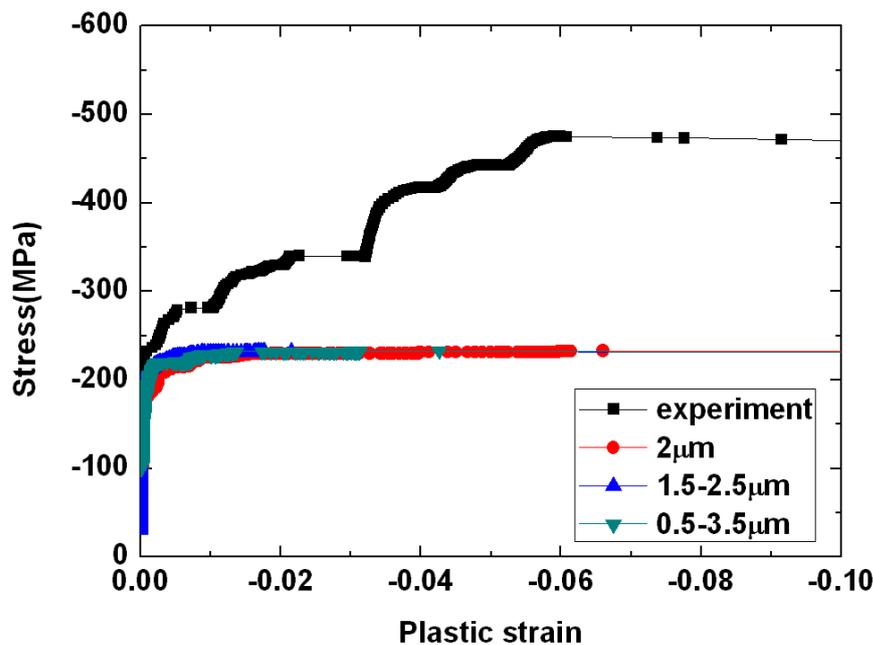## 7.1.3 Effect of the initial dislocation source length

The effect of the length of the initial dislocation sources on the plastic behavior of pillar has already been investigated in the past years. For example, Weygand *et al*. performed DD simulations to study the size effect with a fixed size of 220nm for all the initial dislocation sources ([Weygand *et al*. 08]). In contrast, El-Awady *et al*. also carried out DD simulations to investigate the size effect but with a Weibull distribution of the dislocation source size ([El-awady *et al*. 09]). In both cases, dislocation multiplication is imposed through the classical Frank-Read mechanism when the two pinning point of the sources are both inside the sample or through spiral sources when a single point is located in the pillar.

In this work, three types of simulations have been carried out in terms of source length. First, random dislocation sources with a constant length of 2μm are introduced. However it is generally admitted that the initial length for the dislocation sources in the pillar is smaller or equal to the diameter of the pillar. Following this idea, larger pillar can have longer dislocation source. Thus, we additionally performed two complementary DD simulations with random source length taken in the range [1.5~2.5μm], and [0.5~3.5μm]. Figure 7.5 shows the top view of the initial dislocation features for each case. The diameter of the column is fixed to 2μm, which means that both classical Frank-Read sources and spiral sources will be present in these simulations. The initial dislocation density was set to $\rho_0 = 1.2 \times 10^{13} \text{m}^{-2}$ in order to compare to the other results. Finally the CRSS on basal, prismatic, pyramidal $\pi 1$ and pyramidal $\pi 2$ is fixed to 0.5MPa, 5MPa, 100MPa and 100MPa respectively, also for comparison.
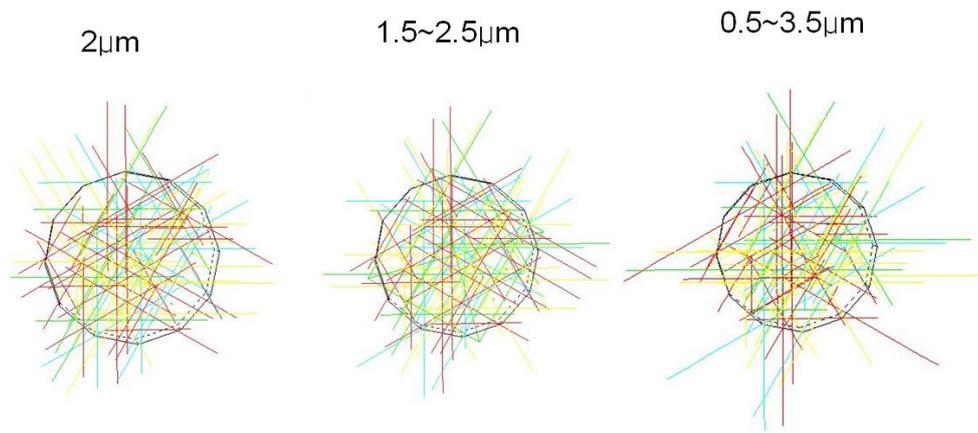
Figure 7.5: Initial dislocation features with different source length.

Figure 7.6 shows that the dislocation source length does not play a major role on the mechanical response of the compressed specimen. For all cases, the maximum compression stress saturates at a stress level of 230MPa. This may be explained by the weak-link source mechanism introduced by Norfleet *et al.* ([Norfleet *et al.* 08]). According to these authors, the mechanical behavior is dominated by weak-link dislocation source such as the longest single-pinned or Frank-Read source. Indeed, assuming that the stress in the column is overall homogeneous, the dislocations which have a longer initial length or which are single pinned will be firstly activated due to lower line tension. This process will stop only if such dislocation sources are exhausted due to interactions with other dislocations. From these simulations, it seems that the dislocation interactions are rather limited and that the weak-link source mechanism dominates.

Figure 7.6: The stress-strain behavior of experiment and simulations. The initial dislocation source length was varied.

In these simulations again strain burst was observed. However, there is still no clear evidence of the effect of the dislocation source length on the strain bust events. As discussed above, it seems that strain burst mainly depends on the dislocation density or other stochastic effects such as dislocation distribution rather than the source length.

7.2 Deformation process

In this section we will check how DD simulations reproduce the effect of the orientation of the compression axis.

7.2.1 [0001] orientation

Based on the simulation results presented in Chapter 7.1, two representative simulation results are now discussed for a better understanding of uniaxial microcompression test. In this simulation, the CRSS on basal, prismatic, pyramidal $\pi 1$ and pyramidal $\pi 2$ were set to 0.5MPa, 5/30MPa, 100MPa and 100MPa respectively. The initial dislocation density was fixed to $\rho_0=1.2\times10^{13}m^{-2}$ and randomly distributed both in space and in length within the range [1.5μm~2.5μm].
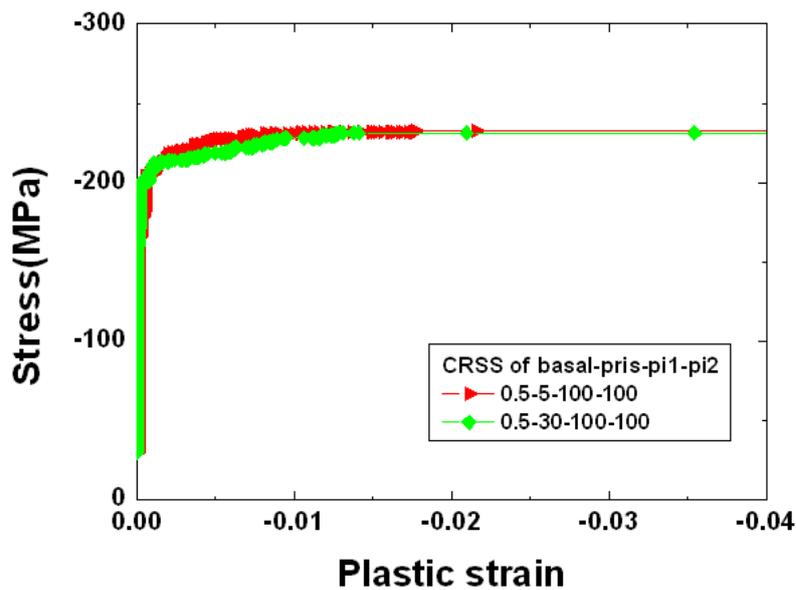
Figure 7.7: Typical DD simulation results for the [0001] orientation with two values for the CRSS on the prismatic system.

Figure 7.7 shows the stress-strain response corresponding to the [0001] orientation. The strain hardening appeared at the early stage of plastic deformation, until 1% of plastic strain, then a plateau is observed up to 1.5% above which strain bursts are observed in both cases. The strain hardening is mainly caused by the mutual interactions between the different pyramidal $\pi 2$ slip systems. The amount of cumulated plastic strain at the initiation of the

strain burst (1.5%) is smaller than our measurements which showed 5~6% of plastic strain. This mismatch between experiments and DD simulations has already been experienced in almost every DD simulations. Until recently no one succeeded to simulate the strain hardening in micropillar compression. No one except El-Awady *et al*. who were able to fit experiment data just by taking into cross-slip events in their DD simulations ([El-awady *et al*. 09]). This could explain the mismatch in term of strain hardening between the experiment and our DD simulations here.

Although the plastic strain level does not perfectly correspond to the experimental measures, the tendency in term of dislocation activities (namely the hardening followed by strain bursts) is similar and DD simulations give a better understanding of the experiments.
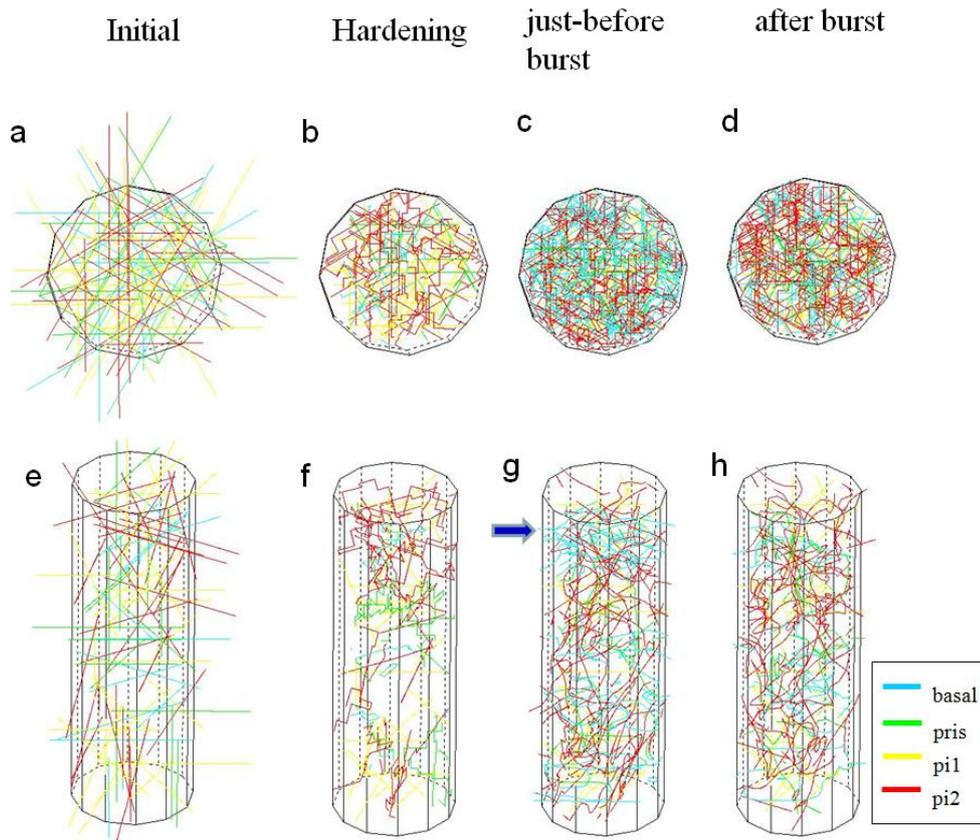
Figure 7.8: Dislocation organization inside the column with the deformation. (a), (e) initial configuration, (b),(f) hardening stage (c),(g) just before strain burst, (d),(h) just after burst. Strain burst is initiated by the basal dislocations pointed out by the blue arrow in (g).

In order to identify what occurred during the deformation, both virtual dislocations located outside the pillar and real dislocations included in the pillar are shown in Figure 7.9. Figure 7.9(a) shows the early dislocation structure after 20 steps of simulation, (b),(e) show the dislocations during the hardening stage, (c),(f) show the dislocations just before strain burst and (d), (g) show the dislocations after burst. Figure 7.9(a), (b), (c) and (d) are the top view whereas (e), (f) and (g) are the front view. The density of dislocation segments in the virtual space give insights about the amount of plastic strain accumulated on the different slip systems.
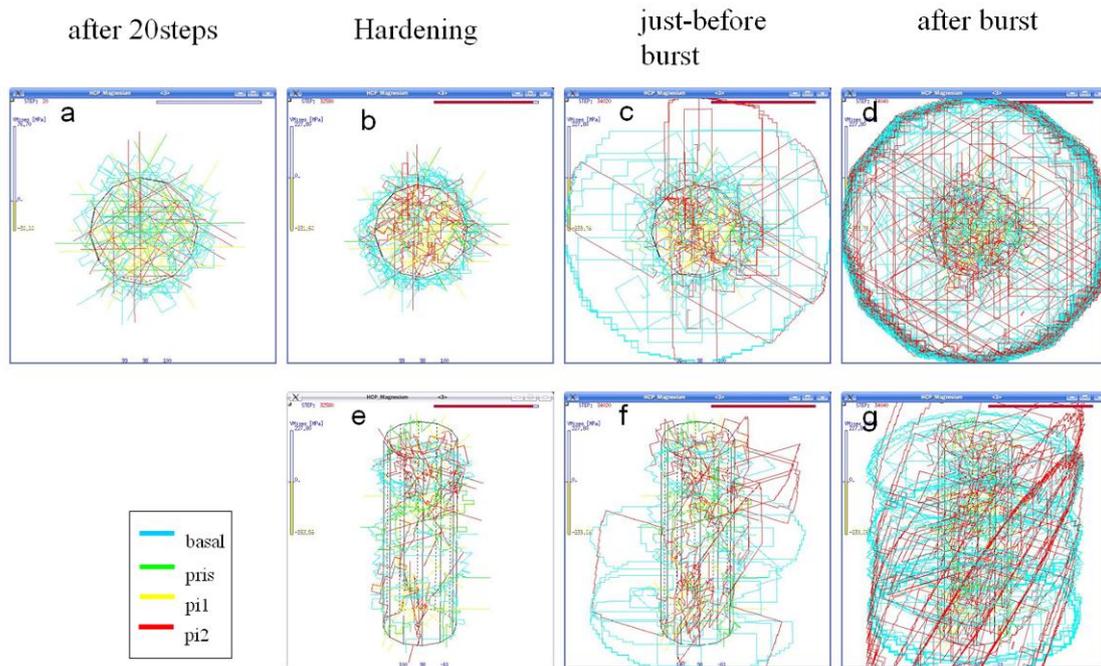
Figure 7.9: The dislocation features both outside and inside the column with the deformation. Snapshots taken at different time steps (a) after 20 steps of the simulation, (b), (e) during the hardening stage, (c), (f) just before the strain burst (d),(g) just after the strain burst

Initially the column is perfectly aligned with the [0001] axis. At the early stage of the deformation, pyramidal π2 slip system indicated by red color is not activated due to the high CRSS (Figure 7.9(a)). During the hardening stage, the six equivalent pyramidal π2 slip are simultaneously activated. Dislocations on π2 multiply and form numerous junctions with other π2 dislocations but also with basal, prismatic and pyramidal π1 slip system (Figure 7.9(b), (e)). Such a dislocation activity causes inhomogeneity of the dislocation spreading over the pillar. Therefore, dislocations in one or two slip systems among the six equivalent pyramidal π2 slip systems glide intensively (Figure 7.9(c), (f)) leading to crystal reorientation. The local reorientation is also supported by the experimental results which reported about 9 degrees local reorientation as shown in Figure 4.4. The crystal reorientation results in a massive amount of basal dislocations escaping the pillar because the Schmid factor on basal slip system is no more zero. Finally, both the massive basal slip as well as pyramidal π2 slip is observed as shown in figure 7.9(d) and (g).

Figure 7.10 shows the schematic image of the deformation process. In summary, at the initial state, because the loading axis is well aligned to the [0001] direction, only pyramidal π2 slip system can contribute the deformation (Figure 7.10(a)). As the pyramidal π2 dislocation escape the pillar, the pillar axis is rotated from the loading axis. In addition, there is a local inhomogeneity in the dislocation spreading over the pillar due to the dislocation activity (Figure 7.10(b)). For that reason, basal dislocations can be activated (Figure 7.10(c)). These basal dislocation are then trapped inside the pillar until the effective

stress applied the weakest each basal dislocation can overcome the forest dislocations made of pyramidal π2 dislocations, basal dislocation. Basal dislocation then glide over large distance leading to important strain bursts.
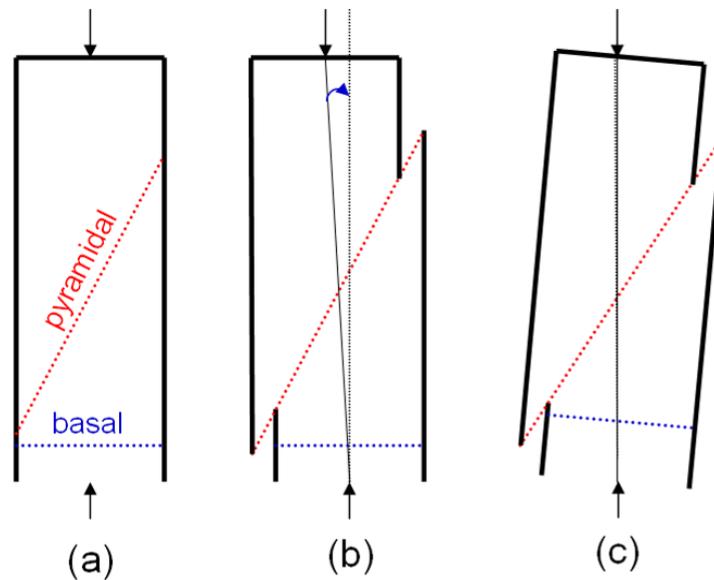
Figure 7.10: Schematic description of the deformation process in the case of [0001] orientation of the compression axis. (a) initial (b) activation and gliding of pyramidal slip systems. The pillar axis is tilted from the initial loading axis due to the local misorientation induced by pyramidal slip. (c) massive basal slip occurs.

The computed shapes of the deformed pillar are shown in Figure 7.11. In Figure 7.11(a) and (b), the image post-processing based on the virtual segments was performed. The CRSS of basal, prismatic, pyramidal π1 and pyramidal π2 is 0.5, **5**, 100 and 100 MPa, respectively for case (a), whereas 0.5, **30**, 100 and 100 MPa, respectively for case (b). The black arrow in (a) indicates the slip mark from the prismatic slip. A typical SEM picture of an actual deformed pillar is given in (c) for comparison.

It is unclear whether there is a slip activity on prismatic slip system or not in the actual [0001] orientated pillar given in Figure 7.11(c). Indeed, it would be difficult to visualize plastic steps with an amplitude lower than a fewer tens of nanometers. However DD simulations did exhibit strain bursts in both cases: with a high and also with a low CRSS on the prismatic system.
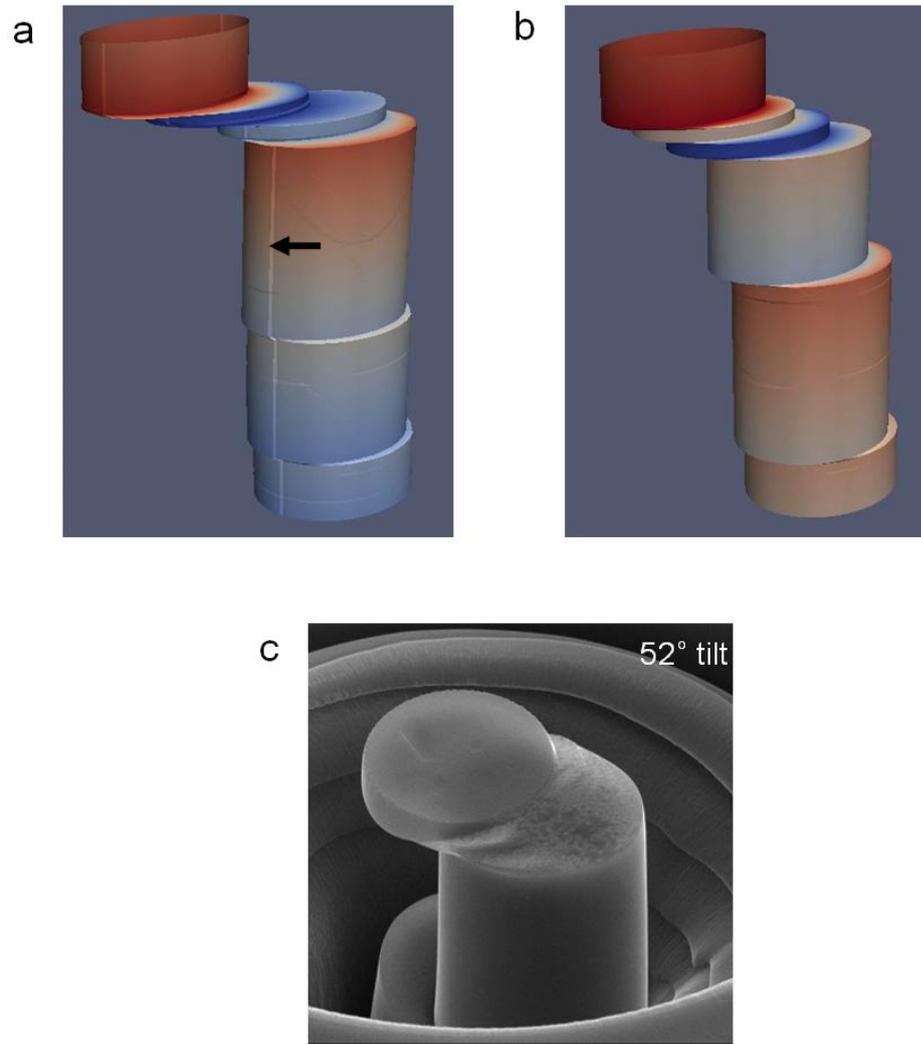
Figure 7.11: Deformed shape of the pillar compressed along [0001]. DD image processing was applied to (a) and (b). The CRSS of basal, prismatic, pyramidal $\pi1$ and pyramidal $\pi2$ is 0.5, **5**, 100, 100, respectively for the case of (a), whereas 0.5, **30**, 100, 100, respectively for the case of (b). The black arrow in (a) indicates a typical slip mark corresponding to prismatic slip. The actual deformed pillar is given in (c) for comparison.

7.2.2 [2-1-12] orientation

The simulation result of microcompression tests along [2-1-12] are presented in this chapter. The Schmid factor on each slip system corresponding to this orientation is given in Table 6.2. The basal plane is tilted close to 45 degrees from the loading axis. As a result, the Schmid factor of the basal slip system is 0.49, i.e. close to maximum. Therefore, only basal slip system has the major contribution to the plastic strain. Figure 7.12 shows the stress-strain behavior computed from DD simulation. The CRSS of basal, prismatic, pyramidal $\pi1$, pyramidal $\pi2$ is 0.5, **5**, 100, 100 MPa, respectively, for the case of the blue curve, whereas, 0.5, **30**, 100, 100 MPa, respectively, for the case of red curve. In both cases, the stress saturates in the early stage of the deformation and no hardening is observed. This is because the basal

dislocations activate and escape the pillar continuously.
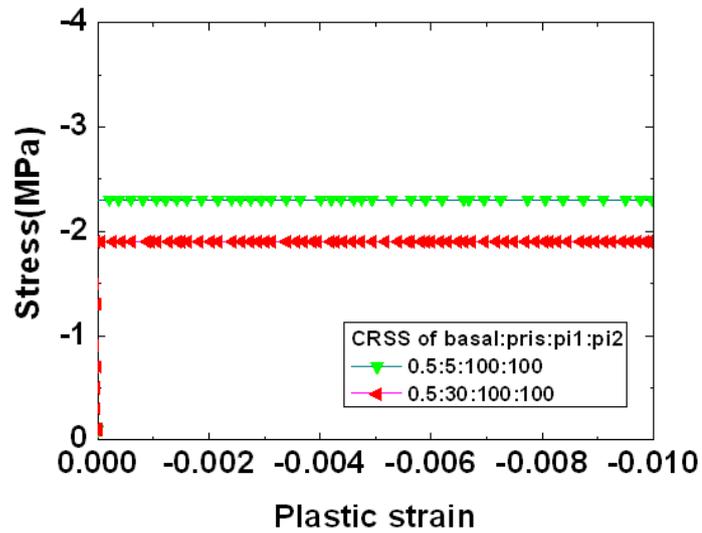
Figure 7.12 The DD simulation results of [2-1-12] orientation. In both cases, the stress saturates in the early stage of the deformation and no hardening is observed

Figure 7.13 shows the dislocation microstructure inside the column. Basal dislocations are the only one to multiply and interact with other dislocations. However, the dislocation microstructure seems to remains globally similar all along the simulation duration. No strain localization is observed.
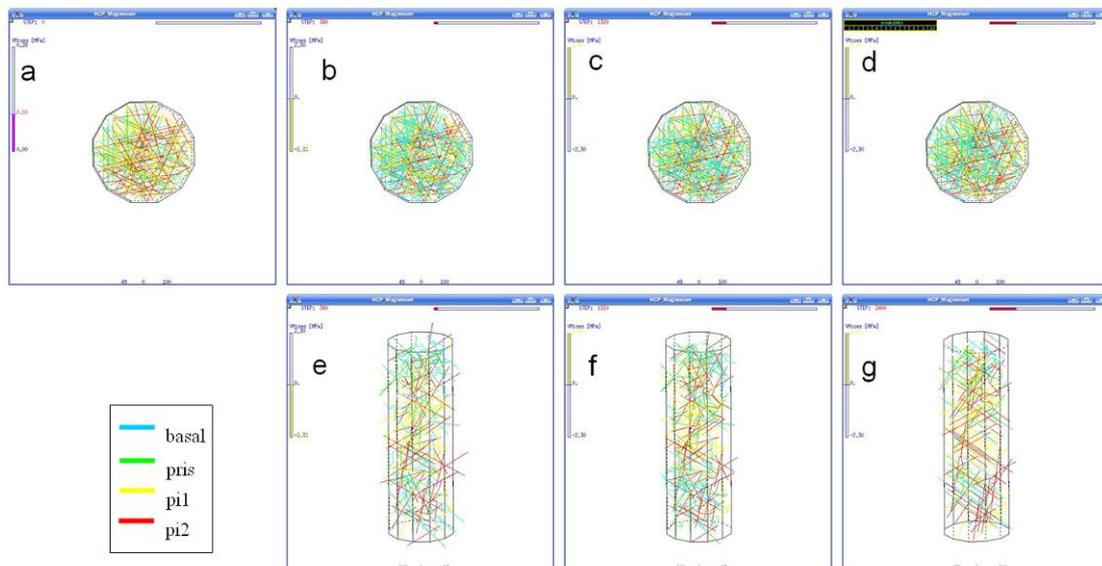
Figure 7.13: Dislocation microstructure inside the column as a function of the deformation. (a) initial, (b),(e) time step #380, (c), (f) time step #1320, (d),(g) time step #2400.

Figure 7.14(a) and (b) show titled images of the 3D view in order to point out the dislocation localization. The basal dislocations are plotted as blue lines. Figure 7.14 reveals that the deformation is mainly accommodated by the basal dislocations.
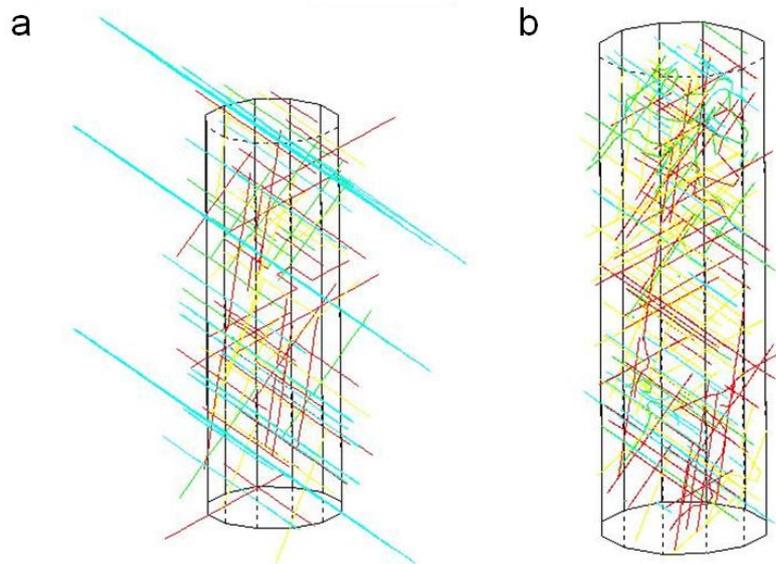
Figure 7.14: Tilted view of the simulated volume. (a) Total dislocation microstructure including bulk and virtual segments. (b) Bulk only dislocations contained in the pillars.

Based on the DD simulation results, a new scenario of the deformation process can be drawn out as depicted in Figure 7.15.
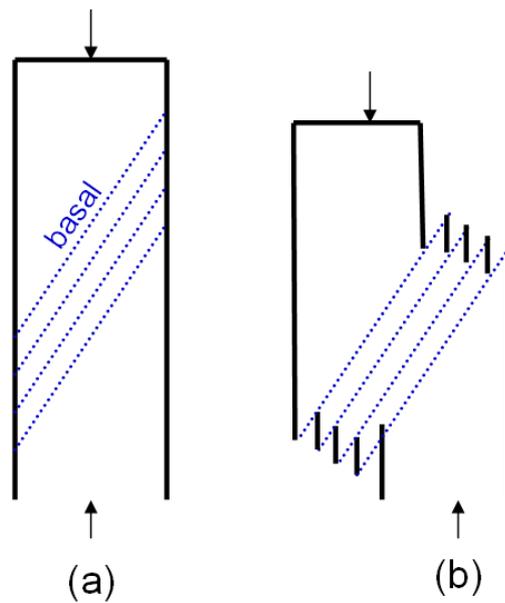
Figure 7.15: Schematic description of the deformation process in the case of [2-1-12] orientation. (a) initial (b) activation and glide of numerous basal dislocation.

Because the basal slip plane has 45 degree with loading axis (Figure 7.15(a)), only basal dislocation is activated during the loading (Figure 7.15(b)).

Snapshots of the shape of the deformed pillar are shown in Figure 7.16. The CRSS on basal, prismatic, pyramidal π1 and pyramidal π2 is 0.5, **5**, 100, 100 MPa, respectively for case (a), whereas 0.5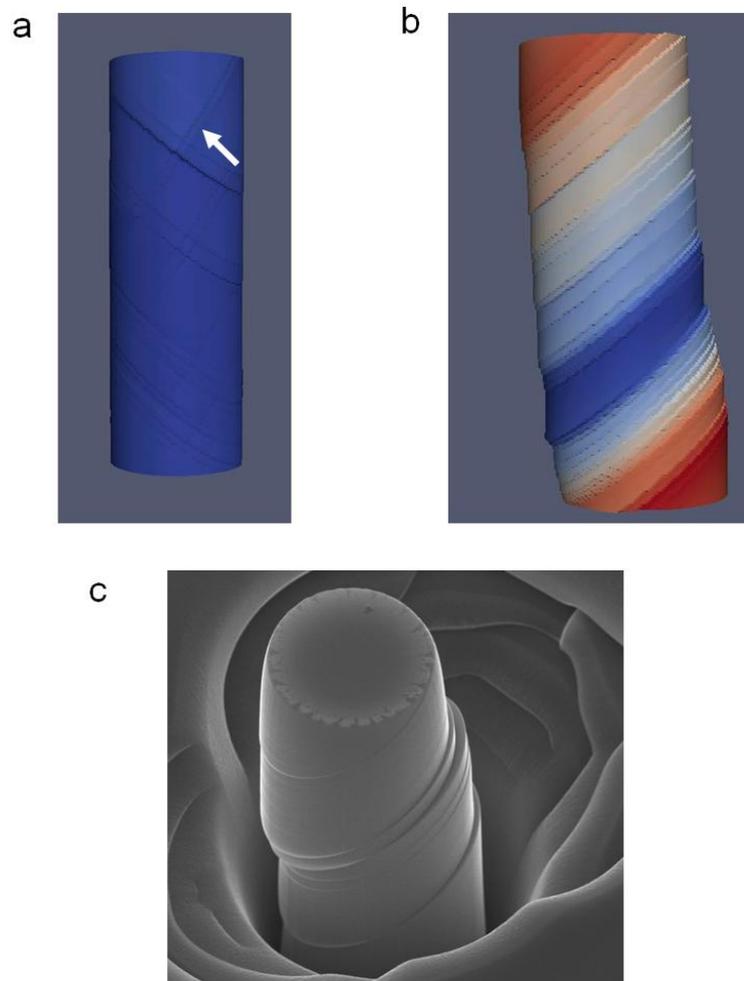, **30**, 100, 100 MPa, respectively for case (b). The white arrow in (a) indicates a slip mark from the prismatic slip. The actual deformed pillar is given in (c) for comparison. As in the previous case, it is unclear whether there is a dislocation activity on the prismatic slip system in the actual [2-1-12] orientated pillar.

In conclusion, in both cases DD simulations predict a rather homogeneous plastic strain within the pillar which is in good agreement with the SEM observations. But once again, it is impossible to conclude about dislocation activity on prismatic system and consequently the value of the CRSS on this system.

Figure 7.16: Shape of the deformed [2-1-12] pillar. DD simulation obtained with a CRSS of basal, prismatic, pyramidal π1 and pyramidal π2 of (a) 0.5, **5**, 100, 100 MPa, respectively and (b) 0.5, **30**, 100, 100 MPa, respectively. The white arrow in (a) indicates a slip mark from the prismatic slip. The actual deformed pillar is given in (c) for comparison.

Key points of Chapter 7

1. Parametric DD simulations were performed to study the uniaxial microcompression along [0001] orientation.

2. Parameters were:
  - the CRSS on pyramidal systems: 1, 20, 30, 40 and 100MPa were tested.
  - the CRSS on prismatic system: 5 and 30 MPa were tested.
  - the initial dislocation density: $1,2.10^{13}m^{-2}$ and $2.4 \ 10^{13} \ m^{-2}$ were tested.
  - the length of the dislocation sources: L=2µm, L in [1.5;2.5µm] and L in [0.5;3.5µm] were tested.

3. The effect of the CRSS on pyramidal systems governs the yield stress

4. The retained set of parameters for the CRSS values on basal, prismatic, π1 and π2 are 0.5, 5~30, 100, 100MPa, respectively.

5. The initial dislocation density affects the strain bursts: the highest density prevents the apparition of strain bursts.

6. The source length does not affect the stress-strain behavior of the [0001] orientation. The deformation is controlled by the weakest link mechanism in term of Frank-Read sources.

7. The full deformation process was identified in the case of the [0001] orientation. The six equivalent pyramidal π2 slip are activated, multiply and form junctions. This induces inhomogeneity of the dislocation microstructure and crystal reorientation. The crystal reorientation results in a massive activity of basal dislocations leading to strain bursts.

8. The [2-1-12] orientation shows a large and homogeneous dislocation activity on the basal slip systems.

9. Despite these analyses, one could not conclude regarding the best choice for the CRSS on prismatic slip systems.

Part III.

General conclusion and perspective

General conclusion and perspectives

8.1 General conclusion

We carried out small scale investigations of Mg single crystal using both an experimental and computational approach. The thesis report starts with a review of the theoretical and historical background of the crystallographic information concerning Mg crystals. An overview of the current understanding of the slip and twining behavior is given. Then, we detailed the experimental method used in this research and introduced the principle of the instrument used for the purpose: FIB, TEM, EBSD and nanoindenter.

The stress-strain relations resulting from microcompression experiments have been presented and discussed in terms of orientation dependent slip activity and twinning mechanisms. Five orientations were prepared, [0001], [2-1-12], [10-11], [11-20] and [10-10]. The deformation behavior is revealed through SEM, EBSD and TEM characterization of the deformation structures.

Experiments have shown that the deformation behavior is strongly governed by the initial crystallographic orientation. The stress-strain response and associated SEM images of the deformed column are summarized in Figure 4.31 and Figure 4.32. Strain burst was observed in all cases although the origin was different.

The size effect was also studied. The flow stress was plotted as a function of the pillar diameter and the exponent was calculated. The effect of twinning on the deformation being large compared to dislocation induced plasticity, this leads to severe size dependence. To explain the size effect due to dislocation plasticity, 'finite-volume self-organized criticality' was suggested. The main idea of this theory is that the ability for the system to arrange itself to dissipate strain energy depends on the number of dislocations within the volume. For the case of smaller volume, fewer dislocations will co-exist; therefore, it requires a higher applied stress to release the strain energy.

Dislocation dynamics simulations were performed to study the uniaxial

microcompression test focusing on the flow stress and the subsequent hardening behavior. A parametric study was performed by varying the initial dislocation density, the initial dislocation source length and the CRSS on the different slip systems. A set of parameters has been proposed although no definitive value could be attributed to the CRSS on the prismatic system. Simulations have been compared to the experimental observations in the case of [0001] and [2-1-12] orientations. This led to a schematic description of the deformation process.

8.2. Perspectives

8.2.1 Geometrical issue of microcompression test.

In addition to the experiments shown in this report, we have performed microcompression tests with squared shape column. The stress-strain response is shown in Figure 8.1 and the SEM pictures of the squared colum, in Figure 8.2. It is found that the squared column show a higher strain hardening and earlier strain bursts compared to the cylindrical column. However, there is no big difference in the SEM images of deformed column (see Figure 8.2). Such a difference might be related to the geometrical issue. For example, this could be attributed to stress concentration at the edge of the column. This geometrical issue is important in micro electric mechanical system (MEMS). Therefore, it would be interesting to further investigate this geometrical effect in a near future.
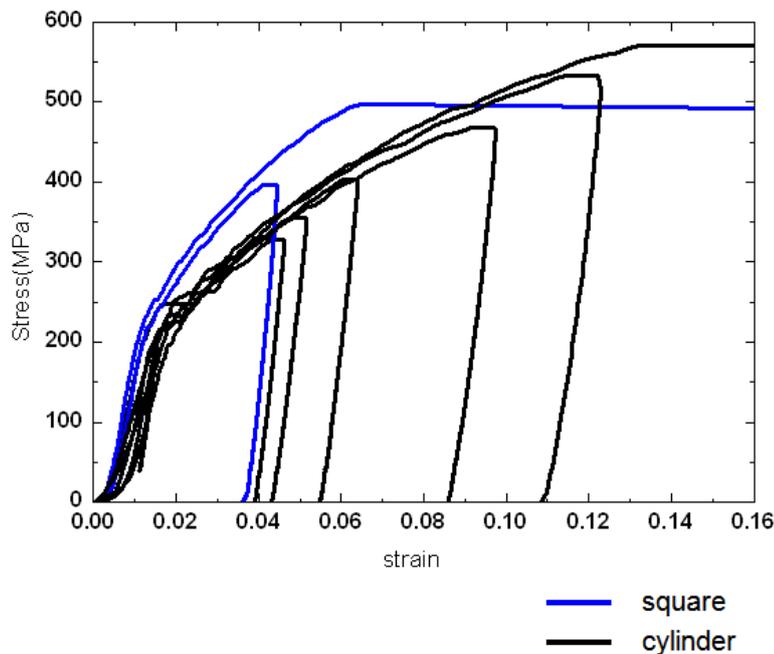
Figure 8.1: Stress-strain responses of square type column and cylindrical type column.
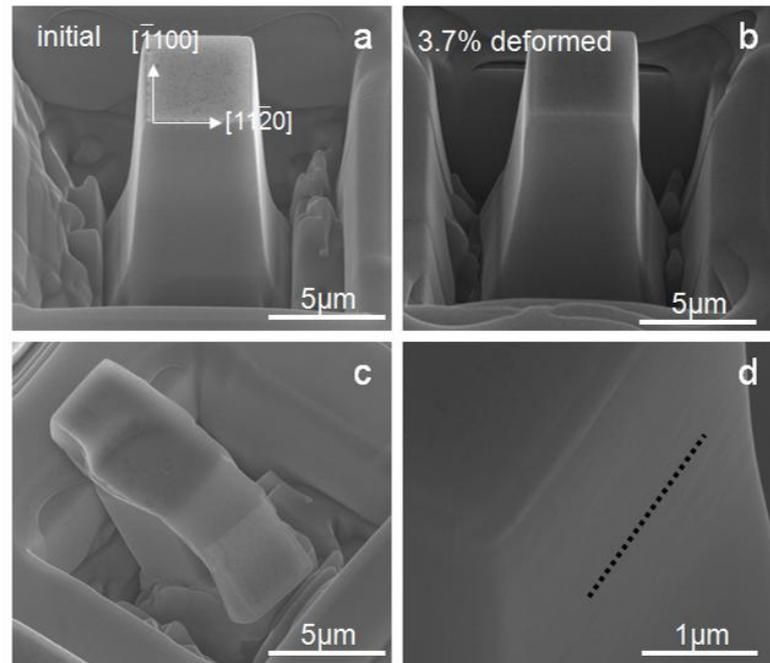
Figure 8.2: SEM images of a typical square type column. (a) initial (b) 3.7% deformed (c) strain burst occurred (d) slip traces. The slip trace in (d) indicated by black dot-line may likely correspond to the basal slip trace. However, more investigations are needed to confirm this hypothesis since it could also correspond geometrically to pyramidal slip system.

8.2.2 Improvements of dislocation dynamics simulations

Accounting for image forces

A dislocation near a surface is attracted toward the free surface due to the image stresses. In this study, the image stresses were ignored. However, as the size is smaller, the effect of the image stress will increase. Thus, numerical estimations of size effects could be improved by accounting for image forces for example through a coupling between the DD and the finite element method. This coupling is already available in TRIDIS so that it could be used in forthcoming studies.

Taking into account cross-slip

In this thesis the dislocation cross-slip was not activated because of numerical problems. On the other hand this mechanism could be very important to propagate dislocation activity from a slip system to another one. As an example, Chevy demonstrated in the case of ice crystals loaded in torsion that although the basal slip was the leading mechanism giving the apparent activation energy, the cross-slip events were the necessary mechanism needed to propagate the basal glide. Thus it is very important to account for cross-slip in the next generation of DD simulation of Mg microcompression. This may give better estimates of the CRSS on the prismatic systems.

8.2.3 Consideration of Ga damaged layer for dislocation dynamics

The FIB process always introduces surface defects such as a thin Ga damage layer. Figure 8.3 shows a schematic description of the Ga damage layer both for large and small pillars.
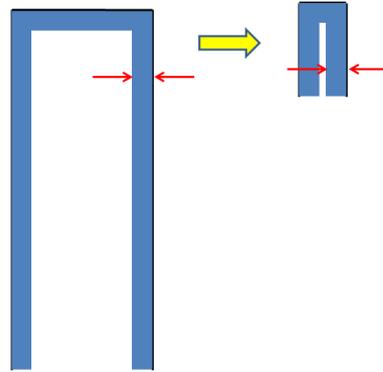
Figure 8.3: Schematic explanation of the Ga damage layer both for large and small pillars.

Because the thickness of damage layer does not depend on the sample size but the voltage, current and working time, the relative volume portion of damage layer increases as the sample is getting smaller. Therefore, one should take into account the presence of a damage layer in the DD simulations. With both the consideration of the image force and the Ga damaged layer, more precise result of size effect could be obtained by dislocation dynamics simulation. Here the difficulty consists in modeling the effect of the Ga damage layer on the dislocation mobility. Information could come from Molecular Dynamics studies.

References

[Agnew *et al*. 01] Agnew SR., YOO MH., TOME CN., Application of texture simulation to understanding mechanical behavior of Mg and solid solution alloys containing Li or Y, *Acta mater.,* 2001:49:4277.

[Agnew and Duygulu 05] Agnew SR., Duygulu Ö., Plastic anisotropy and the role of non-basal slip in magnesium alloy AZ31B, *Int. J. Plasticity,* 2005;21:1161.

[Arsenlis *et al*. 07] Arsenlis A., Cai W., Tang M., Rhee M., Oppelstrup T., Hommes G., Pierce TG., Bulatov VV., Enabling strain hardening simulations with dislocation dynamics, *Modelling Simul. Mater. Sci. Eng*., 2007:15:553.

[Bakarian and Mathewson 43] Bakarian PW., Mathewson CH., Strength of Metals and Alloys, *Trans. AIME,* 1943:152:226.

[Barnett MR 07] Barnett MR., Twinning and the ductility of magnesium alloys: Part II. "Contraction" twins, *Materials Science and Engineering A,* 2007:464:8.

[Bian and Shin 09] Bian MZ., Shin KS., Twin interactions in magnesium single crystal. *Magnesium Technology and their Applications2009*, Weimar. Germany, 2009.

[Bei *et al*. 07] Bei H., Shim S., George EP., Miller MK., Herbert EC., Pharra GM., Compressive strengths of molybdenum alloy micro-pillars prepared using a new technique, *Scripta Mater.,* 2007:57:397.

[Burke and Hibbard 52] Burke EC, Hibbard Jr. WR, Plastic Deformation of Magnesium Single Crystals, *Trans. Metall. Soc.,* 1952:194:295.

[Byer *et al*. 10] Byer CM., Li B., Cao B., Ramesh KT., Microcompression of single-crystal magnesium, *Scripta Mater.,* 2010:62:536.

[Canova and Kubin 91] Canova GR, Kubin LP., Dislocation microstructure and plastic flow : a three dimensional simulation. *Continuum models and discrete systems*, 1991.

[Chang *et al*. 07] Chang HJ., Han HN., Fivel MC., Multiscale modeling of Nanoindentation, *Key Engineering Materials*, 2007:345:925.

[Chaussidon *et al*. 08] Chaussidon J., Robertson C., Rodney D., Fivel M. Dislocation

dynamics simulations of plasticity in Fe laths at low temperature, *Acta Mater.*, 2008:56:5466.

[Chetty and Weinert 97] Chetty N., Weinert M., Stacking faults in Magnesium, *Phys. Rev. B*, 1997:56:10844.

[Chevy 09] Chevy J., Viscoplasticite et Heterogeneites de deformation du monocristal de glace: experiences et simulations, SIMaP, Thèse, INP Grenoble, 2008.

[Conrad and Robertson 57] Conrad H., Robertson WD., Effect of temperature on the flow stress and strain hardening coefficient of magnesium single crystals, *AIME,* 1957:209:503.

[Couret and Caillard 85] Couret A., Caillard D., An in situ study of prismatic glide in magnesium_The rate controlling mechanism, *Acta Mater.,* 1985:33:1447.

[Couret 85] Couret A., Caillard D., An in situ study of prismatic glide in magnesium II Microscopic activation parameters, *Acta Mater.,* 1985:33:1455.

[Devincre and Robert 96] Devincre B., Robert S., Three-dimensional simulation of dislocation-crack interactions in bcc metals at the mesoscopic scale, *Acta Mater.,* 1996:44:2981.

[Déprés 04] Déprés C., Modélisation physique des stades précurseurs de l'endommagement en fatigue dans l'acier inoxydable austénitique 316L, Laboratoire GPM2 - CEA Saclay DEN SRMA, Thèse, INP Grenoble, 2004.

[Dimiduk *et al*. 05] Dimiduk DM., Uchic MD., Parthasarathy TA., Size-affected single-slip behavior of pure nickel microcrystals, *Acta Mater.,* 2005:53:4065.

[El-awady *et al*. 09] El-Awady JA., Wen M., Ghoniem NM., The role of the weakest-link mechanism in controlling the plasticity of micropillars, *Journal of the Mechanics and Physics of Solids*, 2009:57:32.

[Fivel *et al*. 96] Fivel M., Gosling TJ., Canova G., Implementing image stresses in a 3D simulation, *Modeling Simul. Mater. Sci. Eng.,* 1996:4:581.

[Gharghouri *et al*. 99] Gharghouri M., Weatherly G., Embury J., Root J., Study of the mechanical properties of Mg-7.7at.% Al by in-situ neutron diffraction, *Phil. Mag. A*, 1999:79:1671.

[Ghoniem and Sun 99] Ghoniem NM., Sun L., Fast Sum Method for the Elastic Field of 3-D Dislocation Ensembles, *Phys. Rev.* B, 1999:60:128.

[Giessen & Needleman 95] Vander GE., Needleman A., Discrete dislocation plasticity: a simple planar model, *Modelling Simul. Mater. Sci. Eng.*, 1995:3:689.

[Graff *et al*. 07] Graff S., Brocks W., Steglich D., Yielding of magnesium: From single crystal to polycrystalline aggregates. *International Journal of Plasticity,* 2007:23:1957.

[Greer *et al*. 06] Greer JR., Nix WD., Nanoscale gold pillars strengthened through dislocation starvation, *Phys. Rev. B,* 2006;73:245410.

[Greer *et al*. 08] Greer JR., Weinberger CR., Cai W., Comparing the strength of f.c.c. and b.c.c. sub-micrometer pillars: Compression experiments and dislocation dynamics simulations, *Mat. Sci. Eng. A*, 2008:493:21.

[Groh *et al*. 09] Groh S., Marin EB., Horstemeyer MF., Bammann DJ., Dislocation motion in magnesium: a study by molecular statics and molecular dynamics, *Modelling Simul. Mater. Sci. Eng.* 2009:17:075009.

[Guruprasad and Benzerga 08] Guruprasad PJ., Benzerga AA., Size effects under homogeneous deformation of single crystals: A discrete dislocation analysis, *Journal of the Mechanics and Physics of Solids*, 2008:56:132.

[Handbook] Avedesian MM., Baker H., *Magnesium and Magnesium Alloys*, ASM Speciality, Handbook. ASM International, Metals, 1999.

[Hull and Bacon 01] Hull D., Bacon DJ., *Introduction to dislocation*, Pergamon Press, 2001.

[Kelly and Hosford 68] Kelley EW., Hosford WF Jr., Plane-strain compression of magnesium and magnesium alloy crystals, *Trans. Metall. Soc.,* 1968;242:5.

[Kelly and Groves 70] Kelly A., Groves GW., *Crystallography and Crystal Defects*, Addison-Wesley, p.163, 1970.

[Kim and Sa 06] Kim WJ., Sa YK., Micro-extrusion of ECAP processed magnesium alloy for production of high strength magnesium micro-gears. *Scripta Mater.*, 2006:54:1391.

[Kim *et al*. 09] Kim WJ., Jeong HG., Jeong HT., Achieving high strength and high ductility in magnesium alloys using severe plastic deformation combined with low-temperature aging, *Scripta Mater.*, 2009:61:1040.

[Kim GS *et al*. 10] KIM GS., Fivel M., Lee HJ., Shin CS., Han HN., Chang HJ., Oh KH., A discrete dislocation dynamics modeling for thermal fatigue of preferred oriented copper via

patterns, *Scripta Mater.,* 2010:63:791.

[Kim *et al.* 10] Kim GS., Yi SB., Huang Y., Lilleodden E., Twining and slip activity in magnesium <11-20> single crystal, in Mechanical Behavior at Small Scales - Experiments and Modeling, *Mater. Res. Soc. Symp. Proc.* Volume 1224, Warrendale, PA, 1224-FF05-03, 2010.

[Kiener *et al.* 09] Kiener D., Motz C., Dehm G.., Micro-compression testing: A critical discussion of experimental constraints, *Mat. Sci. Eng. A*, 2009 :505 :79.

[Ko *et al.* 07] Ko DS., Park YM., Kim SD., Kim YW., Effective removal of Ga residue from focused ion beam using a plasma cleaner, *Ultramicroscopy,* 2007:107:368.

[Kukta 98] Kukta RV., Observations on the kinetics of relaxation in epitaxial films grown on conventional and compliant substrates: a continuum simulation of dislocation glide near an interface, USA, Thèse, Brown University, 1998.

[Legros *et al.* 97A] Legros M., Minonishi Y., Caillard D., An in-situ transmission electron microscopy study of pyramidal slip in Ti_3Al : I. Geometry and Kinetics of glide, *Phil. Mag. A*, 1997:76:995.

[Legros *et al.* 97B] Legros M., Minonishi Y., Caillard D., An in-situ transmission electron microscopy study of pyramidal slip in Ti_3Al : II. Fine structure of dislocations and dislocation loop, *Phil. Mag. A*, 1997:76:1013.

[Lilleodden 10] Lilleodden ET., Microcompression study of Mg (0001) single crystal, *Scripta Mater.,* 2010:62:532.

[Liu *et al.* 96] Liu XY., Adams JB., Ercolessi F., Moriarty JA., EAM potential for magnesium from quantum mechanical forces, *Modelling. Simul. Mater. Sci. Eng,.* 1996:4:293.

[Manna *et al.* 07] Manna GE., Sumitomo T*.,* Cáceres CH., Griffiths JR., Reversible plastic strain during cyclic loading–unloading of Mg and Mg–Zn alloys, *Materials Science and Engineering A,* 2007:456:138.

[Monnet *et al.* 04] Monnet G., Devincre B., Kubin LP., Dislocation study of prismatic slip systems and their interactions in hexagonal close packed metals: application to zirconium. *Acta Mater.,* 2004:52:4317.

[Morozumi *et al.* 76] Morozumi S., Kikuchi M., Yoshinaga H., Electron microscope observation in and around {1-102} twins. *Trans JIM*, 1976:17:158.

[Motz et al. 09] Motz C., Weygand D., Senger J., Gumbsch P., Initial dislocation structures in 3-D discrete dislocation dynamics and their influence on microscale plasticity, *Acta Mater.*, 2009:57:1744.

[Ng and Ngan 09] Ng KS., Ngan KHW., Effects of trapping dislocations within small crystals on their deformation behavior. *Acta Mater.*, 2009:57:4902.

[Nogaret 07] Nogaret T, Modélisation multi-échelle des mécanismes de déformation des aciers austénitiques inoxydables irradiés, SIMaP, Thèse, INP Grenoble, 2007.

[Norfleet *et al*. 08] Norfleet DM., Dimiduk DM., Polasik SJ., Uchic MD., Mills MJ., Dislocation structures and their relationship to strength in deformed nickel microcrystals, *Acta Mater.*, 2008:56:2988.

[Obara *et al*. 73] Obara T., Yoshinaga H., Morozumi S., {11-22}<-1-123> slip system in magnesium, *Acta Mater.,* 1973:21:845.

[Oliver and Pharr 04] Oliver WC., Pharr GM., Measurement of hardness and elastic modulus by instrumented indentation. *J. Mater. Res.,* 2004:19:3.

[Oliver and Pharr 92] Oliver WC., Pharr GM., An improved technique for determining hardness and elastic modulus using load and displacement sensing indentation experiments. *J. Mater. Res.,* 1992:7:1564.

[Quimby *et al*. 62] Quimby RM., Mote JD., Dorn JE., Yield point phenomena in magnesium.lithium single crystals, *Trans. ASM,* 1962:55:149.

[Partridge 67] Partirdge PG., The crystallography and deformation modes of hexagonal close-packed metals, *Metall.Review,*1967:12:169.

[Robert CS 64] Robert CS, The deformation of magnesium, *Magnesium and Its Alloys,* Wiley, New York, 1964.

[Proust *et al.* 08] Proust G., Tome CN., Jain A., Agnew SR., Modeling the effect of twinning and detwinning during strain-path changes of magnesium alloy AZ31, *Int. J. Plasticity,* 2009:25:861.

[Reed-Hill and Robertson 57] Reed-Hill RE, Robertson WD., Deformation of magnesium single crystals by nonbasal slip, *Trans. Metall. Soc.,* 1957:220:496.

[Reed-Hill *et al*. 57] Reed-Hill RE, Robertson WD., Pyramidal slip in magnesium, *Acta Metall.,* 1957:5:717.

[Rosenbaum 64] Rosenbaum HS., Nonbasal slip in hcp metals and its relation to mechanical twinning, *Deformation Twinning*. Gordon and Breach, New York, 1964.

[Schwarz 99] Schwarz.KW., Simulation of dislocations on the mesoscopic scale. I. Methods and examples, *Journal of Applied Physics,* 1999:85:106.

[Shan *et al*. 07] Shan ZW., Mishra RK., Asif SA., Warren OL., Minor AM.,   Mechanical annealing and source-limited deformation in submicrometre-diameter Ni crystals, *Nature Materials,* 2007:7:115.

[Shenoy *et al*. 00] Shenoy VB., Kukta RV., Phillips R., Mesoscopic analysis of structure and strength of dislocation junctions in fcc metals, *Phy. Rev. Lett.*, 2000:84:1491.

[Shim *et al*. 09] Shim S., Bei H., Miller MK., Pharr GM., George EP., Effects of focused ion beam milling on the compressive behavior of directionally solidified micropillars and the nanoindentation response of an electropolished surface. *Acta Mater.,* 2009:57:503.

[Shin *et al*. 06] Shin CS., Fivel MC., Verdier M., Oh KH., Numerical methods to improve the computing efficiency of discrete dislocation dynamics simulations, *J. of Comp. Phys.*, 2006:215:417.

[Shin *et al*. 07] Shin CS, Robertson CF., Fivel MC., Fatigue in precipitation hardened materials, a three dimension discrete dislocation dynamics modelling of the early cycles, *Philosophical Magazine*, 2007:87:3657.

[Shin 04] Shin CS, 3D discrete discloation dynamics applied to dislocation-precipitatie interactions, GPM2, Thèse, INP Grenoble, 2004.

[Smith 07] Smith AE., First principles calculations of stacking fault energies for magnesium and titanium, *Matrials Forum,* 2007:31:71.

[Song and Gray 95] Song SG., Gray III GT., Structural interpretation of the nucleation and growth of deformation twins in Zr and Ti—II. Tem study of twin morphology and defect reactions during twinning, *Acta Mater.,* 1995;43:2339.

[Staroselsky and Anand 03] Staroselsky A., Anand L., A constitutive model for hcp materials deforming by slip and twinning: application to magnesium alloy AZ31B, *Int. J. Plast*., 2003:19:1843.

[Stohr and Poirier 72] Stohr JF., Poirier JP., Etude en Microscopie Electronique de Glissement Pyramidal {1122}<1123> dans le Magnesium. *Phil. Mag.,* 1972:25:1313.

[Schwarz 99] Schwarz KW., Simulation of dislocations on the mesoscpoic scale. I. methods and examples, *J. Appl. Phys.*, 1999:85:108.

[Tang *et al*. 98] Tang M., Kubin LP., Canova GR., Dislocation mobility and the mechanical response of bcc single crystals : a mesoscopic approach, *Acta Mater.*, 1998:46:9.

[Tang *et al*. 07] Tang H., Schwarz KW., Espinosa HD., Dislocation escape-related size effects in single-crystal micropillars under uniaxial compression, *Acta Mater.* 2007:55:1607.

[Taylor 38] Taylor GI., Plastic strain in metals. *J. Inst. Met.,* 1938:62:307.

[Thomas and Goringe 79] Thomas G, Goringe MJ, *Transmission electron microscopy of materials*, John Wiley & Sons, 1979.

[Uchic *et al*. 04] Uchic MD., Dimiduk DM., Florando JN., Nix WD., Sample dimensions influence strength and crystal plasticity, *Science*, 2004:305:986.

[Uchic and Dimiduk 05] Uchic MD., Dimiduk DM., A methodology to investigate size scale effects in crystalline plasticity using uniaxial compression testing, *Mat. Sci. Eng. A* 2005:400:268.

[Uesugi *et al*. 03] Uesugi T., Kohyama M., Kohzu M., Higashi K., Generalized stacking fault energy and dislocation, properties for various slip systems in magnesium: A first principles study, *Mat. Sci. Forum*, 2003:225:419.

[Volkert and Lilleodden 06] Volkert CV., Lilleodden ET., Size effect in the deformation of sub-micron Au columns, *Phil. Mag.,* 2006;86:5567.

[Verdier *et al*. 98] Verdier M., Fivel M., Groma I., Mesoscopic scale simulation of dislocation dynamic in fcc metals: Principle and applications, *Modelling and Simulation in Materials Science and Engineering*, 1998:6:755.

[Wonsiewicz and Backofen 67] Wonsiewicz BC., Backofen WA., Plasticity of magnesium crystals, *Trans. TMS-AIME,* 1967:239:1422.

[Ward Flynn P *et al*. 61] Ward Flynn P., Mote J., Dorn JE., On the thermally activated mechanism of prismatic slip in magnesium single crystals. *Trans Metall Soc.,* 1961;221:1148.

[Weygand *et al*. 01] Weygand D., Friedman LH., Giessen EV., Discrete dislocation modeling in three-dimensional confined volumes, *Materials Science and Engineering A*, 2001:309:420.

[Weygand *et al*. 08] Weygand D., Poignant M., Gumbsch P., Kraft O., Three-dimensional dislocation dynamics simulation of the influence of sample size on the stress–strain behavior of fcc single-crystalline pillars. *Materials Science and Engineering A*, 2008:483:188.

[Williams and Carter 04] Willams DB., Carter CB., *Transmission Electron Microscopy: A Textbook for Materials Science*, Springer, 2004.

[Wu *et al*. 08] Wu L., Jain A., Brown DW., Stoica GM., Agnew SR., Clausen B., Fielden DE., Liaw PK., Twinning–detwinning behavior during the strain-controlled low-cycle fatigue testing of a wrought magnesium alloy, ZK60A. *Acta Materialia,* 2008:56:688.

[Yi *et al*.10] Yi SB., Bohlen J., Heinemann F., Letzig D., Mechanical anisotrophy and deep drawing behavior of AZ31 and ZE10 magnesium alloy sheets. *Acta Mater.,* 2010;58:592.

[Yi 05] Yi Sangbong. Investigation on the deformation behavior and the texture evolution in magnesium wrought alloy AZ31, Ph.D. Thesis, Techniscen Universität Clausthal, 2005.

[Yoo 81] YOO MH., Slip, twinning, and fracture in hexagonal close packed metals, *Metall. Trans. A,* 1981:12:409.

[Yoshinaga and Horiuchi 63] Yoshinaga H., Horiuchi R., Deformation mechanisms in magnesium single crystals compressed in the direction parallel to the hexagonal axis, *Trans. JIM,* 1963:4:1.

[Yu *et al*. 10] Yu Q., Shan ZW., Li J., Huang X., Xiao L., Sun X., Ma E., Strong crystal size effect on deformation twinning. *Nature*, 2010:463:335.

[Zbib *et al*. 99] Zbib HM., Rhee M., Hirth JH., On plastic deformation and the dynamics of 3d dislocations, *Int. J. Mech. Sci.,* 1999:40:113